Numerical study of divertor detachment in the MAST-U tokamak

Investigating the role of atom-plasma and molecule-plasma interactions during divertor detachment

Yulin Zhou

PhD
University of York
Physics

September 2022

Abstract

Divertor detachment is a promising method to reduce heat loading and erosion in tokamak devices or even in future magnetic fusion reactors. In this thesis, two detachment regimes (increasing upstream density and seeding impurity) leading to the decrease of the divertor ion flux is numerically studied through modelling the super-X divertor in MAST-U like conditions. This thesis builds on previous work using the original SD1D modules of BOUT++, which is established to simulate parallel transport process from upstream to the target.

We implement an upgrade in SD1D module by adding molecule-plasma interactions and impurity seeding in order to making simulations more self-consistent. To understand the role of molecules in density ramp detachment process, comparisons are made between the cases with different recycling conditions. It is found that if the recycling in divertor is more likely to produce neutral molecule, the roll-over of ion flux at the target occurs at a higher upstream density and a lower target temperature. We also find that molecule–plasma interactions are as crucial as atom–plasma interactions during divertor detachment, both of which account for the main plasma momentum loss. Molecule–plasma interactions can even cause a strong rise of Halpha signal in the detachment process, which agrees with the measurement on other devices (e.g TCV tokamak).

The divertor detachment induced by seeding impurity (e.g. neon) is simulated in order to understand the difference between the two detachment regimes. It is found that increasing the puffing rate of neon impurity cannot quickly reduce the target temperature, thus the density of molecule species is small during detachment due to the high molecule dissociation rate, while atom-plasma interactions become dominant and account for the most of plasma momentum loss. Different from the density ramp induced detachment, we cannot find the strong rise of Halpha signal in this case.

Contents

List of Tables

List of Figures

Acknowledgements

Time always run fast. It has been the end of my PhD research. In the past four years, I received help and guidance from a lot of people. The work presented in the thesis would not have been possible without their invaluable contribution.

Professionally I would like to express my deepest appreciation to my supervisors Ben Dudson and Fulvio Militello, who have been supportive of my research and daily life since the start of my PhD project. Ben and Fulvio are very kind person, whose knowledge into the subject matter steers me through this research. They are admirable scientist, full of energy and creativity. Both of them play a decisive role in my research. As I am an international student, their suggestions and experience are very helpful for me to adapt to the working and living environment. And special thanks to Kevin Verhaegh and David Moulton, whose support allows my research to go extra miles.

And my biggest thanks to my families for all the support you have given me, especially my wife Jing He who always has profound belief in my work and gives me encouragement through the research. Appreciate the help of my landlord Willie and Sarah, who offer us accommodation and their living experience.

Appreciate the support of the China Scholar ship Council and the National Natural Science Foundation of China (11805055), who offers fund for my PhD research.

Author's Declaration

I declare that this thesis is a presentation of original work and I am the sole author. This work has not previously been presented for an award at this, or any other, University. All sources are acknowledged as References.
Parts of this thesis have been adapted from the following papers:

- Chapter3 and Chapter4 contain material from the publication: Yulin Zhou, Benjamin Dudson, Fulvio Militello, Kevin Verhaegh and Omkar Myatra, "Investigation of the role of hydrogen molecules in 1D simulation of divertor detachment",2022 Plasma Phys. Control. Fusion 64 065006

Chapter 1

Introduction

1.1 Energy crisis and possible solutions

The industrial revolution in the past 200 years have significantly changed people's live. The massive technical progress provides an exponential economic growth and an improving living quality. But the industrial revolution and the fast technological development require massive energy use. TeraWatts of energy is needed to just maintain our living standards. As the most widely available energy source, fossil fuels such as natural gases, coal and oil are the most important energy source for the current day world. They are formed from the conserved remains of animals and plants over a geological time span (millions of years). But due to the requirement of fast development, fossil fuel resources are being consumed at an alarming rate, which leads to the serious problem of energy scarcity. It is found that the oil, gas and coal reserves will be used up within about 100 years [1][2].

What is more, the continuous use of fossil fuel resources have shown serious side effects in our living world, climate change and environmental pollution. Greenhouse gases exhausted in the air like carbon dioxide and nitrogen oxides, are largely produced by the use of fossil fuel resources. The fast exhaust of these gases have caused global warming, which leads to extreme climate change. Floods, droughts, extreme heatwave and sea level rise happen more often in densely populated regions. Some other products of burning fossil fuel like particulate matters, sulphur dioxide and carbon monoxide are deteriorating the air quality and thus have already led to serious public health issues [3], especially in the developing countries. In order to prevent people from potential global catastrophes and pollutants in the air, it requires our immediate action to control the exhaust of harmful gases. So it is very urgent to accelerate the transition of our social development from fossil-fuel based to more renewable or nuclear energy based.

Currently, there is only about 18% of all energy sources produced through renewable (about 13%) and nuclear energy sources (about 5%) (figure 1.1)[1],both of which are mostly produced in developed countries. But a large part of total population is still in developing countries, a much bigger energy consumption is needed to improving quality of life and social development (1.2) [1]. Therefore developing new energy supply technologies and reducing the usage of fossil fuel have become a global challenge. The renewable energy sources like solar, hydropower, wind and biomass has been fast developed in the past 46 years. The total renewable energy produced in 2019 is about triple of it in 1973[1]. But it has some disadvantages like a relatively low power production and high cost of utilize renewable energy, it is more expensive to use renewable energy. Energy generation is significantly based on the natural conditions, such as weather and tide, thus a more complex energy storage technique is needed to deal with the fluctuation of power generation. Furthermore, the power plant must be built in a certain area in order to use renewable energy like coastal areas for tidal power and sunny areas for solar power. It cannot be used anywhere. So the renewable energy cannot replace fossil fuel currently, which is still the most available and cheapest energy source.

Clean energy is not only obtained from natural phenomenon like wind and tide, it can also be generated by capturing heat from atoms that split apart (or nuclear fission) [4]. In figure 1.1, nuclear fission energy supply only provided 0.9% of the global share of total energy supply in 1973, but it fast grew to 5% in 2019. Nuclear fission-based reactor could generate sustainable and clean energy with a relatively high energy production. The fast development in the past decades has made nuclear fission energy supply technique mature, which largely reduces the safety risk and the cost of energy production [5]. In some developed countries, nuclear fission energy has already become one of the most important energy sources, such as France (69.9%), Sweden (39.3%) and Korea (25%) [1]. In the future, the number of nuclear fission

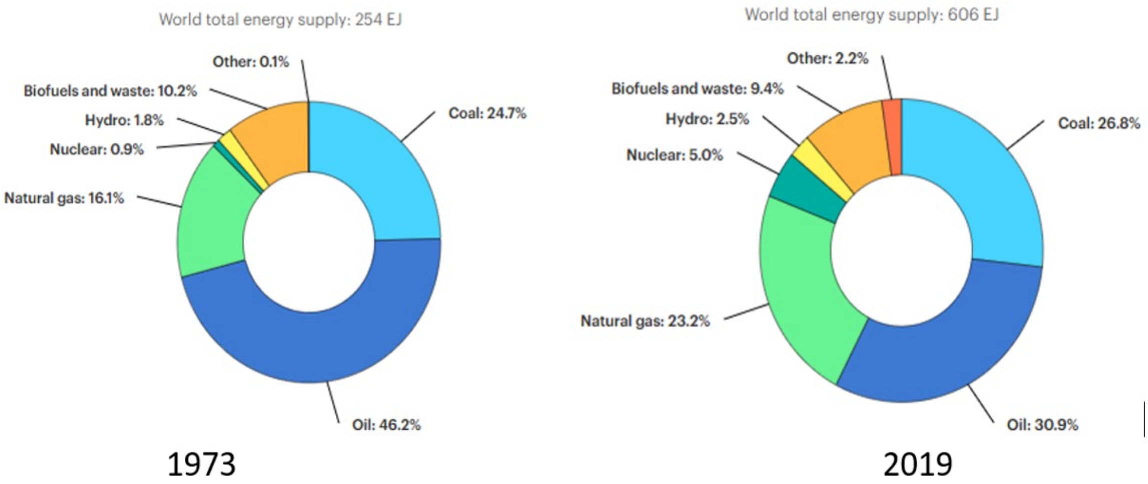

Figure 1.1: Global share of total energy supply by source[1]

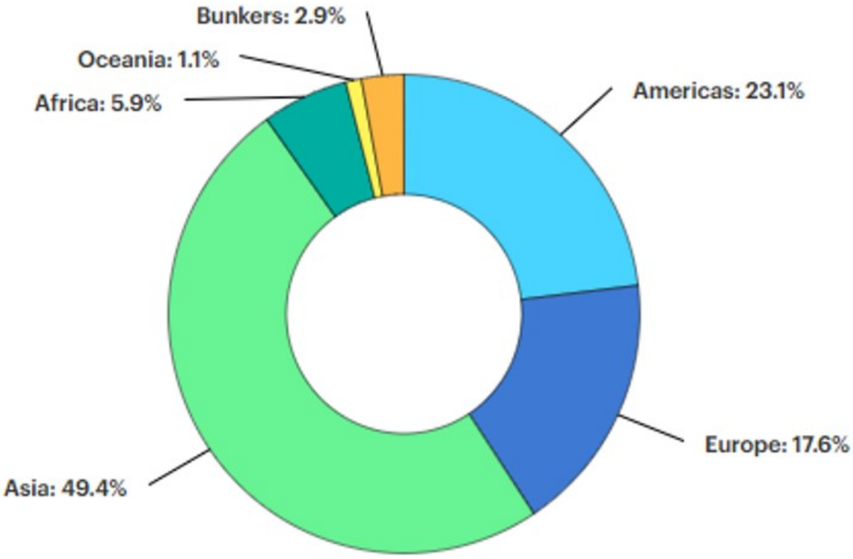

Figure 1.2: Regional share of total energy supply[1]

plants is expected to largely increase in order to fulfil the requirement of low carbon economy in Paris energy agreement [6].The development of nuclear fission energy in such countries does help to reduce of usage of fossil fuel. While it has many advantages, it also plenty of negative effects[7]:

(1) Environmental impact: Mining the uranium used to produce nuclear energy would release arsenic and radon, which have a negative impact on the surrounding area; Nuclear power plants cause thermal water pollution (Heated water is released to an aquatic ecosystem).

(2) Water intensive: The water consumption in nuclear power plants is enormous, which is more than what is used for coal processing.

(3) Risk of nuclear accidents: Although nuclear power plants have very strict safety measure in place, the risk is always existing. Once accidents happen, it will become a national or even global disaster.

(4) Radioactive waste: There is no harmful greenhouse gase emitted in the air from nuclear power plants. But it produces hazardous radioactive waste, which continues to accumulate in nuclear power plants. It will become an issue once power plants run out storage space. Any leak of the waste will lead to massive radioactive pollution.

(5) Non-renewable: The fuel used in nuclear reactors like uranium is a limited resource. It is estimated that the world's uranium resources could provide sufficient energy for about 200 years.

With the disadvantages, nuclear fission energy is still not an idea solution for the energy crisis.

Theoretically the process of atomic nuclei combining to form a heavier nucleus (or nuclear fusion) can also provide an energy source[8].Different from nuclear fission, it is a clean energy and there is abundant fuels for nuclear fusion (i.e. hydrogen, deuterium and tritium) that can be easily obtained from sea water. It is very safe. Only a small amount of radioactive waste produced in nuclear fusion, and its lifespan is much shorter than that of a nuclear fission[9][10]. Energy released during the fusion of deuterium and tritium could be a thousand times greater than fission of uranium and billions times the burning of coal. Therefore nuclear fusion is regarded by many as the ultimate energy supply for humankind[11].However, the technical challenge of how to get energy from nuclear fusion is still a problem. In order to realize controllable nuclear fusion and achieve sustainable energy, scientists and engineers from 35 countries including Europe, China, Japan, the US, Russia, India are working together to build the largest fusion experiment ever conducted in France, called ITER(International Thermonuclear Experimental Reactor). The goal of ITER is to operate at 500 MW with less than 50 MW of input power, a tenfold energy gain, but no electricity will be generated at ITER [12].A demonstration Power Plant, known as Demo, is expected to demonstrate large-scale production of electrical power on a continual basis. The conceptual design of Demo is expected to be completed by 2024, with the first construction phase is to last from 2024 to 2033. The goal of Demo is to generate twenty five times more energy. The first phase of operation commencing from 2033 [13][14]

1.2 Nuclear fusion and different plasma confinement methods

When two or more atomic nuclei come close enough for the strong nuclear force to exceed the electrostatic force and pull them together, they could combine to form a heavier nucleus. There will be a difference in mass between the products and reacted particles. For instance, two protons and two neutrons is heavier than an alpha particle (consists of two protons and two neutrons). According to Einstein's mass–energy equivalence, the difference in mass is manifested the release of energy, which leads to a larger binding energy between the atomic nuclei after the reaction. A nuclear fusion process that produces atomic nuclei lighter than iron-56 is exothermic and release energy, while for nuclei heavier than iron-56 nuclear fusion process is endothermic and requires an external source of energy. Thus nuclear fusion uses lighter elements like hydrogen, deuterium, tritium and helium [15].The elements heavier than iron-56 are more likely used for nuclear fission, such as uranium, thorium and plutonium.

To achieve nuclear fusion, a substantial energy barrier of the Coulomb force must be overcome. It is a force caused by nuclei containing positively charged protons, which repel each other via the electromagnetic force. If the nuclei get close enough, the nuclear force can be dominant over the Coulomb force and pull them together. Most of the fusion occurs in the high energy tail of the Maxwellian distribution.In figure 1.3, it lists the main fusion reactions and their fusion reaction cross-sections as a function of the incident particle energy[15]. It is found that the fuel mixed by deuterium and tritium (D-T) has the lowest kinetic energy to fuse. It provides 14.1MeV of energy. Although the D-T fusion reaction is the best option, it still requires a very high temperature (10keV $-$ 100keV) to achieve nuclear fusion. But such a high temperature is still insufficient for obtaining net energy from fusion reactions, since collisions between charged particles and radiation emission also cause significant energy loss. Thus it is a big challenge to confine the reacting fusion particles and their energy.

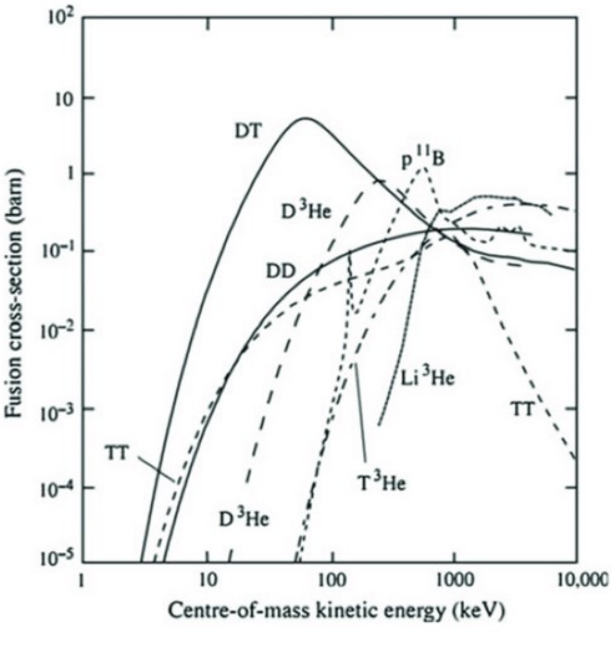

Figure 1.3: Fusion reaction cross-sections as a function of the incident particle energy, for the nuclear fusion reactions[15]

Lawson criterion gives the conditions of net energy generation [16]. This criterion defines the energy confinement time $\tau_E = W/P_{loss}$, representing the rate at which a system loses energy. W is the energy density of the system and P_{loss} is the power lost per unit volume. To operate a fusion machine in a steady state, the fusion plasma temperature must be at a constant temperature (assume all species have the same temperature and there are no impurities). Thermal energy must therefore be added at the same rate of the plasma energy loss in order to maintain the fusion conditions. This energy can be supplied by the fusion reactions themselves or by external heating sources. For the case of a $50 : 50$ mix of D-T (the same principle can be applied to other fusion fuels), the energy density of both electrons and ions together is $W = 3nk_BT$.The volume rate f(reactions per volume per time) of fusion reactions is $f = n_D n_T < \sigma\upsilon >= 1/4n^2 < \sigma\upsilon >$, where σ is the fusion cross-section (in figure1.3),υ is the relative velocity,and $<>$ represents an average over the Maxwellian velocity distribution at the temperature. The volume rate of heating by fusion is $f_{E_{ch}}$. E_{ch} is the energy of the charged fusion products. The Lawson criterion requires that fusion heating exceeds the losses. So based on the discussion above, $f_{E_{ch}} > P_{loss}$. $1/4n^2 < \sigma\upsilon > E_{ch} > \frac{3nT}{\tau_E}$. The equation can be written as:

$$n\tau_E \geqslant L \equiv \frac{12T}{E_{ch} < \sigma\upsilon >} \tag{1.1}$$

The quantity $\frac{T}{<\sigma\upsilon>}$in equation 1.1 is function of temperature with an absolute minimum. Replacing $\frac{T}{<\sigma\upsilon>}$ with its minimum value gives an absolute lower limit for the product $n\tau_E$. This is the Lawson criterion.

There are various nuclear fusion schemes which try to fulfil the fusion requirement. Inertial confinement fusion (ICF) and magnetic confinement fusion (MCF) are two main approaches for fusion research. ICF, which uses power laser pulses to compress a small pellet of fusion fuel, aims at increasing the pressure nT as much as possible. But only using the target's inertia for confinement results in a relatively small τ_E. It uses power laser pulses to compress a small pellet of fusion fuel. MCF utilise a magnetic field in order to confine the ionised plasma fuel. This approach provides a much larger energy confinement times, so a lower plasma pressure nT is needed for achieving fusion reaction. In this thesis, we only discuss magnetic confinement fusion.

The temperature required for fusion (tens of millions of degrees) is too high for any known materials to directly contact the fusion plasma. MCF provides a promising

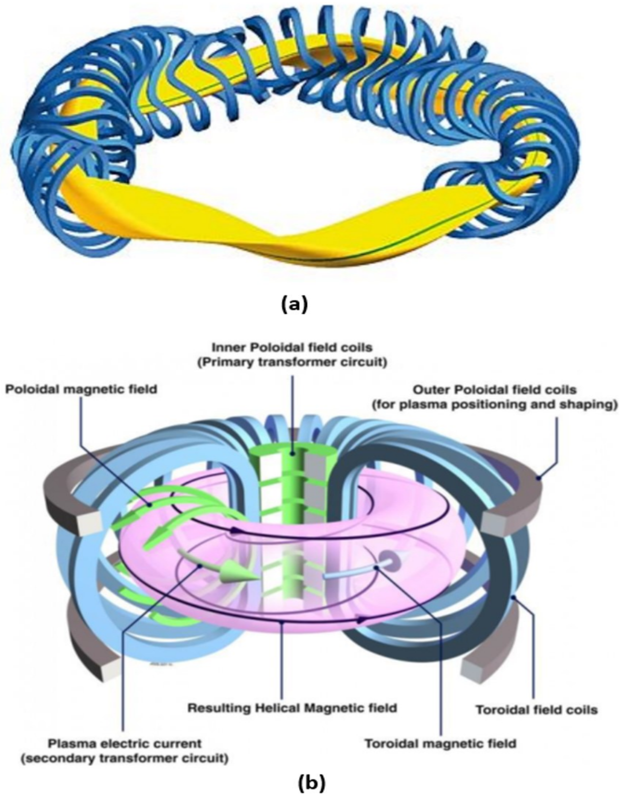

Figure 1.4: The configuration of a stellarator [17] and a tokamak device[18]

approach to achieve a good plasma confinement, which uses magnetic fields to localise the charged plasma. The magnetic mirror was the major research area in the early years of fusion energy research. The devices with the mirror configuration consisted of a linear tube with magnets around the outside. The magnets were arranged in two sets, one set of small magnets spaced evenly along the length of the tube, and another pair of much larger magnets at either end. The confinement mainly depends on adiabatic invariance of the magnetic moment add total energy. But particles with high kinetic energy still escape through the ends of the magnetic mirror. A toroidal shape configuration, which connects both ends of the magnetic mirror, could well solve this problem. Stellarators is one of the ways to achieve the toroidal shape configuration. It uses unconventional coil shapes to generate a helical magnetic field structure as shown in figure 1.4(a) [17]. Tokamak is another one, which uses more conventional and simpler coils to generate a toroidal magnetic field configuration. The plasma current along the field line could generate a poloidal magnetic field. The poloidal and toroidal fields combine to form a helical magnetic field configuration, as shown in figure 1.4(b) [18]. Although stellarators do not need a current to be driven, the coil system needs to generate the magnetic field is much more complicated compared to that of the tokamakk. Tokamaks on the other side are easier in design and maintenance, and have higher performance than stellarators.

1.3 The heat exhaust problem and tokamak divertor

Figure 1.5 a shows the cross section of a large-scale tokamak. The plasma current with high kinetic energy is confined and flows circularly in the magnetic cage. However, the confinement is not perfect. The massive power required by nuclear fusion leads to significant collision rates within the plasma and causes large pressure gradients from the core plasma to the edge area. A significant amount of heat will leak out from the core into the edge. Additionally, the turbulence caused by pressure gradients can accelerate the cross-field transport, which is the transfer of heat and particles across magnetic flux surfaces. Therefore the wall of containing the vessel, which is close to the edge area, will inevitably contact the leaked plasma. In this process, energetic plasma particles strike the solid surface, dislodging atoms from the lattice [19]. These atoms will sputter into the core of the plasma and result in plasma contamination, which lowers the core plasma performance.

The divertor, a promising solution of heat exhaust problem, was developed in order to extract heat and ash produced by the fusion reaction, minimize plasma contamination, and protect the surrounding walls from thermal and neutronic loads. A poloidal divertor configuration (figure 1.5b) can be produced by using an external conductor carrying a current I_D in the same direction as the plasma current I_p[19]. The thin region between the separatrix and the vessel wall is formed, called the scrape-off layer (SOL) that largely reduces the direct contact between hot plasma and wall surface. There is a null in the poloidal field, called X-point, at the point between the two current centres. The magnetic flux surface passing through the X-point is the magnetic separatrix. A solid plane cutting through the flux surfaces surrounding the I_D is introduce to form a plasma sink. Plasma particles escaping through separatrix will flow along a field line in the SOL and eventually strike on the solid surface, which are call the divertor target. Different types of divertor have been designed,

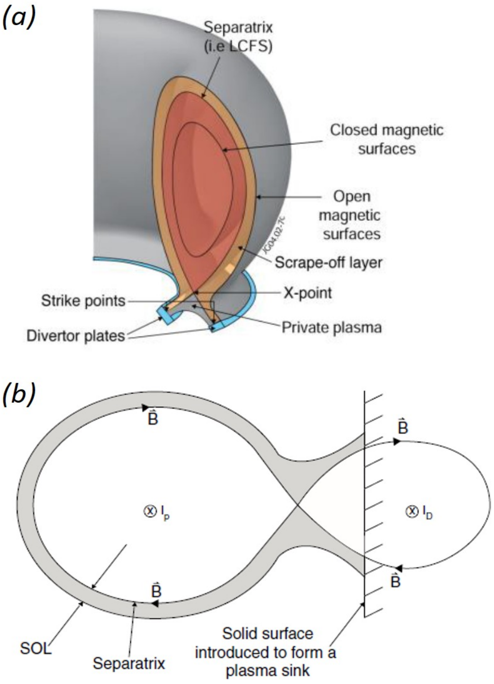

Figure 1.5: (a) The field cross section in the divertor configuration; (b) a poloidal divertor configuration produced using an external conductor carrying a current I_D in the same direction as the plasma current I_p [19]

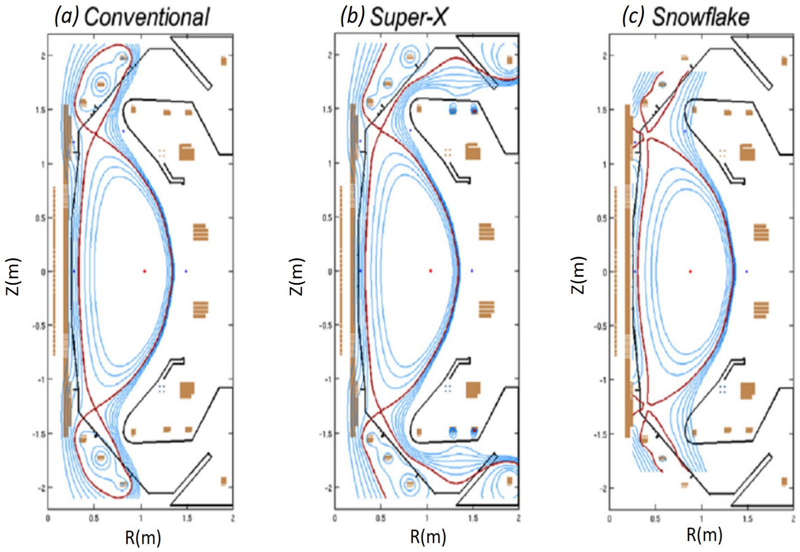

Figure 1.6: Free boundary vacuum calculations of some of the achievable plasma configurations in MAST Upgrade showing the conventional double-null diverted configuration, a Super-X long divertor leg configuration and a snowflake configuration, demonstrating the flexibility of MAST Upgrade for studying alternative exhaust configurations[20]

including toloidal divertor [21] and poloidal divertor [22][19]. Currently the poloidal divertor has become the first option for tokamak research. The design of magnetic field configuration in divertor chamber can be flexible, as shown in figure 1.6. There are tokamaks like MAST-U with the so called 'super-X' divertor, which extends the divertor leg (or magnetic field configuration in the divertor) in order to spread the arriving heat over a much larger area, increasing the distance the evacuating particles have to travel to be exhausted. Tests at MAST-U, which began operating in October 2020, have shown at least a tenfold reduction in the heat on materials with the Super-X system [23]. It would also allow components in future commercial tokamaks to last for much longer; greatly increasing the power plant's availability, and reducing the cost of fusion electricity. The Snow-flake divertor is another creative design. The general idea behind the snow-flake configuration is that, by a proper selection of divertor (poloidal field) coils, one can make the null point of the second, not of the first order as in the conventional divertor. The separatrix in the vicinity of the X-point then acquires a characteristic hexapole structure, reminiscent of a snowflake. The fact that the field has a second-order null, leads to a significant increase of the flux expansion [24]. Since the heat flux normally flows along the magnetic field lines, tilting the target plates for changing the angle between field lines and the material surface can be another good way to reduce heat load on target [25].In ITER, the heat flux on the target plates can obtain a factor of about 30 lower than the traditional design.

The 'closed divertor' is currently used in tokamak devices like TCV, in order to physically separate the divertor region from the plasma core region. This design improves confinement of neutrals produced by recycling in the divertor volume, therefore a larger neutral density is obtained in the close divertor than in the traditional one, and helps to reduce the heat load in the divertor [26]. The impurities either from impurity seeding or from plasma-surface interaction are also confined or accumulated in the closed divertor, which lead to a higher radiation power than the conventional divertor [27] . However this design will make diagnostic measurements in divertor difficult.

1.4 The possible solutions of heat exhaust problem

It is a big challenge to tame divertor power exhaust to an acceptable level. As discussed in section 1.3, the design of super-X and snow-flake divertors could help to decrease heat load on plasma-facing materials. There are several other approaches could help to address this problem:

(1) Tilting the target plates: make a larger angle between the field lines and the material surface in order to increase the effective wetted area on material surface [28]

(2) A stronger material needs to be used for the plasma-facing material, like Tungsten and Molybdenum.

(3) Divertor detachment: Seeding impurities or increasing the upstream density are the two most widely used approaches to reach the detached divertor regime [29][19].

In terms of divertor detachment induced by impurity seeding, the divertor is cooled down mainly due to the radiation from impurities, which are generated by plasma-material interactions (e.g. sputtering from plasma facing materials, leading to the release of C, W) [30] or extrinsic impurity seeding (e.g. nitrogen, neon) [31]; In the second regime, neutral gas (like hydrogen, deuterium or tritium) may be injected through gas puffing, raising the density in the core and leading to an increasing upstream density, which is able to cause a lower target plasma temperature according to the Two Point Model (TPM) [19]. The increasing upstream density also intensifies recycling at the target, which results in a larger neutral density. It accelerates the interaction between neutrals and the plasma flux moving towards the target and thus further cools the divertor. Divertor detachment is the topic of this work, which will be specifically discussed in Chapter 2.

1.5 Overview of the thesis

This chapter introduced different energy sources which could be the solution of energy crisis, the advantage of fusion energy compared to other energy sources, and the approaches to achieve divertor detachment in the tokamak fusion research.

In Chapter 2 we complete a literature review on atomic and molecular physics in tokamak divertor, a simplified model (Two Point Model), the approaches to achieve divertor detachment, and the experimental diagnosing and numerical modelling of divertor detachment.

In Chapter 3, we introduce the BOUT++ framework and the newly developed module SD1D. Then we implemented two upgrades in the original SD1D module: (1) add the molecular model in SD1D and (2) add the impurity (neon) model in SD1D. The upgraded physical model of SD1D is used in the rest of the thesis.

Next in Chapter 4 we use the upgraded SD1D to investigate the role of atomic and molecular processes during divertor detachment with upstream density scan. The effect of different recycling conditions on the target ion flux and target temperature is analysed in this part.

To understand the difference of detachment induced by upstream density ramp and by impurity seeding, in Chapter 5 we use the upgraded SD1D (with neon impurity) to compare the atomic and molecular processes during two different scans (upstream density scan and neon seeding rate scan), and we analyse the particle, momentum and power balance during the two scans. In this chapter, we also investigate the effect of force balance on the neon ions.

Chapter 2

Literature Review

This chapter provides an overview of divertor physics. Section 2.1 reviews the basic physics of divertor for the understanding of particle and heat transport in divertor. Section 2.2 reviews atomic and molecular physics in the divertor volume, in particular the data analysis of collisional and radiative reactions, which is crucial to the understanding of divertor detachment. An important analytical model for divertor research, the Two Point Model (TPM), is reviewed in section 2.3. In the last section, experimental measurements and numerical modelling of divertor detachment are highlighted for understanding the motivation of this work.

2.1 The basic physics of tokamak divertor

Plasma particles and energy, escaping from the confined plasma, will be transported along the magnetic field lines in the scrape-off layer (SOL) until they finally strike the divertor targets (figure 1.5(a)). As discussed in section 1.3, the tokamak divertor is primarily used to extract the heat and particles flowing out from the core plasma area. The heat and particle flux flowing into the divertor plays a crucial role in determining the temperature in the SOL region and the divertor. So, understanding the transport of heat and particle flux in the divertor becomes a crucial area of study for divertor power exhaust.

2.1.1 Particle flux flowing from plasma to the solid surface

Since the mass of an electron is much smaller than the mass of an ion, the thermal velocity of the electrons can be much higher compared to the ions. Therefore, the solid surface (e.g. the target) will receive a higher electron flux and becomes negatively charged. A narrow region close to the surface is therefore produced, called the sheath, where the assumption of quasineutrality is no longer available and $n_i > n_e$. As a result, the Coulomb force produced by this negatively charged surface will attract the ions and push away the electrons. The width of the sheath can be defined as an expression of T_e and n_e [19][32]:

$$\lambda_D = \sqrt{\frac{\epsilon_0 k_B T_e}{e^2 n_e}} \tag{2.1}$$

Typically, the width of the sheath is very small, e.g. just several micrometers for the MAST tokamak [33]. The electrostatic potential V distribution given by the Poisson equation is

$$\frac{d^2V}{dx^2} = -\frac{e}{\epsilon_0}\left(n_i - n_e\right) \tag{2.2}$$

The electrostatic potential drop along the SOL to the target accelerates the speed of ions, which can be written as:

$$v_i = -\sqrt{2eV/m_i} \tag{2.3}$$

Here it is assumed that the ion kinetic energy is produced by the potential difference. According to the continuity equation (the current $j_i = n_i v_i = const$, we can get $v_i/v_{i,s}$ and obtain:

$$n_i = n_{i,s}\sqrt{\frac{V_s}{V}} \tag{2.4}$$

where s represents the sheath. $v_{i,s}$, $n_{i,s}$, $V_{i,s}$ are ion velocity, ion density and the potential at the sheath entrance (defined at a distance of sheath width from the solid surface). The density of electron is defined by a Boltzmann distribution:

$$n_e = n_{e,s} exp\left[\frac{e\left(V - V_s\right)}{k_B T_e}\right] \tag{2.5}$$

If quasineutrality is still applicable at the sheath entrance (e.g. pre-sheath), $n_{i,s} = n_{e,s} = n_s$. According to equation2.2, equation2.4 and equation2.5, we can obtain:

$$\frac{d^2\left(V_s - V\right)}{dx^2} \approx \frac{en_s}{\epsilon_0}\left[\frac{e}{k_B T_e} - \frac{1}{2V_s}\right]\left(V_s - V\right) \tag{2.6}$$

Here, a Taylor expansion at $x = x_s$ is used in equation 2.6. If the physical solution for V is non-oscillatory, the expression $\frac{e}{k_B T_e} - \frac{1}{2V_s}$ must be negative, so $V_s \geq -\left(k_B T_e\right)/\left(2e\right)$ [32]. Based on equation 2.3 a constraint of ion velocity is given at the sheath entrance:

$$v_{i,s} \geq \sqrt{\frac{k_B T_e}{m_i}} \tag{2.7}$$

The simplest possible case is to assume the ion temperature $T_i = 0$ as done in the above derivation. In this case, all the ions are assumed to start at a single location upstream of the sheath edge with zero velocity. The ions are assumed to fall collisionlessly through a pre-sheath potential drop. $v_{i,s}$ is the ion sound speed marked as 'c_s' [19][32]:

$$C_s = \sqrt{\frac{Zk_B T_e + \alpha k_B T_i}{m_i}} \tag{2.8}$$

Z is the ion charge number; $\alpha = 1$ is for isothermal flow, $\alpha = 5/3$ is for adiabatic flow with isotropic pressure and $\alpha = 3$ is for one dimensional adiabatic flow [34]. As a result, ions can be at least accelerated to sound speed at the sheath entrance. This constraint is called the Bohm criterion.

2.1.2 Hydrogen heat transport in the divertor

According to the different transports of heat in the divertor (e.g. convection and conduction), there are two modes of divertor heat transport: sheath-limited heat transport and conduction-limited heat transport [19].

In the sheath-limited regime, the SOL is characterized by:

(1) The electron temperature and ion temperature are constant along the flux tube;

(2) Cross-field transport of particles from the main plasma is the only particle

source in the SOL;

(3) There is no momentum and power losses in the SOL;

(4) The sheaths at the divertor target are the only particle and heat sinks;

(5) The SOL collisionality (e.g. ration of connection length to mean free path) is weak.

This case implies the SOL collisionality may be too weak to maintain the electrons Maxwellian in the sheath-limited regime. If it is not Maxwellian, the distribution will still be constant along SOL, since the mean free paths for self-collisions is larger than the system length (or connection length in this case). Therefore in this situation, the heat transmission properties of the sheath determine the temperature along the SOL[19][35] and heat transport along the SOL is mainly carried by parallel convection.

As the plasma density in the divertor increases, the mean free paths for self-collisions will become smaller than the system length and will cause temperature gradients along SOL. In the case of high divertor collisionality and a large connection length, heat conduction will become the main heat transport process [19]. In such a conduction-limited regime, the pressure determined by both temperature and density is approximately constant along the SOL. If the density near the target increases, the temperature in the same place may decrease in order to keep the pressure constant. The density can be increased by raising the upstream density or by introducing a particle source near the target (for example neutral hydrogen recycling or a gas puff), which intensifies the ionisation and thus leads to an additional plasma flux near the target that further accelerates the recycling process. When the solid surface becomes fully saturated with neutrals (e.g. hydrogen atoms and molecules), a steady state can be achieved that no external source of fuel is required. In this case, the plasma outflow is automatically matched to the neutral inflow rate [36][19]. Consistent with convection not being important in this case, the recycle ionisation is assumed to be very close to the solid surface [19]. Additionally, incoming ions will recombine with electrons near the target to produce neutral atoms and molecules. This process releases the potential energy as heat to the solid surface. For hydrogen, the ionisation energy $E_{pot}^{ion} = 13.6\text{eV}$ and dissociation energy is $E_{pot}^{diss} = 4.5\text{eV}$. The total is $E_{pot} = E_{pot}^{ion} + E_{pot}^{diss} = 18.1\text{eV}$. The power density deposited on the solid surface containing the kinetic and potential energy is:

$$q_{tot} = (\gamma k_B T_e + E_{pot})\,\Gamma_s \tag{2.9}$$

The strongly radiating regime is another important mechanism for reducing the heat load in the divertor. As the electron temperature T_e decreases in the divertor, the hydrogenic recycling becomes more intensive and produces more neutral atoms, which increase the associated radiative losses [19][32]. It happens mainly because more excitation occurs before ionisation at low electron temperatures and volumetric recombination also provides the radiated power when T_e becomes very low (below a few eV). Furthermore, the plasma-surface interaction can produce low-Z impurities (e.g. carbon) in both the SOL and the divertor. These intrinsic impurities, which have a large radiation function at low T_e (about 10eV), can radiate a large fraction of power entering the SOL [37]. If the radiating area is close to the targets, it can effectively reduce the heat flux on the target. In this work, it is indeed studied that for MAST-U conditions the intrinsic carbon radiation accelerates the reduction of target temperature and target plasma flux (Chapter 4).). In some tokamak with a metallic first wall (e.g. tungsten), the radiation function of the intrinsic impurity become larger at higher temperatures but smaller at lower temperatures. It may cause a problem: unexpected core radiative losses. If the intrinsic impurity radiation and hydrogen radiation still cannot reduce heat load to an acceptable level, extrinsic impurity may be seeded into the divertor [35][38][39][40][41]. Section 2.2.5 will further discuss the divertor impurity radiation caused by intrinsic and extrinsic impurities.

Although a reduction of the temperature leads to a lower heat flux density on solid surface, it may still be not sufficient for safe operation in large scale devices, such as ITER and DEMO [12][13][14][42]. The particle fluxes reaching the surface are predicted to be very high such that the potential power deposited on the surface becomes crucial. As a consequence, both the temperature and the particle flux to the surface needs to be decreased for a safe operation. Understanding the mechanism leading to the reduction of target particle flux is also the main purpose of this work.

2.2 Atomic and molecular physics in tokamak divertor

Understanding the role of the atomic and molecular processes in divertor is crucial to study divertor detachment. This part specifically discusses the atomic and molecular physics, including atomic and molecular databases (section 2.2.1), reaction rates of crucial plasma-atom and plasma-molecule collisional reactions (section 2.2.2), hydrogen excitation radiation (section 2.2.3), hydrogen photon emission (section 2.2.4 and divertor impurity radiation (section 2.2.5).

2.2.1 Atomic and molecular databases

The reaction rates and emission rates for the analysis of atomic and molecular processes in divertor conditions can be obtain via several databases, such as ADAS, AMJUEL, HYDHEL and YACORA [43][44][45][46]

ADAS is a general collisional radiative mode that calculates the population densities (or the population coefficients) of the energy levels of various particle species. ADAS models the population densities through solving a large system of equations representing a differential equation of the populational densities that are relevant to the various reactions including electron collisional transitions; radiative decay[43][35]; collisional ionisation and recombination (radiative, dielectronic and threebody are all included). The atomic reaction rates (e.g. ionisation (named SCD in ADAS) and recombination (ACD)) can be calculated by applying certain groupings of terms in the differential equation, which takes a collection of processes into account to make up the reaction rates[43][30]. ADAS is also able to determine the line emission coefficients (PEC for photon emission) and emissivities for the most energetic lines in the spectrum, thus it can be applied to provide radiation power loss (PLT for excitation and PRB for recombination and Bremsstrahlung) [47]. These parameters are functions of temperature and density. ADAS accounts for the atomic collisional and radiative reactions in detail, which could help understanding of atomic processes in the detachment research. But it cannot be used to analyse the molecular process.

YACORA is another collisional radiative mode, which can be used to determine these population densities of excited states of specific atoms or molecules in the considered plasma (e.g. hydrogen and helium)[46]. YACORA solves a system of equations that describes how the density of each excited state evolves in time as a consequence of processes that populate or depopulate such excited levels [46]. The collection of processes in the equations includes spontaneous emission, electron collision excitation, two-body recombination, three-body recombination and ionisation. Similar to ADAS, the population densities obtained by YACORA are functions of temperature and density. The advantage of a generalised collisional radiative model is that both ground and metastable populations are tracked, which is important for impurity studies. But YACORA only includes one impurity (Helium) in its model, it will no longer be available for the study of other impurity species.

HYDHEL [45] and AMUEL [44] are two important databases containing data relevant to plasma-atom and plasma-molecule interactions. In the HYDHEL database, the cross-section and reaction rate coefficient are calculated by a single polynomial function of electron temperature [45]. A double polynomial function of energies of the two collided particles are applied for calculating charge exchange rate coefficients. It means the rate coefficients of crucial reactions (e.g. ionisation, recombination and dissociation) have no dependency of electron density, which should play a crucial role in the collisional and radiative reactions. Taking into account the density dependence of the plasma-neutral interactions is important because the electron density in the divertor can significantly change depending on the operating conditions and is sensitive to the variation of the upstream density, heat and particle flux. When divertor detachment is triggered by increasing the upstream density, the peak electron density in divertor will be several times larger than during attached conditions, while the divertor electron density can decrease when the divertor is fully detached. Thus it is essential to consider electron density variation in the calculation of rate coefficients and hydrogenic radiation loss.

The AMJUEL database contains extensive information on the cross-sections, rate coefficients, cooling rates and population densities, which have a dependency of both electron temperature and density. Its reaction list covers the crucial atomic and molecular processes for detachment research, including electron-impact and ion-impact reactions, hydrogenic excitation radiation and hydrogenic photon emission [44][48][49]. Thus using the AMJUEL database for the numerical modelling of divertor detachment could avoid the huge error caused by the missed density dependency in HYDHEL and could provide the details of molecular processes for detachment research that ADAS cannot give.

In this work, ADAS is employed to provide impurity radiation (e.g. carbon and neon) in numerical simulations, while the reaction rate coefficients and the population coefficients are obtained from Amjuel.

2.2.2 Rate coefficients of plasma-atom and plasma-molecule collisional reactions

To understand the complex hydrogenic atomic and molecular processes, AMJUEL database predicts the rate coefficients for the collisional reactions for both hydrogen atom and molecule, which are shown as a function of electron temperature in figure 2.1, figure 2.2 and figure 2.3. Each reaction has three curves, which represents the rate coefficient at three different electron densities (e.g. $n_e = 5 \times 10^{18}/\mathrm{m}^3$, $n_e = 5 \times 10^{19}/\mathrm{m}^3$ and $n_e = 5 \times 10^{20}/\mathrm{m}^3$). In figure 2.1, the ionisation, charge exchange and recombination rate coefficients present the basic processes occurring during divertor detachment [19][35]:

(1) Ionisation and charge exchange are the dominant atomic processes at higher T_e, and few neutral atoms could exist without any external neutral sources;

(2) Once T_e drops ($T_e < 10$eV), the ionisation rate coefficient drops, and charge exchange becomes the most significant atomic process;

(3) if T_e goes down further in a deeply detached case, recombination becomes more significant at $T_e < 1$eV

The effective volume ionisation and recombination rates, which are important for describing detached plasma, are affected by both the rate coefficients. One should note, however, that these are reaction rate coefficients and not volume rates (which needs to multiply the reaction rate coefficients by the density of one reacted particle).

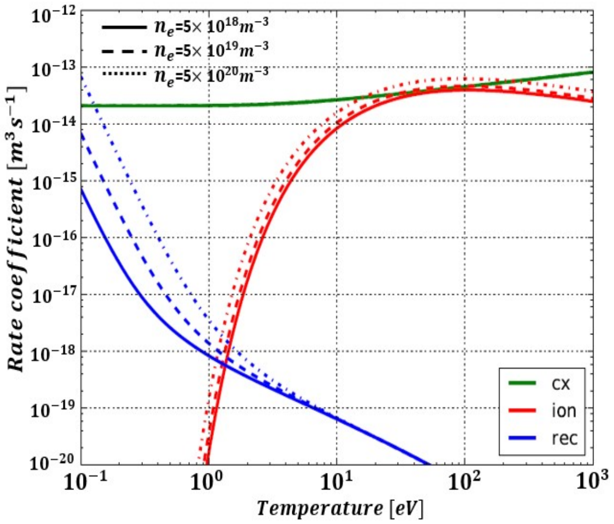

Figure 2.1: Hydrogen atom effective ionisation, charge exchange and recombination rate coefficients as a function of electron temperature for electron density $n_e = 5 \times 10^{18}/\mathrm{m}^3$,$n_e = 5 \times 10^{19}/\mathrm{m}^3$ and $n_e = 5 \times 10^{20}/\mathrm{m}^3$ [48]

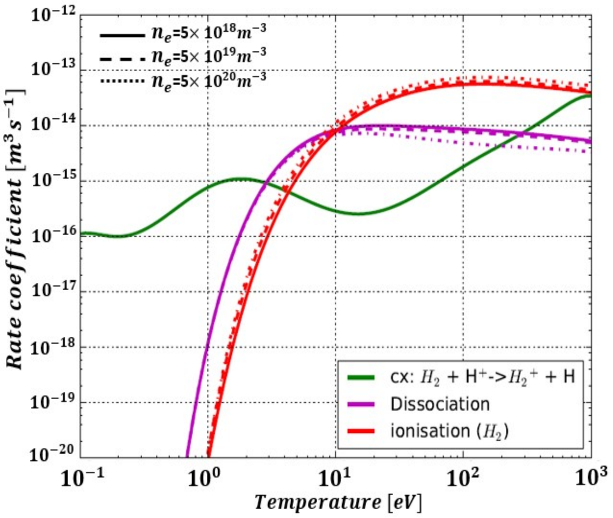

Figure 2.2: Hydrogen molecule effective charge exchange, dissociation, and non dissociative ionisation rate coefficients as a function of electron temperature for electron density $n_e = 5 \times 10^{18}/\mathrm{m}^3$,$n_e = 5 \times 10^{19}/\mathrm{m}^3$ and $n_e = 5 \times 10^{20}/\mathrm{m}^3$ [48]

Hydrogen molecules (H_2 and H_2^+) may also play an important role in momentum losses in the divertor, especially in the detached case with high recycling rates or external neutral sources [48][49]. The elastic collisions or charge exchange between neutral molecules and plasma ions may effectively reduce the plasma ion momentum near the target [38]. As shown in figure 2.2, molecular charge exchange $H^+ + H_2 \to {H_2}^+ +$ H is the main molecule sink at low temperatures $T_e \sim 3.0$eV. But when T_e increases to about 10eV, both dissociation $e + H_2 \to H + H + e$ and non-dissociative ionisation $e + H_2 \to 2e + {H_2}^+$ gradually become the more important molecule sink over charge exchange. Once $T_e > 10$eV, the rate coefficient curves shows that non-dissociative ionisation is the main molecule sink.

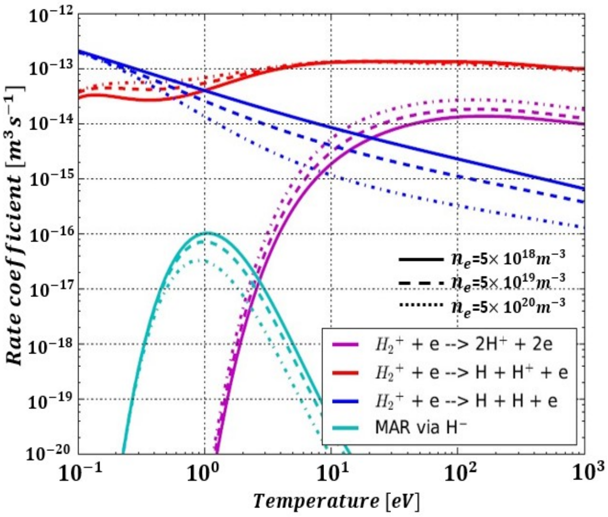

Figure 2.3: Rate coefficients of effective dissociative ionisation (purple), dissociative excitation (red), dissociative recombination (blue) and molecular activated recombination (MAR) via H^-, as a function of electron temperature for electron density $n_e = 5 \times 10^{18}/m^3$,$n_e = 5 \times 10^{19}/m^3$ and $n_e = 5 \times 10^{20}/m^3$ [48]

The charged molecule (H_2^+) is an important product of molecule collisional reactions (primarily via non-dissociative ionisation and molecular charge exchange) [38][48][46]. There are three channels for the dissociation of H_2^+: dissociative excitation ($e + {H_2}^+ \to e + H^+ + H$), dissociative ionisation ($e + {H_2}^+ \to 2e + H^+ + H^+$) and dissociative recombination ($e + {H_2}^+ \to e + H + H$), which contribute to recombination and ionisation [50])[51]. Through comparing the rate coefficients in figure 2.3 to the coefficients of non-dissociative ionization and molecular charge exchange in figure 2.2, the rate at which H_2^+ is dissociated is generally larger than the rate at which H_2^+ is produced, therefore the density of H_2^+ should be small. Both H_2^+ and H^- are the channels for molecular activated recombination (MAR), which may lead to large momentum losses in detached cases [38][52][53][54].But the rate coefficient of MAR via H^- is small compared to the H_2^+ reactions.

A comparison (figure 2.4) can be made for investigating the density of different particle species at which systems with different electron temperatures reach a thermal equilibrium (H_2, H_2^+, H, H^+). AMJUEL databse provides the reaction rate coefficients of atomic and molecular reactions (shown in figure 2.1, 2.2 and 2.3) for this comparison and the total density is fixed at $N_{total} = 1 \times 10^{20} \mathrm{m}^{-3}$. The result shows that the curves of ion density and atom density cross at about 1eV, which matches the cross of the rate coefficients of ionisation and recombination in figure 2.1. This result matches the result of the SAHA ionisation equation [55]. The density of molecular species (H_2, H_2^+) is found much smaller than the density of atomic species, even though their sinks (e.g. dissociation, non-dissociative ionisation and molecular charge exchange) decrease at lower temperatures. The density ratio $\frac{n_{\mathrm{H_2}^+}}{n_{\mathrm{H_2}}}$ is about 0.02 at the electron temperatures lower than 5eV (figure 2.4). But in a detached divertor, molecules can be injected into the divertor volume by localized gas puffing or can be produced through recycling at the target. As the molecular density increases, more H_2^+ will be produced and thus the H_2^+ collisional and radiative reactions will become more important. As a result, in such conditions this charged molecule plays a bigger role in the dynamics of detachment (e.g. influence particle balance).

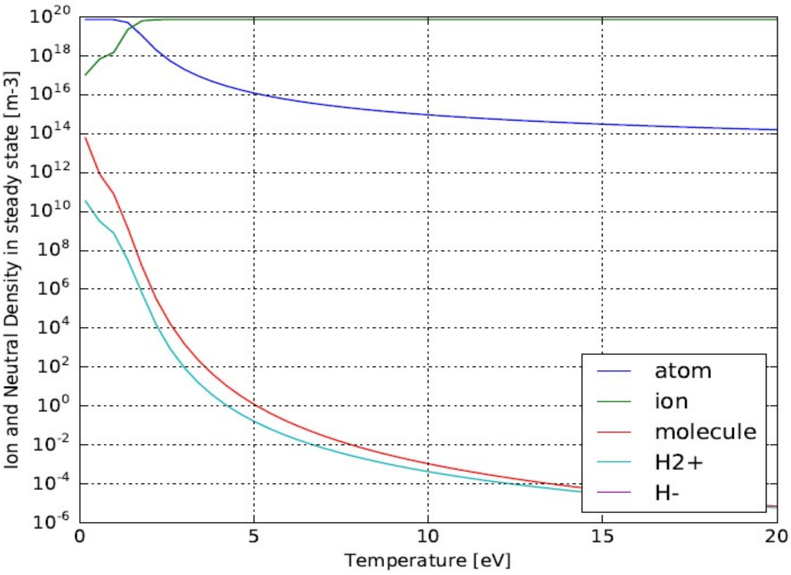

Figure 2.4: The density of different particle species at which systems with different electron temperatures reach a thermal equilibrium (H_2, H_2^+, H, H^+)

2.2.3 Hydrogen excitation radiation

Besides collisional reactions, the hydrogen atom radiation caused by atom-plasma or molecule-plasma interactions is also crucial for divertor physics[38][56][57]. It contributes a significant energy loss from the plasma in divertor volume, and greatly affects the target flux in terms of particle and power balance. Summing the radiation arising from line emission according to the photon emission coefficients (PEC) from ADAS can provide information on the hydrogenic radiative power loss.

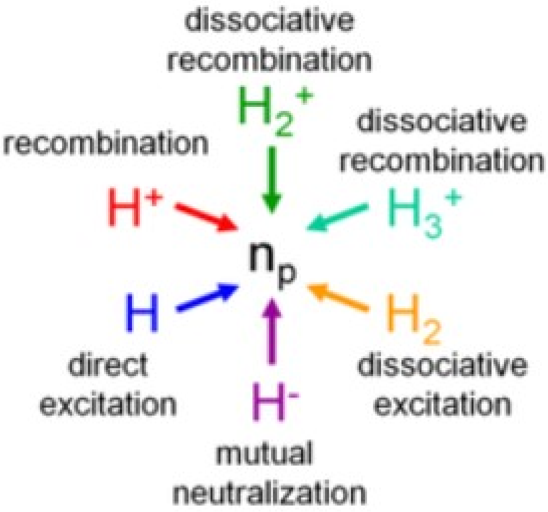

Figure 2.5: The channels to generate excited hydrogen atoms. Figure from [46]

According to the collisional and radiative models in YACORA [46], there are 6 channels to generate excited hydrogen atoms (figure 2.5). Direct electron-impact excitation (via H) and electron-ion recombination (via H^+) are atomic excitation channels. Dissociation (via H_2), dissociative recombination (via H_2^+ and H_3^+) and mutual neutralization (via H^-) are molecular excitation channels, since they generate excited atoms after molecular break-up. However, the ADAS cannot be used to analyse the contribution of different excitation channels to the total radiative power loss.

The AMJUEL database provides another way to model the hydrogenic radiative power loss by using the population coefficients of the different channels (section 3.4) [44][48]. Thus, this approach can be used to analyse the radiation power loss though different channels separately.

The emissivity $L = \varepsilon_{rad,pq}/n_e N_0$ (erg $*$ cm^3/s) corresponding to the low-n and medium-n Lyman lines (e.g n=2-6 → 1) are shown in figure 2.6 for the excitation channels at three different electron densities. $\varepsilon_{rad,pq}$ is the radiation power by the excited atom transiting from state p to q. N_0 is the density of the reacting species (e.g. H for direct excitation and H^+ for recombination). Since the density of H_3^+ is tiny in divertor conditions, it is ignored in this part. As the channel's names imply, the radiative reactions always happen together with the corresponding collisional reactions. Qualitatively, the curves of the ionisation rate coefficient and recombination rate coefficient shown in figure 2.1 are similar to the corresponding emissivity curves in figure 2.6 (a)-(c). Similarly, the curves of emissivity coefficient via dissociation channel (H_2) and dissociative recombination channel (H_2^+) correspond to the rate coefficients of dissociation in figure 2.2 and dissociative recombination in figure 2.3, respectively. For the mutual neutralization excitation channel (H^-), its emissivity curve is similar to the rate coefficient of reaction 7.2.3b ($H^+ + H^- \rightarrow H^+ + H + 2e$) in Amjuel [44]

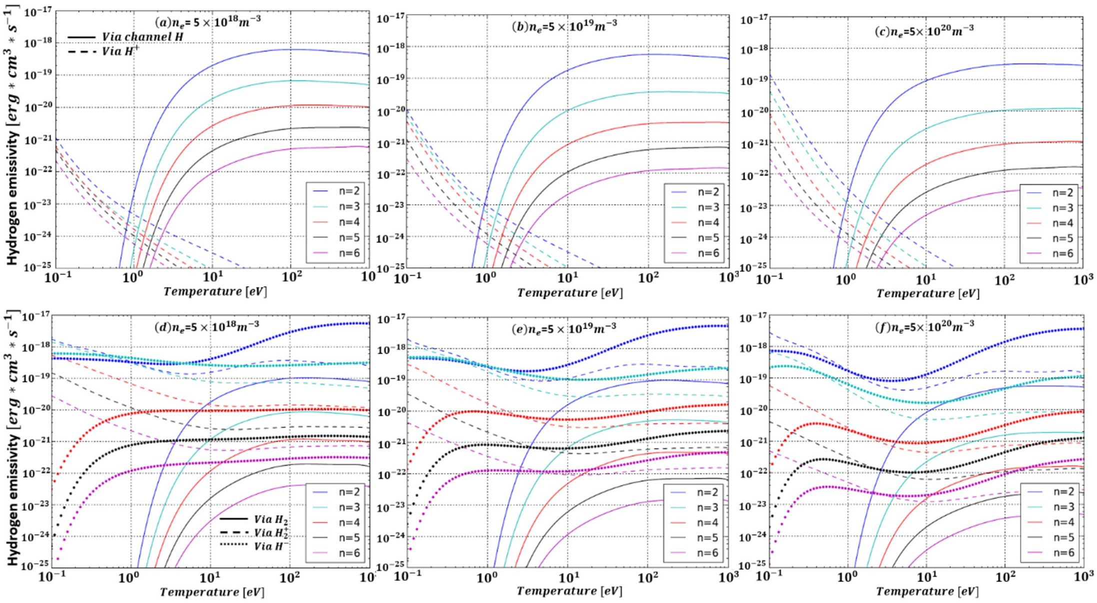

Figure 2.6: Hydrogen emissivity of the hydrogen excited atom at different energy levels (Lyman lines n=2-6 → 1) as a function of electron temperature for the electron density $n_e = 5 \times 10^{18}/\text{m}^3$, $n_e = 5 \times 10^{19}/\text{m}^3$ and $n_e = 5 \times 10^{20}/\text{m}^3$. Two atomic excitation channels (direct electron-impact excitation H and recombination H^+) and three molecular excitation channels (dissociation via H_2, dissociative recombination via H_2^+ and mutual neutralization via H^-) are shown here [48].

According to the emissivity produced by hydrogen excited atoms at different energy levels (n=2-6) , it can be seen that the deviation between the curves via direct electron-impact excitation is much larger than the one between the recombination emissions. Therefore, the intersection of emissivity for the two excitation channels is located at a larger T_e for a higher-n Lyman line [48][35]. Once the electron density increases, the direct electron-impact excitation emissivity is slightly reduced, while the emissivity via electron-ion recombination emission increases. Thus, the emission via recombination channel tends to be more significant at higher densities. Moving now to molecular emission, in figure 2.6(d)-(f), the emissivity variation between different Lyman lines is generally large for the three excitation channels considered [48]. Only the emissivity of the Lyman line $n = 3$ via H_2^+ and H^- does slightly decrease with increasing electron density, while the others change little. Two things should be noted for the molecular excitation channels: (1) due to the small densities, the excitation via H_2^+ and H^- is less important at high temperatures, even though the emissivity via H_2^+ and H^- is greater than the other channels. They may become important in the divertor as their densities greatly enhance with the drop of temperature $T_e < 3\text{eV}$ or with external fuelling (gas puffing). (2) Having one channel dominates over the other channels does not imply that its reaction rate dominates over the other's reaction rate [35].

2.2.4 Hydrogen photon emission

Similar to hydrogen emissivity in section 2.2.3, the photon emission coefficient can also be obtained using the population coefficient of the different excitation channels [48]. Figure 2.7 shows photon emission coefficients of the hydrogen excited atom at different energy levels (Balmer lines 3-6 → 2) as a function of electron temperature for the electron density $n_e = 5 \times 10^{19}/\text{m}^3$. compared to figure 2.6, it is found that the Balmer lines have a similar behaviour of the emissivity, for both atomic channels and molecular channels.

H_{alpha} emission (Balmer lines 3 →2), the brightest hydrogen line in the visible spectral range, is crucial for tokamak experiment diagnostics, and conveys information on neutral density and neutral-plasma interactions. The blue curves in figure 2.7

present that the emission coefficients of H_{alpha} photon emission coefficients via H_2^+ and H^- are larger than the other channels. But due to their small densities, H_2^+ and H^- channels are less important than the direct excitation channel at high temperatures. The photon emission via H_2^+ and H^- channel may also become important in that case with a high recycling rate or with external fueling. In particular, for H_{alpha} photon emission, H_2^+ and H^- are expected to be the dominant excitation channels.

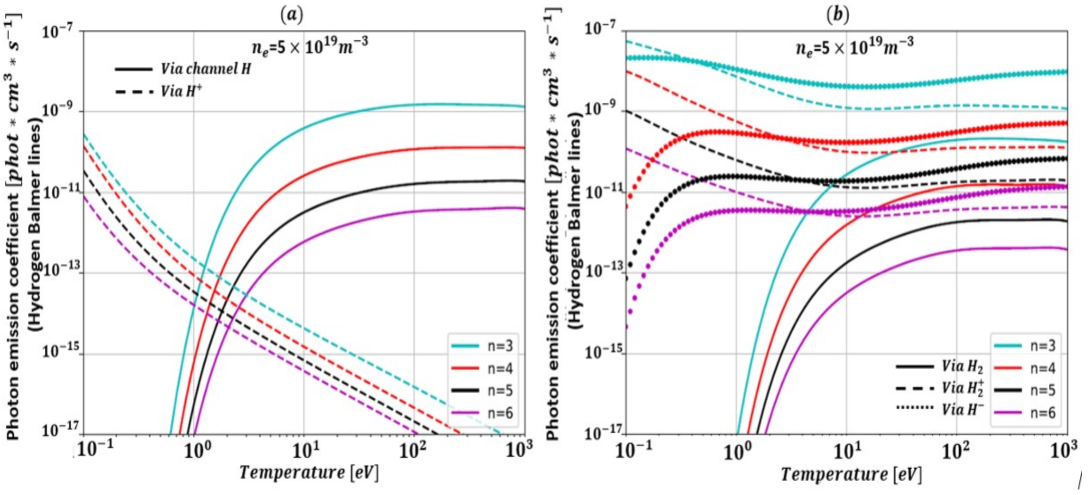

Figure 2.7: Photon emission coefficient of the hydrogen excited atom at different energy levels (Balmer lines 3-6 → 2) as a function of electron temperature for the electron density $n_e = 5 \times 10^{19}/\mathrm{m}^3$. (a) Two atomic excitation channels and (b)three molecular excitation channels are shown here [48]

2.2.5 Divertor impurity radiation caused by intrinsic impurity (carbon) and extrinsic impurity (neon)

As discussed in section 2.2.1, ADAS can be used for analysing impurity radiation, including excitation radiation (PLT), recombination (PRB) and charge exchange between hydrogen and the impurity (PRC). In general, PLT could be the dominant radiation coefficient for carbon, thus some works just focus on the PLT coefficient to calculate the carbon radiation loss. Figure 2.8 considers all these coefficients and investigates the radiative power loss rates (Wm^3) of carbon as a function of plasma temperature. It shows that the peak of the radiative power loss rate is located at temperatures around 10eV, where powerful carbon radiation is most possibly to be produced. But carbon radiation may be less important at low temperatures due to the

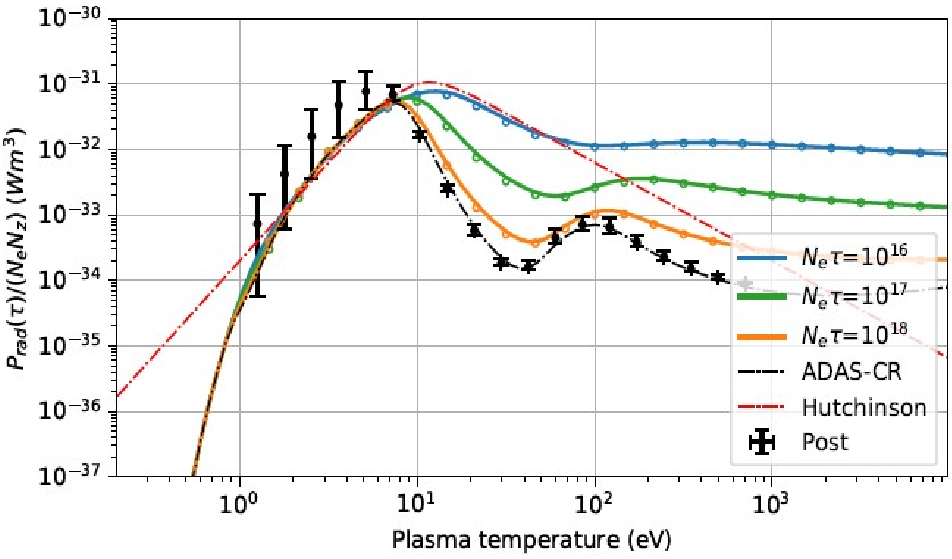

Figure 2.8: Radiative power loss rates (wm^3) of carbon as a function of plasma temperature (electron density is fixed $n_e = 1 \times 10^{19}/\text{m}^3$). The collisional-radiative result for P_{rad} from ADAS is marked as ADAS-CR, while results with different refuelling rates are marked by the $n_e\tau_{recy}$; The collisional-radiative equilibrium is compared to the result from Post's work [58][59]. The error-bars are given as the mean and standard deviation across the models. The empirical result given by Hutchinson is also presented [59][60]

small radiation loss rate. Figure 2.8 also compares the results obtained by different approaches. It is found that the ADAS and the Post's work provide similar radiative power loss rates when T_e > 10eV while Hutchinson's result is much higher. When T_e < 10eV the ADAS result becomes lower than Post's work. Hutchinson's result is similar to the ADAS result between 2eV and 10eV and then gradually becomes higher than the ADAS result with the decrease of temperature. Thus Hutchinson's empirical result might overestimate the radiative power loss of carbon, and might significantly influence the power balance in divertor.

As discussed in section 1.4, there are two approaches to achieve divertor detachment, raising the upstream plasma density or seeding impurity in divertor. But the approach of increasing upstream density to reach detachment can be detrimental to core confinement [62] and is subject to the Greenwald density limit in tokamak [63], particularly in metal wall protected machines. Seeding impurity in the divertor could be a possible solution, which leads to volumetric radiation of the power in the edge region, the SOL and the divertor, and thus a reduction in the power reaching the

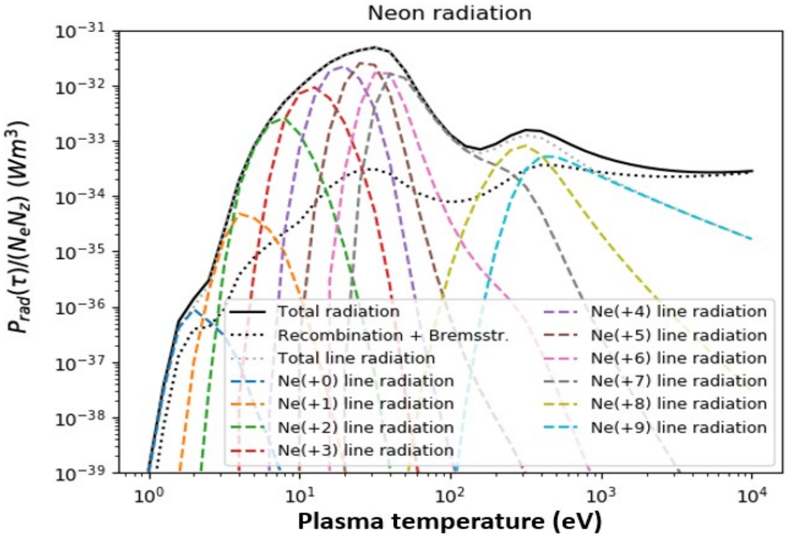

Figure 2.9: Charge resolved radiative power loss rates (wm^3) of neon as a function of plasma temperature ($n_e = 1 \times 10^{19}/\mathrm{m}^3$). The collisional-radiative result for P_{rad} from ADAS [61].

divertor targets, which in turn facilitates access to a detached regime [64]. The main candidates for this task are the noble gases (e.g. neon) since the radiative properties of noble gasses are close to those of carbon, with a high radiative efficiency for the range of temperature typically encountered in the divertor region, yet remaining relatively low in the plasma core [65][65]. Neon as an important extrinsic impurity can be injected in divertor for reducing the heat flux through radiation and trigger the divertor detachment. In order to better understand the expected neon radiation, one not only needs to know the overall content but more specifically the charge-state resolved content. Figure 2.9 presents the radiative power loss rate of neon at different charge states as a function of electron temperature. It shows that the coefficients of $\mathrm{Ne}^{3+} - \mathrm{Ne}^{7+}$ are located around the peak of total radiative power loss rate (at about 30eV). $\mathrm{Ne}^{3+} - \mathrm{Ne}^{7+}$ could be the main cooling species in divertor conditions [66]. Similar to carbon impurity, neon may also become less important when $Te < 10$eV.

In order to get a rough idea of the general radiation curves, it usually assumes that there is no transport in the data analysis (e.g. Atomic++ in section 3.3). It means that the fractional abundance (the ratio of neon density in a certain charge state by the total neon density) can be calculated by using the rate coefficient of ionisation, recombination and charge exchange recombination (see figure 2.10). However, transport could significantly influence the temperature regime in which a certain charge state can be found [35]. Thus, transport effects can be extremely important in modelling the radiation expected of a particular impurity [41][29]. In Chapter 5, we specifically analysed the parallel transport of the neon cooling species and effect of parallel force balance on their density profiles.

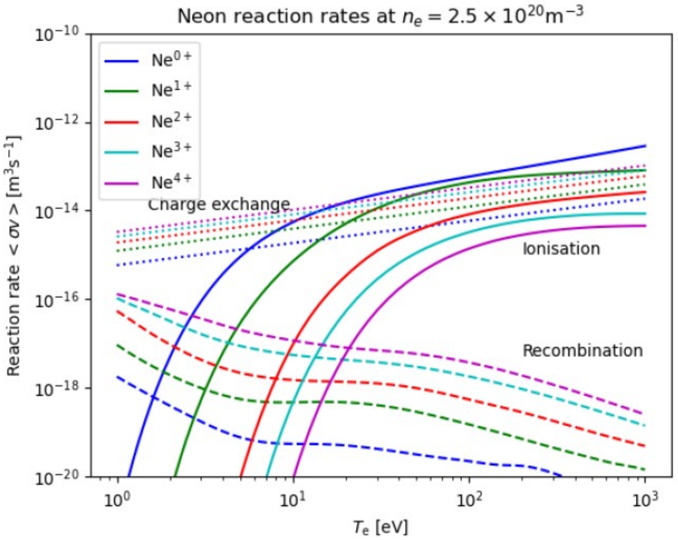

Figure 2.10: Reaction rates for Neon (charge state from $n = 0$ to $n = 5+$) at a density $n_e = 2.5 \times 10^{20}/\mathrm{m}^3$. The Solid represents ionisation, the dashed is recombination, and the dotted is charge exchange recombination.

2.3 The simplified Two Point Model of the divertor SOL

The two point model is a simplified analytical model for divertor research. The model is simple, but it is able to explain general trends and help build insight in the divertor SOL physics [19][36][67]. As figure 2.11 shows, the divertor SOL can be straightened out as a 1D linear structure, since the parallel gradients are usually small at locations far from the targets. Some assumptions need to be made for the straightened SOL: (1) Toroidal curvature is neglected; (2) Parallel transport is much more important than perpendicular dynamics. The upstream (denoted by ‘u’) is the location where the heat flows into SOL from the confined plasma. It could be taken at any place along the sepratrix and there is little change when the upstream is located at a different place. The target is denoted by ‘t’ at the end of field line. Three equations are used in the Two Point Model which represent pressure balance, parallel heat conduction

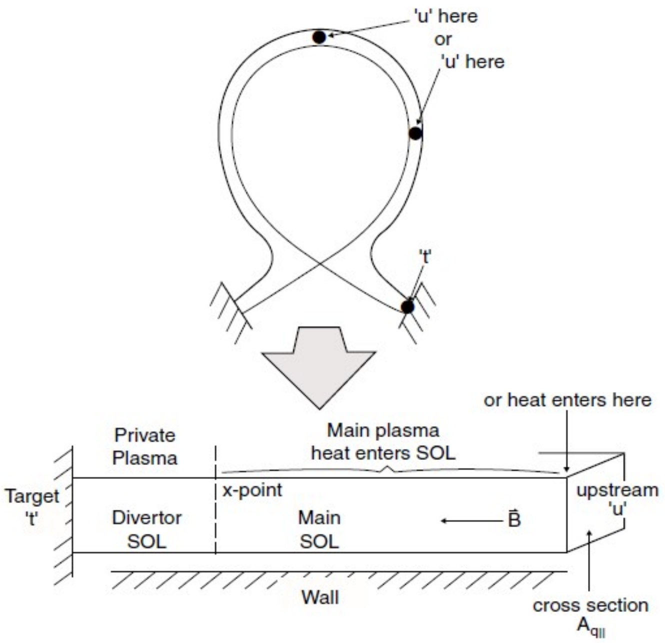

Figure 2.11: For purposes of simple modelling, the poloidal divertor SOL is straightened out in a 1D model [19]

and the target sheath conditions, in order to construct a set of analytic relationships linking the upstream and the target. It is usually assumed that [19][32][35]:

1. The divertor SOL is straightened out to be a 1D structure.

2. Ion-neutral friction is ignored along the SOL.

3. There are no viscous effects.

4. Radiation losses along the SOL are neglected.

5. The neutrals recycling from the targets are immediately ionized in front of the target.

6. The influence of ionisation on the flow profile is ignored.

7. Parallel heat conduction is the only heat transport process.

8. The total pressure (including static pressure $(nkT_e + nkT_i)$ and dynamic pressure(mnv^2)) is constant along a field line. $n_e = n_i = n$ and v is the sound speed of ion.

9. There is no cross-field particle and momentum transport.

2.3.1 The basic two point model

Based on the assumptions listed in the previous section, the total pressure (including static pressure and dynamic pressure) is assumed to be constant along a field line. T_e is assumed to be equal to ion temperature T_i. So the static pressure $n_e kT_e + n_i kT_i = 2nkT$ and the dynamic pressure is mnv^2. v is the sound speed of ion based on T. The total pressure is $2nkT + mnv^2$. Since the total pressures at the upstream and the target are the same, we get:

$$n_t \left(2kT_t + mv_t^2\right) = 2n_u kT_u \tag{2.10}$$

Here, we assume no dynamic pressure at upstream. In an isothermal fluid mode with a particle source proportional to the plasma density n, the plasma fluid velocity could not exceed the isothermal sound speed, without singularities arising. Thus based on the Bolm criterion in section 2.1, $c_s = \sqrt{\frac{2T}{m_i}}$. The dynamic pressure at the target is equal to $2n_tT_t$, so equation 2.10 can be rewritten as:

$$n_u T_u = 2n_t T_t \tag{2.11}$$

According to the assumption of no power losses along the SOL, the heat flux unchangeably flows from upstream to the target. The power density transmitted to the target can be writtern as:

$$q_{\parallel} = \gamma n_t T_t c_{st} \propto n_t T_t^{3/2} \left(= p_t T_t^{1/2} \right) \tag{2.12}$$

γ here is the sheath power transmission coefficient, which represents the intensity of the accelerated plasma hitting the target through the sheath. Equation 2.12 indicates that the heat flux reaching the target is determined by the pressure and temperature at the target. Since it is assumed that parallel heat conduction is the only heat transport process, the parallel heat conductivity is written as $\kappa_{\parallel,e} = {v_{th,e}}^2 \tau_e$ where the thermal velocity of electron is $v_{th,e} \propto {T_e}^{1/2}$ and the electron collision time is defined as $\tau_e \propto {T_e}^{3/2}$, resulting in $\kappa_{\parallel,e} \propto {T_e}^{5/2}$. Thus the classic (Spitzer) parallel heat conduction density is written as [19][68][9]

$$q_{\parallel} = -\kappa_0 {T_e}^{\frac{5}{2}} dT/dx \tag{2.13}$$

Here the thermal conductivity is defined as $\kappa_0 {T_e}^{5/2}$, where κ_0 is the electron parallel heat conductivity coefficient. Then integrate the equation 2.13 along the field line from upstream to the target in order to obtain a relation between the temperatures at upstream and at the target (shown in equation 2.14.

$$q_{\parallel} = -\kappa_0 T^{\frac{5}{2}} \frac{dT}{dx}$$

$$\longrightarrow T^{\frac{5}{2}} dT = -\frac{q_{\parallel}}{\kappa_0} dx$$

$$\longrightarrow T_u^{\frac{7}{2}} = T_t^{\frac{7}{2}} + \frac{7 q_{\parallel} L}{2\kappa_0} \tag{2.14}$$

L is the connection length (distance along the field line from upstream to the target). The three equations of two point model are the equations 2.11,2.12 and 2.14, which related four variables n_t, n_u, T_t and T_u for a given heat flux $q_{\parallel}$.Thus if one of the four variables is given, the other variables can be calculated from the three equations. In conduction limited regime, the temperature at upstream could be much larger that the temperature at the target. Therefore equation 2.14 could be simplified as

$$T_u^{\frac{7}{2}} \approx \frac{7q_{\parallel}L}{2\kappa_0} \longrightarrow T_u = \left(\frac{7q_{\parallel}L}{2\kappa_0}\right)^{\frac{2}{7}} \tag{2.15}$$

In this situation, n_t, T_t and T_u can be directly calculated if the value of upstream density n_u is given. The three equations can be rewritten as

$$T_t = \frac{q_{\parallel}^2}{n_u^2 T_u^2}\frac{2m_i}{\gamma^2} \propto \frac{q_{\parallel}^2}{n_u^2 T_u^2}$$

$$n_t = \frac{n_u^3 T_u^3}{q_{\parallel}^2}\frac{\gamma^2}{4m_i} \propto \frac{n_u^3 T_u^3}{q_{\parallel}^2}$$

$$T_u = \left(\frac{7q_{\parallel}L}{2\kappa_0}\right)^{\frac{2}{7}} \tag{2.16}$$

The equation 2.16 shows that the target temperature T_t can be effectively reduced by increasing upstream density n_u, while n_t must become larger in order to be consistent with constant pressure along the flux tube. The heat flux at the target is determined by both the plasma ion flux at the target and the energy of each ion: $\Gamma_t = q_{\parallel}/T_t$. So the plasma ion flux at the target can be written as:

$$\Gamma_t = \frac{n_u^2 T_u^2}{q_{\parallel}}\frac{\gamma}{2m_i} \propto \frac{n_u^2 T_u^2}{q_{\parallel}} \tag{2.17}$$

Here it is assumed that both volumetric power loss and convective heat transport are ignored [19][35]

2.3.2 Corrections to the Two Point Model using loss factors

According to the strong assumptions made in the previous section, various processes (e.g. convection transport, radiation, and momentum losses) are excluded in the basic two point model. However, these missing processes are usually crucial for the divertor physics. This section will make an extension to the basics two point model by adding correction factors in the equations, in order to provide estimates for the effects of these missing processes. Volumetric power losses due to line radiation in the SOL $q_{\text{rad}}^{\text{SOL}}$ [Wm^{-2}] (either by impurities or recycled neutrals) and charge exchange collisions $q_{\text{cx}}^{\text{SOL}}$ [Wm^{-2}] can be included in equation 2.18. f_{power} is a power loss factor representing the proportion of power loss in the total heat flux [19][32]

$$q_{\mathrm{rad}}^{\mathrm{SOL}} + q_{\mathrm{cx}}^{\mathrm{SOL}} \equiv f_{\mathrm{power}} q_{\|} \tag{2.18}$$

As a result, $q_{\|}$ and q_t can be decoupled in equation 2.19:

$$\left(1 - f_{\mathrm{power}}\right) q_{\|} = q_t = \gamma k T_t n_t C_{st} \tag{2.19}$$

Although parallel conduction is the dominant heat transport process in the SOL, parallel convection still plays a role. Thus a convection factor (f_{conv}) that determines the heat fraction carried by convection is introduced in equation 2.20 [19][32].

$$q_{\|\mathrm{cond}} = \left(1 - f_{\mathrm{conv}}\right) q_{\|} \tag{2.20}$$

Thus equation 2.14 can be rewritten as:

$$T_u^{\frac{7}{2}} = T_t^{\frac{7}{2}} + \frac{7}{2} \frac{\left(1 - f_{\mathrm{conv}}\right) q_{\|} L}{\kappa_0} \tag{2.21}$$

Strictly, it should be integrated from upstream to the entrance of the ionization zone as the heat in this zone is then convected. But since convection is a very effective transport process and the ionization zone is just a very thin layer, it is assumed that the temperature at the entrance of the zone is equal to the target temperature, which is much lower than the temperature at upstream [19][32]. Thus equation 2.21 can be simplified to:

$$T_u^{\frac{7}{2}} \approx \frac{7}{2} \frac{\left(1 - f_{\mathrm{conv}}\right) q_{\|} L}{\kappa_0} \tag{2.22}$$

When the temperature becomes very low near the target, momentum losses will be significant. In order to account for momentum losses by frictional collisions between ions and neutrals, viscous forces and volume recombination, a momentum loss factor f_{mom} is introduced [19][32]. With this, the pressure conservation (equation 2.11) should be revised to:

$$2 n_t T_t = \left(1 - f_{\mathrm{mom}}\right) n_u T_u \tag{2.23}$$

Depending on the corrected three equation 2.19, 2.22 and 2.23, the density, temperature and plasma flux reaching the target can be give as below:

$$n_t = \frac{n_u^3}{q_\parallel^2}\left(\frac{7q_\parallel L}{2\kappa_0}\right)^{\frac{6}{7}}\frac{\gamma^2 e^3}{4m_i}\frac{(1-f_{\mathrm{mom}})^3(1-f_{\mathrm{conv}})^{\frac{6}{7}}}{(1-f_{\mathrm{pow}})^2} \tag{2.24}$$

$$T_t = \frac{q_\parallel^2}{n_u^2}\left(\frac{7q_\parallel L}{2\kappa_0}\right)^{-\frac{4}{7}}\frac{2m_i}{\gamma^2 e^2}\frac{(1-f_{\mathrm{pow}})^2}{(1-f_{\mathrm{mom}})^2(1-f_{\mathrm{conv}})^{\frac{4}{7}}} \tag{2.25}$$

$$\Gamma_t = \frac{n_u^2}{q_\parallel}\left(\frac{7q_\parallel L}{2\kappa_0}\right)^{\frac{4}{7}}\frac{\gamma e^2}{2m_i}\frac{(1-f_{\mathrm{mom}})^2(1-f_{\mathrm{conv}})^{\frac{4}{7}}}{(1-f_{\mathrm{pow}})} \tag{2.26}$$

When the upstream density increases, the hydrogen recycling becomes more intensive due to the increased particle flux. This high recycling will remove power from the SOL through line hydrogenic radiation. Thus, the power loss factor f_{power} is no longer negligible, which directly leads to a reduction of the target heat flux (equation 2.19). However the intensive recycling near the target can produce more neutrals, which are fast dissociated and then ionised to be plasma ions, thus the target particle flux may increase as well. Another commonly used method to increase the radiated power in the SOL is impurity seeding such as neon and nitrogen [19][32]. A further effect of the radiation losses is to decrease the target temperature and to increase the target density and particle flux. In order to reduce the target flux, the ratio of conducted to convected heat flux must change $f_{\mathrm{conv}} > 0$ or the momentum losses must occur in the divertor $f_{\mathrm{mom}} > 0$.

2.4 Understanding of divertor detachment

2.4.1 The detached regime

In general, divertor detachment is characterized by (1) the reduction of the surface heat load, (2) the reduction of plasma ion flux at the target and (3) a pressure drop at the target [19][69]. As discussed in the basic two point model, increasing collisionality (or conduction) and radiative losses is able to reduce both the temperature and the heat flux at the target. However it is insufficient to reduce the plasma ion flux reaching the target. According to the equation 2.26, momentum losses, power losses or a changeable ratio of conducted to convected heat flux are required to achieve the divertor detachment. Although the pressure at upstream is still constant, the reduction of plasma ion flux at the target requires decreasing the target pressure, therefore a pressure gradient near the target will be developed along the field lines [68][19].

The main mechanisms which remove momentum are ion-neutral collisions (e.g. charge exchange) and recombination. These two processes dominate with respect to the ionization at temperatures about 5eV and 1.5eV respectively. These low temperatures can be achieved by a further increase of upstream plasma density, as $T_t \propto n_u^{-2}$. In this case with such low temperatures, the potential energy (the energy for hydrogen atomic ionisation and molecular dissociation) is no longer negligible and the equation 2.19 can be revised to be:

$$(1 - f_{\mathrm{pow}})\, q_{\|} = q_t = (\gamma k_B T_t + E_{\mathrm{pot}})\, \Gamma_t \tag{2.27}$$

The total potential energy released per hydrogen ionisation and dissociation is $E_{\mathrm{pot}} = E_{\mathrm{pot}}^{\mathrm{ion}} + E_{\mathrm{pot}}^{\mathrm{diss}} = 18.1\mathrm{eV}$. When the temperature in front of the target is low enough, the recycling process at the target will become intensive to produce a large amount of the neutrals (hydrogen atoms and molecules). In this case, a cloud of neutral gas will cover the region in front of the target and undergo several elastic collisions with hydrogen ions which flow to the target [70][32]. As the masses of the neutral atom or molecule and the ion are approximately equal, the momentum transfer is very efficient and the ions will rapidly cool down to the neutral temperature. After the collisions, the neutral will either reach the surface, where it deposits its momentum, or enter the hotter recycling zone, where it will ionize and flow back to the surface, removing no momentum. After the first collision, however, the neutral will travel at approximately the ion sound speed and the following collisions do not efficiently remove momentum [19][32]. In order to maximize momentum removal, the neutral must reach the surface after each collision. The number of effective collisions is given by the mean free path for ion-neutral collisions λ_{in} and the divertor dimension (or connection length) L. Most collisions would be efficient if both lengths are of the same order and small compared to the ionization mean free path:

$$\lambda_{\text{in}} \approx L_{\text{div}} \ll \lambda_{\text{ion}} \tag{2.28}$$

The reduction of the particle flux with respect to the flux entering the gas target at the recycling zone, Γ_r is roughly:

$$\frac{\Gamma_t}{\Gamma_r} \approx \frac{\lambda_{\text{in}}}{L_{\text{gt}}} \tag{2.29}$$

L_{gt} is the length of the neutral cloud area. If the temperatures are below 5eV over a sufficient large area and the neutral density is high enough, ion-neutral collisions can provide an effective sink for momentum and particle flux [19][32]. If the temperature in the elastic collision zone falls below 1eV then electron-ion recombination (EIR) becomes important [71][72][73]. The ions flowing to the target can recombine with the electrons, directly decreasing the particle flux to the target. With constant power entering the elastic collision zone, the plasma ion flux at the target can be reduced by an order of magnitude due to recombination processes dominating [74][32]. Volumetric recombination can also arise from molecular activated recombination (MAR) [52][38][75][76], which can play a role at low temperatures during divertor detachment. MAR can be obtained through several combinations of molecular reactions[50], which is discussed in section 2.2.2. It should be noted here that recombination is a volumetric process. If the plasma flow velocity towards the target is high, the probability for recombination to occur can be low even if the temperature is reduced. Therefore in order to produce more neutrals by recombination, ion-neutral collisions are needed in order to slow down the plasma.

2.4.2 The transition from attachment to detachment

Generally, plasma density ramp (e.g. increasing upstream density) and impurity seeding are two widely used approaches to achieve divertor detachment [19][66][38]. Either the atomic and molecular processes or the impurity radiation can lead to dissipation of the intense heat flux before it reaches the divertor surface. As figure 2.12 shows, the peak divertor heat flux is significantly reduced by detachment in the experiments of DIII-D tokamak [77][78]. The general processes during the divertor transition induced by a core density ramp or impurity seeding ramp is shown as follow.

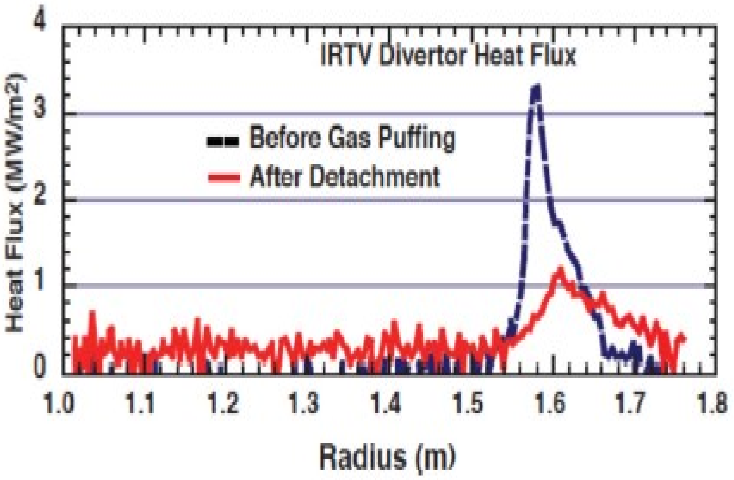

Figure 2.12: Divertor power loading in DIII-D before and after detachment [77]

Plasma density ramp or impurity seeding increases the radiation in the divertor, while the peak of radiation power is located near the target where the temperature is relatively low. When the temperature decreases below the optimum temperature for radiation (e.g. 10eV for carbon), the radiation front would move away from the target to the region with the optimum temperature for radiation (or towards X-point). The spread of neutrals or impurities towards X-point also promotes the move of radiation front. When radiative losses and the electron density further increase, the temperatures and the power reaching the target will be further reduced. The ionisation region starts to move towards the x-point and charge exchange becomes more dominant over ionisation near the target [70][35].

When the temperature at the target drops below a few eV (typically about 5eV) and the ion flux to the target starts to decrease, divertor detachment occurs. After the transition, the radiative losses/divertor densities further increase, the ionisation region moves further away from the target and the area where charge exchange dominates over ionisation increases while ultimately volumetric recombination starts to occur near the target. In the strongly detached phase, the target density may decay and thus the density front may start to move towards the X-point. When the density/core radiation is further increased, strong radiative losses in the core may occur and the plasma could disrupt due to a radiative collapse. The expansion of detached area has been found in detachment experiments, such as TCV [79][80][81][82][10].

Some efforts have been dedicated to controlling the divertor detachment. In the ASDEX-Upgrade tokamak, diagnostics which are able to characterize the detached area in real-time, have been used for active control of divertor detachment. It was found that the detachment could be controlled through maintaining total plasma radiation at a fixed fraction of input power through injection of impurities like neon, argon and nitrogen [83][84]. Through experiments with alternative magnetic geometries in TCV, it was found that the angle of divertor plate tilt, poloidal flux expansion and major radius of the strike-point location greatly influence the detachment front location[28].Even so, it is still a big challenge to fully control the detachment process.

2.4.3 Divertor design and neutrals

As discussed above, increasing neutral pressures in the divertor is an effective way to achieve detached plasma operation. It can be achieved by either plasma fuelling or a high recycling regime (by increasing upstream density). But there is a correlation between the best plasma performance in tokamak devices and the low fuelling of the main plasma [85]. Although plasma fuelling (e.g.gas puff) results in a highly radiation and collision region and thus reduces the plasma temperature, it may also cause the confinement degradation [86][87].

To obtain a large value of the neutral compression ratio (ratio of neutral pressure near the targets to neutral pressure near the main plasma), the ITER incorporates a deep, well baffled divertor in order to retain neutrals created when the SOL plasma strikes the targets. As discussion in section 1.3,a closed divertor may be a good design for this purpose. It can produce higher main chamber neutral pressures than an open geometry. The first tokamak that applies geometrically closed divertors was ASDEX [88] and PDF [89]. Now it is used in modern tokamak devices (e.g. MAST and TCV). Apart from tokamak geometry, the design of the magnetic field configuration in the divertor chamber can influence the production of neutrals. Different field configurations have been used in divertor in order to increase the plasma-wetted area and reduce the heat flux, e.g.Super-X' and 'Snowflake' configurations [23][24]. More neutrals can be produced through surface recycling than the traditional divertor.

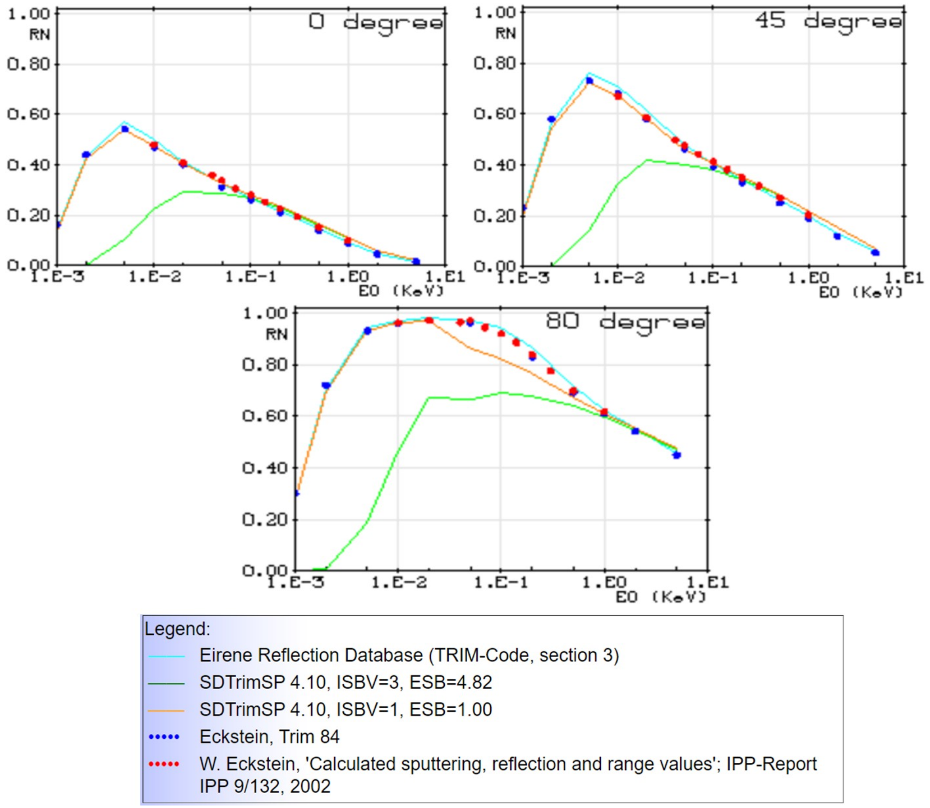

Figure 2.13: The particle reflection coefficient of hydrogen on the carbon-material surface. Diagrams from [90]

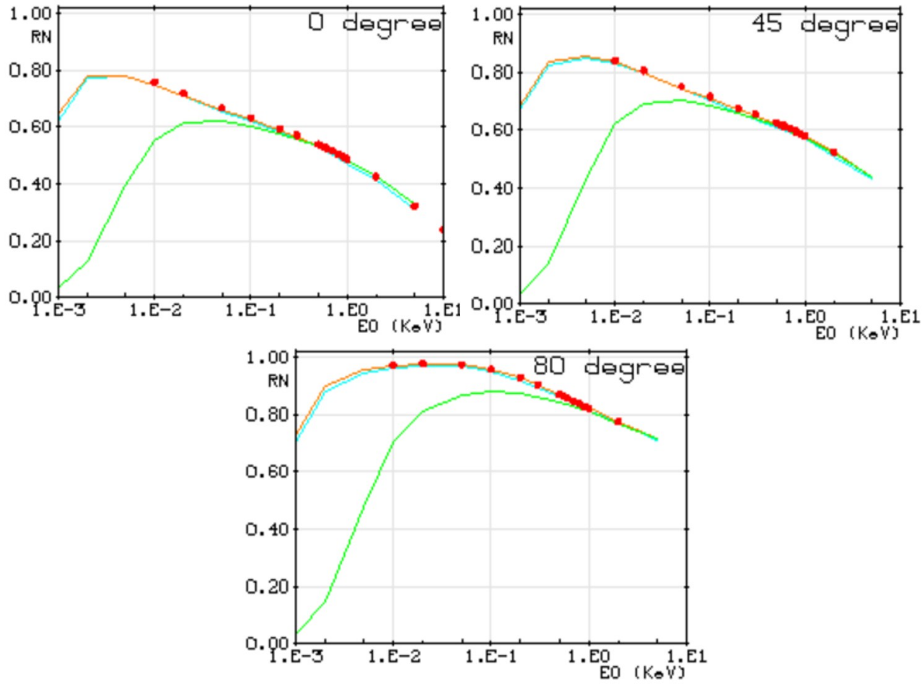

Figure 2.14: The particle reflection coefficient of hydrogen on the tungsten-material surface. Diagrams from [90]

As mentioned in section 1.3, tilting the target plates is an effective way to reduce heat flux, but it can also significantly affect the particle reflection coefficient of neutrals, which determines the recycling rate on the target. Figure 2.13 shows the particle reflection coefficient of hydrogen on carbon-material surfaces, which becomes smaller at lower incident polar angles [90]. But different plasma-facing materials will cause different reflection coefficients. According to figure 2.13 and figure 2.14, it is found that the particle reflection coefficient of hydrogen becomes larger on tungsten-material surfaces [90]. It means tungsten materials may produce more neutrals through recycling process. Additionally, the ratio of recycled atom flux and recycled molecule flux can be different on different materials [91]. These differences will affect the atomic and molecular processes in the divertor, which significantly influence the divertor performance.

To understand the effect of plasma recycling on different walls and target materials, it motivates me to investigate the role of atomic and molecular processes during divertor detachment with different recycling rate, which will be discussed in Chapter 4

Flux expansion

Since the heat flux and particle flux mainly flow along the magnetic field lines to the target, expanding the field lines can obtain a larger plasma-wetted area on target as shown in figure 2.15(a)[28]. It is called poloidal flux expansion obtained by decreasing the ratio of the poloidal field and the total field B_{poloidal}/B [92][93][94]. As the figure 2.15(b) shows, the flux expansion can also be obtained by expanding the distance from divertor entrance to the strike point on the target (toroidal flux expansion). It is found that the low-R_t configuration may lead to enhanced neutral trapping compared to the high-R_t configuration [95]. But there are some limits, including limited poloidal spreading due to the limited area of the divertor chamber. What is more, expanding the flux poloidally or toroidally needs a larger distance of the toroidal field coils from the centre of the plasma, due to the divertor chamber fully enclosed by the toroidal coils. Therefore, in order to achieve an acceptable heat load on the target, the divertor design may apply multiple of these configurations (e.g. designing a Super-X divertor with the flux expansion)[96]

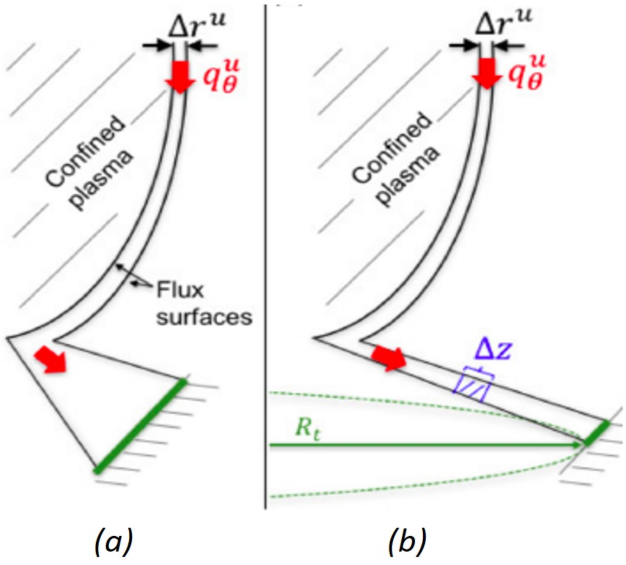

Figure 2.15: The divertor magnetic field configuration of (a) poloidal flux expansion and (b) toroidal flux expansion [28]

2.4.4 Experimental diagnosing and numerical modelling of divertor detachment

Divertor detachment involves a large collection of different processes having different effects on the plasma and target parameters, such as the ion target flux, target temperature and target heat flux. Therefore, various ways and methods could be used to define and characterise detachment [19][85][97]. A large range of diagnostics have been used to observe and measure the different aspects of detachment, in order to present and analyse the complete detachment process.

Experimental diagnostics

Meassuring with different probes is an efficient way for divertor diagnostics. For example, Langmuir probes [98] are usually used to measure the plasma density and electron temperature and plasma potential by inserting one or more electrodes (segmented Langmuir probe) into the plasma. The plasma ion flux reaching the target can be routinely obtained by measurements of Langmuir probes [99][19][100][101]. However, Langmuir probes can be inaccurate (e.g. overestimating plasma temperature and underestimating plasma density in detached divertor conditions). Especially in a detached divertor with dense and cold plasma, Langmuir probes cannot be used for the measurements in the divertor[35]. Reciprocating probe has been installed in the scrape-off layer of some tokamaks (e.g. TCV) [102][103] to measure the upstream plasma parameters, including plasma density, plasma temperature and heat flux at upstream. But typically only two plunges per discharge can be done, repeated discharges are needed in order to obtain more snapshots.

As discussed in section 2.3, the variation of upstream parameters (e.g. upstream density ramp) can lead to a change of heat flux, plasma ion flux and temperature at the target. It needs more reliable measurement ways for monitoring these parameters at upstream. Thomson scattering systems contain multiple lasers which can either be interleaved or fired simultaneously for either higher temporal resolution or higher signals [35]. They can be applied to monitor plasma density and temperature in core, upstream, SOL and divertors depending on line of sight. Recently, a new divertor Thomson scattering system has been developed for the MAST-U tokamak to measure electron density and temperature profiles along the Super-X strike leg [104]. The existing polychromator design has been adapted for low temperature measurements, thus it can provide more reliable measured results during detachment.

In terms of the detachment induced by impurities, diagnosing through imaging spectroscopy can be an effective approach to monitor impurity concentrations, electron densities, neutral populations and more [105][73][106][107][108][32]. Although these parameters are crucial for investigating detachment, detached divertors are most often investigated by measuring the hydrogen Balmer lines (section 2.2.4) in the spectrum [73][75][109].

Since different diagnostics are used to investigate the different aspects of detachment, it is important to obtain a coherent picture between the different diagnostics in order to account for the individual short-comings of each diagnostic. For instance, the high spatial resolution data of reciprocating probes can be combined with the lower spatial resolution Thomson data in order to combine the strengths of both diagnostics, in order to achieve high spatial and high temporal resolution. There is another case of this combination, a Multi-Wavelength Imaging (MWI) diagnostic has recently been designed and built on the MAST-U for studying the impact of machine's Super X divertor design [110], which can simultaneously capture 11 spectrally filtered images of the visible light emitted from divertor plasmas and can provide crucial knowledge for the interpretation of observations. For obtaining the inferred map of plasma parameter, it combines with localized measurements from Langmuir probes/Thomson scattering systems and 1D emission-weighted plasma profiles from spectroscopy, will provide crucial knowledge for the interpretation of observations.

Although various diagnostic systems have been used for divertor research, diagnosing the full effects of neutral processes is still a technical challenge for current diagnostic approaches. Molecular processes are often too complicated to diagnose, since molecules can undergo a large subset of different reactions [52][35].It requires more advanced diagnostic approaches with both a high resolution (sub-angstrom) and a large spectral coverage (40 nm)[35]. The effects of molecular processes are always ignored in experimental research, and thus it may lead to a large difference between the measurement and modelling results, especially in detached cases. To better understand the divertor physics and to study the role of molecular processes, it requires the efforts of numerical modelling with molecular physics and validations between measurements and modelling results.

Modelling

Although the actual detachment dynamics are complicated, the Two Point Model is often used for quick experimental comparisons. But the Two Point Model ignores cross-field transport and complex atomic and molecular physics. Even though the correction factors (section 2.3.2) could be considered, it is still insufficient to study these problems. To address this problem, 2D codes such as SOLPS, EDGE2D, SOLEDGE2D [111][112][49][113] have been developed for edge plasma simulations including divertor detachment. SOLPS-ITER, as one of the most often used suites for advanced divertor modelling, combines B2.5 (a fluid code in order to solve the Braginskii equations for ions and electrons together with EIRENE) [58][114]. EIRENE is a Monte Carlo neutral code which also includes several atomic, molecular and chemical physics databases (e.g. HYDHEL and AMJUEL presented in section 2.2.1). The data such as the rate coefficients of collisional and radiative reactions for divertor physics can be conveniently fetched and analysed by this code. The simulations of SOLPS code provide plasma and neutral parameters such as the electron density, temperature, neutral density and charge-resolved impurity densities. Target parameters (such as the ion target current) are also provided by the model. Such parameters can be compared to measured parameters in experiments [90].

Sophisticated 2D edge plasma transport codes are often too complex for easy interpretation of the physics involved. It is inefficient to use them for getting an idea of the different scalings in detachment. Some 1D computational models (e.g. [71][115][116][36][117] can provide more details of the underlying processes in the edge plasma, despite some simplifications and omissions, such as simplified geometry and treatment of cross field transport. Therefore making reasonable assumptions is crucial in 1D simulations.

A newly developed 1D divertor plasma code in BOUT++ framework, named SD1D, has been used to investigate the detachment dynamics [36][48]. The databases like ADAS and Amjuel are used to provide atomic and molecular data for SD1D simulations. With its good applicability, SD1D can be used for studying different types of divertor in different tokamaks and it can provide insight into the detachment physics (e.g. the role of momentum and power losses in divertor, atomic and molecular processes, the feedback control of detachment and more) [36][48]. As an efficient numerical tool for divertor research, SD1D can be used to provide guidance for the divertor experiments on different devices.

The physical model and important code upgrades in SD1D will be presented in next chapter.

2.5 Conclusions

Dviertor has been widely used in tokamak devices in order to extract the outflowing heat flux and ash produced by the fusion reaction. However, the heat load on plasma-facing material of the divertor target could be higher than the material limit and thus damage the target plates. It is the tokamak exhaust problem, which is a crucial problem for tokamak fusion research and even the construction of future magnetic confinement fusion devices. Divertor detachment is a potential solution to this problem, which can effectively reduce heat load on the target plates. Generally increasing the plasma density at upstream or seeding impurity in the divertor can achieve divertor detachment, but the process involves complex atomic and molecular physics, which significantly affect the particle, momentum and energy balance in the divertor volume. The role of atomic and molecular processes in the two detachment regimes may be different, and the divertor configuration and the target materials play a crucial role in the production of neutrals through recycling near the target, which may also influence atomic and molecular processes and thus affect the detachment process. The complex atomic and molecular processes make divertor detachment difficult to be controlled. Thus we need to implement experimental diagnostics and numerical modelling to investigate the effect of these process in the two detachment regimes.

Although various diagnostic systems have been used for divertor research, it is still a technical challenge to fully measure plasma-atom and plasma-molecule interactions. In this work, the atomic and molecular processes in MAST-U super-X divertor are modelled by a newly developed code 'SD1D' in order to investigate the role of molecular species in the particle, momentum and energy balance in divertor.

Chapter 3

Physical model of SD1D

Material in the section 3.4 of this chapter was published as part of the paper: *Investigation of the role of hydrogen molecules in 1D simulation of divertor detachment,* Yulin Zhou et al 2022 Plasma Phys. Control. Fusion 64 065006 [48]

The new 1D divertor plasma code, SD1D, is a plasma simulation model built on BOUT++, developed mainly for numerically studying divertor physics, especially the mechanism of divertor detachment. In this chapter we present the numerical implementation, starting with an introduction of the BOUT++ framework in Sec. 3.1. Then the basic physical model of the SD1D module is presented in Sec. 3.2, and the Atomic++ module which is used to calculate the impurity radiation power is introduced in section 3.3. In order to study the role of molecular processes, a molecular model is added in the SD1D module, which will be detailed in Sec. 3.4. Finally in Sec. 3.5, the impurity (neon) transport is added in SD1D module to investigate the difference between density ramp detachment and impurity seeding detachment.

3.1 Introduction of BOUT++ framework

BOUT++ (Boundary Turbulence in C++), which was developed from the older BOUT code [118], is a software framework for solving arbitrary numbers of non-linear partial differential equations in curvilinear coordinates in parallel[119]. Since BOUT++ was developed, it has been upgraded with different solvers options and pre-conditioners[120] and verified with the method of manufactured solutions [121].

BOUT++ is a fully open-source code with a variety of numerical methods and time-integration solvers, which can be used to solve quite general sets of time-dependent equations on grids with various geometries, different plasma configurations, different coordinate system and different topologies. The geometry is specified by providing the coordinate spacing between grid points $dx_{i,j}$, $dy_{i,j}$, and $dz_{i,j}$ in three directions. The distance between grid points is $\sqrt{g_{i,j}dx^i dx^j}$. $g_{i,j}$ is the components of the metric tensor. BOUT++ is intended to be quite modular, enabling fast testing of numerical methods. It provides an efficient platform for users to design their fluid and plasma simulation codes. For instance, writing simulation code for tokamak plasma research is a complicated process which needs to solve problems, including communication between multiple processors, spatial differentiation, time integration, curved geometry and more. However BOUT++ has helped users to complete all these works, which have be written as operators and functions, thus largely simplifying the code development within its framework.

Now various modules have been built in BOUT++, such as SD1D, STORM, ELMpb and more [122] [36] [123], aiming to numerically study the physics of edge plasma region in the geometry of different devices, such as MAST-U, JET, TCV, DIII-D and the future devices (e.g. ITER, DEMO). Here is a brief introduction for BOUT++ code. An in-depth description of the code can be found in BOUT++ documentation[124].

3.2 The original SD1D module

3.2.1 Equations for plasma and neutral atoms

A 1D time dependent fluid model[19][117] is used in SD1D module, which evolves the plasma density n, parallel momentum density $m_{H^+}nv_{\|}$ and static pressure $p = 2enT$. The plasma equations are shown below [36]:

$$\frac{\partial n}{\partial t} = -\nabla \cdot [\mathbf{b}v_{\|}n] + S_n - S \tag{3.1}$$

$$\frac{\partial}{\partial t}(\frac{3}{2})P = -\nabla \cdot \mathbf{q}_e + v_{\|}\partial_{\|}p + S_E - E - R \tag{3.2}$$

$$\frac{\partial}{\partial t}(m_{H^+} n v_\parallel) = -\nabla \cdot [m_{H^+} n v_\parallel \mathbf{b} v_\parallel] - \partial_\parallel p - F \tag{3.3}$$

Where $\partial_\parallel = \mathbf{b} \cdot \nabla$, the heat flux is $\mathbf{q_e} = \frac{5}{2} p \mathbf{b} v_\parallel - \kappa_\parallel \boldsymbol{\partial}_\parallel T_e$ and the Braginskii thermal conduction coefficient is $\kappa = \kappa_0 T^{\frac{5}{2}}$. The constant $\kappa_0 = 2293.8[\mathrm{MW/m^2/eV^{\frac{5}{2}}}]$ and m_{H^+} is the mass of the main ions. $v_\parallel$ is the parallel velocity of the main ions. The ion and electron temperatures are assumed to be equal and isotropic: $T = T_e = T_{\mathrm{H}^+}$, while their densities are equal as well: $n_e = n_{\mathrm{H}^+}$.

In equation 3.1, S_n is the external particle source evolved by a proportional-integral (PI) feedback controller, therefore a specified upstream plasma density can be achieve. S shows the particle sources and sinks caused by collisional reactions like ionisation and recombination. In equation 3.2, S_E represents an external source of power that keeps injecting energy with a fixed rate into a volume above X-point, as the red arrows are shown in figure 3.1. E represents energy exchange due to plasma-neutral interactions; R is radiation power generated by hydrogen atom radiation and impurity radiation. The particle sources and sinks (S), friction force (F), and energy sources and sinks (E and R) caused by collisional reactions can be found in the Appendix A.

The equations of atom density n_{H}, atom parallel momentum $n_{\mathrm{H}} v_{\parallel \mathrm{H}}$ and atom static pressure $n_{\mathrm{H}} T_{\mathrm{H}}$ are similar to equation 3.1, equation 3.2 and equation3.3. But the reaction rate in the source, sink and force terms of atomic equations is calculated differently. Recycling is considered in SD1D model, which converts the plasma ion flux arriving the target to neutral atom flux at a fixed rate (section 3.2.2).

To implement simulations for studying divertor detachment (e.g. density ramp detachment), S_E, S_n and upstream plasma ion density are the crucial controllable quantities to achieve detachment in simulations.

Flux tube expansion As discussed in 2.4.3, flux expansion can be crucial for the reduction of heat load at the target. In SD1D module, the effects of gradients in the total magnetic field (the total flux expansion) have been included. The flux

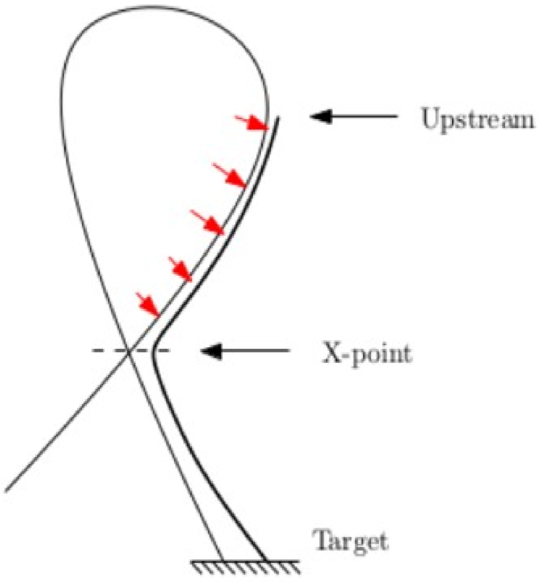

Figure 3.1: The geometry for SD1D simulations [125]

expansion is presented using the different flux tube area at different grid points from the X-point to the target as shown in figure(3.2). The flux tube area at different grid points S is written as equation (3.4).

$$S = S_{\text{Xpoint}}(1 + (f_{\text{expansion}} - 1) \times \frac{y - y_{\text{Xpoint}}}{2\pi - \theta_{y_{\text{Xpoint}}}}) \tag{3.4}$$

S_{Xpoint} is the flux tube area at X-point. y is along the parallel direction and y_{Xpoint} reprents the position at X-point. $f_{\text{expansion}}$ is the area expansion factor, the ratio of the total field at the X-point to that at the target ($B_{\text{X-point}}/B_{\text{target}}$). $\theta_{y_x} = \pi \times (2 - d_{\min} - \frac{\sqrt{(2-d_{\min})^2 - 4\times(1-d_{\min}\times\frac{L_x}{L}))}}{1-d_{\min}}$. The parameter L_x is the length from upstream(or midplane) to X-point, L is the total connection length (from upstream to the target) $d_{min} = 0.1$. All the evolving quantities are constant on a flux-tube cross-section, as shown in figure 3.2.

Since the magnetic field cannot confine the transport of neutral particles, the atoms will be transported across the magnetic field and they will also migrate upstream. 1D codes usually ignore the effects of cross-field transport, which may be crucial for the diveror detachment. To model this process, SD1D provides an effective parallel velocity to atoms which is the sum of a parallel flow and parallel projection of a perpendicular diffusion [36]: v_H=$v_{\parallel,H} - (\frac{B_\phi}{B_\theta})^2\frac{\partial_\parallel p_H}{v}$. The total atom collision frequency is calculated by the sum of charge exchange rate, ionisation rate and neutral-neutral collision rate. Since the poloidal flux expansion can affect cross-field neutral diffusion, the cross-field neutral diffusion multiplier (field-line pitch) $(\frac{B_\phi}{B_\theta})^2$ is used in this equation.

Although a similar cross-field diffusion could be added in the plasma equations, an unknown diffusion coefficient would be produced in simulations. So the parallel projection of the cross-field diffusion is not considered in the following works.

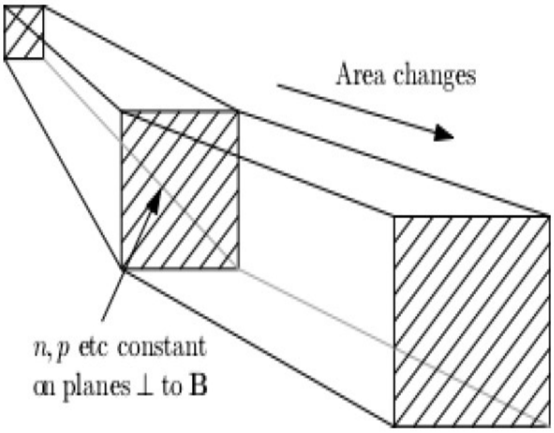

Figure 3.2: Flux tube expansion

3.2.2 Boundary condtions

Sonic (Bohm) boundary conditions are set at the target, where the parallel plasma velocity $v_{\|} \geq c_s$. The plasma sound speed is $c_s = \sqrt{\frac{2\times T}{m_{\mathrm{H}+}}}$. The plasma parallel velocity should be greater than or equal to the sound speed. Boundary conditions are imposed on the boundary between cells. If the velocity of plasma flow in the last cell is supersonic then a Neumann boundary condition will be set for the velocity [36].

The plasma density and pressure boundaries are 'free', so that they are extrapolated into the boundary. If an additional boundary is imposed on plasma density and pressure, the system of equation will be over-constrained. The temperature gradient at the sheath entrance is set to zero, replacing the heat conduction with the energy flux corresponding to a sheath heat transmission of $q = \gamma n T c_s$ [36]. The sheath transmission coefficient γ is equal to 6 in this work.

For recycling processes at the target in this work, the recycling fraction of ion flux to the target is set to $f_{\mathrm{recl}} = \frac{\Gamma_{\mathrm{recl}}}{\Gamma^t_{\mathrm{ion}}} = 0.99$, such that 99% of the plasma ion flux to the target Γ^t_{ion} is recycled and converted to the neutral flux Γ_{recl} (made up of neutral atoms) in the final grid point at the target. The temperature of recycled neutral atoms are given based on the Franck-Condon energy (e.g. 3.5eV for hydrogen atom)[36]. The neutral velocity is equal to zero at the target and the neutral temperature boundary and density boundary are free.

Only atomic processes were considered in the original SD1D module, while volumetric processes involving molecular species were not directly calculated, being only included indirectly in the effective radiation rate. Since molecules play a crucial role in divertor plasma dynamics, it is necessary to create a molecular model in SD1D (section 3.4). Additionally the hydrogen reaction rate (except recombination) and excitation radiation power in the original SD1D are obtained by semi-analytic approximations [126][127]. The reaction rate coefficients of atom-plasma interactions and hydrogen emissivity from those approximations are only a function of T_e and have no n_e dependence. As discussed in section 2.2.2 and section 2.2.3, a large error may be produced if n_e changes.

3.3 Impurity radiation: Atomic++ module

The radiation of either intrinsic impurities (e.g. carbon) or extrinsic impurities (e.g. neon, nitrogen) plays a crucial role in the boundary plasma power dissipation. To include the impurity radiation, the SD1D is coupled with the Atomic++ module in BOUT++ framework. Generally, Atomic++ is developed to fetch and analyse data from the ADAS database. Through evaluating a set of balance equations based on ADAS rate coefficient data, the model is able to determine the population and momentum dynamics of impurity at each charge state. The absorbed and radiated power can also be calculated by the model. It can be coupled with other BOUT++ modules and provide its calculations for simulations [59]. The following part will present Atomic++ module in detail.

Data from the ADAS database

The ADAS data files are supplied with accompanying Fortran-77 reader functions

[43]. Since the BOUT++ framework is a C++ based code, the use of Fortran is disallowed in the BOUT++ project. To address this problem, the data functions of ADAS rate coefficients and emissivities (such as effective ionisation, effective recombination, charge exchange, line emission and continuum emission) are wrapped in Python3 by using functions adapted from the atomic project in [128]. Then the functions are exported to JSON-formatted text. A separate Github project to automate the ADAS fetch, SI-unit conversion and JSON-save routine is provided at [59][43].

Particle, momentum and energy balance equations

The rate coefficients and emissivity obtained from ADAS can be used to construct a set of balance equations for the density, momentum and energy of each charge state of the specified impurity. Firstly, balancing the sinks and sources of the particle at a certain charge state 'Z' can achieve a particle balance equation for the particle '*part*', as shown in [59]:

$$\frac{\partial n^{Z}_{\text{part}}}{\partial t} = \left[K^{Z-1\rightarrow Z}_{\text{i,part}} n^{Z-1}_{\text{part}} - \left(\left(K^{Z\rightarrow Z+1}_{\text{i,part}} + K^{Z\rightarrow Z-1}_{\text{rec}}\right) n^{Z}_{\text{part}}\right) + K^{Z+1\rightarrow Z}_{\text{rec}} n^{Z+1}_{\text{part}}\right] \times n_e$$

$$+ \left[K^{Z+1\rightarrow Z}_{\text{cx}} n^{Z+1}_{\text{part}} - K^{Z\rightarrow Z-1}_{\text{cx}} n^{Z}_{\text{part}}\right] n_n \tag{3.5}$$

Here K is rate coefficient $< \sigma v >$ of a certain reaction type, including ionisation 'i', recombination 'rec' and charge exchange 'cx'. n_e and n_n are electron density and density of neutrals. Ionisation from the state below(Z'=Z-1) is the source of the state above and recombination (including charge exchange with neutrals) from the state above (Z'=Z+1) is the source of the state below. The sinks are the inverse situations. One thing needs to be noted here: The ground state and the highest state only have one reaction direction.

Similarly, the forces imposed on the particle of each charge state can be achieved by the reaction rate coefficients. The momentum balance equation is [59]:

$$\frac{\partial\left[p^Z_{\text{part}}\right]}{\partial t} = \left[K^{Z-1\to Z}_{\text{i,part}} p^{Z-1}_{\text{part}} - \left(\left(K^{Z\to Z+1}_{\text{i,part}} + K^{Z\to Z-1}_{\text{rec}}\right) p^Z_{\text{part}}\right) + K^{Z+1\to Z}_{\text{rec}} p^{Z+1}_{\text{part}}\right] \times n_e$$

$$+ \left[K^{Z+1\to Z}_{\text{cx}} p^{Z+1}_{\text{part}} - K^{Z\to Z-1}_{\text{cx}} p^Z_{\text{part}}\right] n_n \tag{3.6}$$

The momentum density of a certain particle species is $p^Z_{\text{part}} = m_{\text{part}} n^Z_{\text{part}} v^Z_{\text{part}} [\text{Nm}^{-3}\text{s}]$. The energy balance equation gives the rate at which energy is absorbed through ionisation, dissipated through recombination or radiation. Therefore it represents the cooling rate of a particle species. The equation can be written as below[59]:

$$P_{\text{cool}} = P_{\text{rad}} + \sum_{Z=0}^{Z_{\text{max}}-1} \left\langle \phi^Z_{\text{i,part}} \right\rangle \left[R^{Z\to Z+1}_{\text{i,part}} - R^{Z+1\to Z}_{\text{rec}}\right] - \left(\left\langle \phi^Z_{\text{i,part}} \right\rangle - \phi_n\right) R^{Z+1\to Z}_{\text{cx}} \quad [\text{Wm}^{-3}] \tag{3.7}$$

In equation 3.7, the raidation power of the particle species 'part' is [59]

$$P_{\text{rad}} = \sum_{Z=0}^{Z_{\text{max}}} n^Z_{\text{part}} \left[\left(L^Z_{\text{line}} + L^Z_{\text{cont.}}\right) n_e + L_{\text{cx}} n_n\right] \quad [\text{Wm}^{-3}] \tag{3.8}$$

The ionisation and recombination rate are $R^{Z\to Z+1}_{\text{i,part}} = K^{Z\to Z+1}_{\text{i,part}} n^Z_{\text{part}} n_e$ and $R^{Z+1\to Z}_{\text{rec,part}} = K^{Z+1\to Z}_{\text{rec,part}} n^{Z+1}_{\text{part}} n_e$. The rate of charge exchange with neutrals is $R^{Z+1\to Z}_{\text{cx,part}} = K^{Z+1\to Z}_{\text{cx,part}} n^{Z+1}_{\text{part}} n_n$. Ionisation potential for the state 'Z' is $\phi^Z_{\text{i,part}}$ and for the neutrals ϕ_n [59]

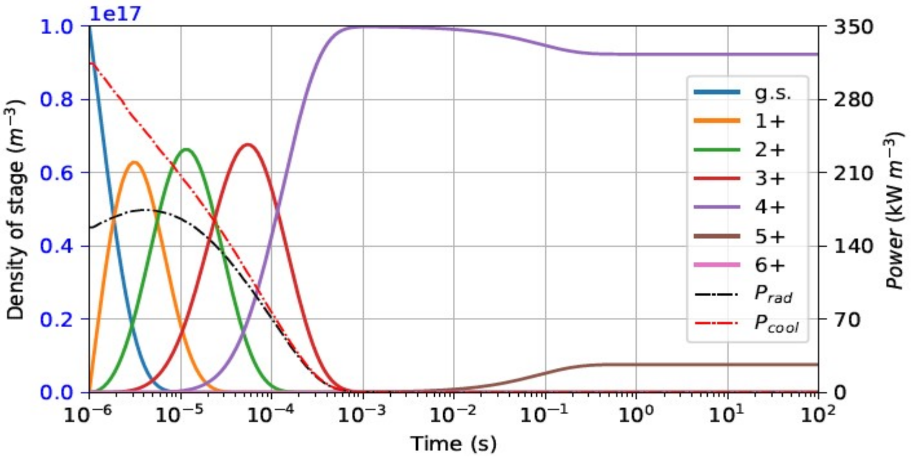

Figure 3.3: Density of charge states and radiation power as a function of time for the case with 1% carbon impurity, $T_e = 50\text{eV}$ and $n_e = 1 \times 10^{19}\text{m}^{-3}$. Diagram from [59]

Based on the equation, the density and cooling rate of an impurity at different charge states and the force imposed on them can be simulated if T_e, n_e and the initial density of the impurity are given. As figure 3.3 shows, the density, radiation power and cooling rate of carbon at different states eventually reach a thermal equilibrium after a time evolution of the system. So if Atomic++ receive T_e, n_e and the total impurity density (including all charge states) from other codes, inversely Atomic++ can provide its calculations back to their simulations.

3.4 Code upgrade: the molecular model in SD1D

In the original version of SD1D (section 3.2.1), only atomic processes were included, while molecular processes were not. To investigate the role of atomic and molecular processes in divertor detachment physics, an important upgrade was carried out in SD1D module by adding a molecule model, including an explicitly evolved hydrogen molecule model labelled '$\mathrm{H_2}$' and a charged molecule model labelled '$\mathrm{H_2^+}$'.

3.4.1 Equations for $\mathrm{H_2}$ and $\mathrm{H_2^+}$

The molecule model is established in a similar way to the atom model. The equations of molecule including density $n_{\mathrm{H_2}}$, pressure $p_{\mathrm{H_2}}$ and parallel momentum $n_{\mathrm{H_2}}v_{\|\mathrm{H_2}}$ are written in the form of equations 3.1,3.2 and 3.3 [48]:

$$\frac{\partial n_{\mathrm{H_2}}}{\partial t} = -\nabla\cdot\left[\mathbf{b}v_{\|,\mathrm{H_2}}n_{\mathrm{H_2}}\right] - S_{\mathrm{H_2}} \tag{3.9}$$

$$\frac{\partial}{\partial t}\left(\frac{3}{2}p_{\mathrm{H_2}}\right) = -\nabla\cdot\mathbf{q}_{\mathrm{H_2}} + v_{\|,\mathrm{H_2}}\partial_{\|}p_{\mathrm{H_2}} - E_{\mathrm{H_2}} \tag{3.10}$$

$$\frac{\partial}{\partial t}\left(m_{\mathrm{H_2}}n_{\mathrm{H_2}}v_{\|,\mathrm{H_2}}\right) = -\nabla\cdot\left[m_{\mathrm{H_2}}n_{\mathrm{H_2}}\mathbf{b}v_{\|,\mathrm{H_2}}\right] + \partial_{\|}p_{\mathrm{H_2}} - F_{\mathrm{H_2}} \tag{3.11}$$

$$\mathbf{q}_{\mathrm{H_2}} = \frac{5}{2}p_{\mathrm{H_2}}\mathbf{b}v_{\|,\mathrm{H_2}} \tag{3.12}$$

The terms of the sources, sinks ($S_{\mathrm{H_2}}$ and $E_{\mathrm{H_2}}$) and friction force $F_{\mathrm{H_2}}$ are generated by the recycling and collisional reactions listed in table 3.1, including non-dissociative

1. $\mathrm{e} + \mathrm{H} \rightarrow 2\mathrm{e} + \mathrm{H}^+$	Ionisation
2. $\mathrm{H}^+ + \mathrm{H} \rightarrow \mathrm{H} + \mathrm{H}^+$	Charge exchange
3. $\mathrm{H}^+ + \mathrm{e} \rightarrow \mathrm{H}$	Electron-ion Recombination
4. $\mathrm{e} + \mathrm{H}_2 \rightarrow 2\mathrm{e} + \mathrm{H}_2^+$	Non-dissociative Ionization
5. $\mathrm{e} + \mathrm{H}_2 \rightarrow \mathrm{e} + \mathrm{H} + \mathrm{H}$	Dissociation
6. $\mathrm{H}^+ + \mathrm{H}_2 \rightarrow \mathrm{H}_2^+ + \mathrm{H}$	Molecular charge exchange
7. $\mathrm{e} + \mathrm{H}_2^+ \rightarrow \mathrm{e} + \mathrm{H}^+ + \mathrm{H}$	Dissociative excitation
8. $\mathrm{e} + \mathrm{H}_2^+ \rightarrow 2\mathrm{e} + \mathrm{H}^+ + \mathrm{H}^+$	Dissociative ionization
9. $\mathrm{e} + \mathrm{H}_2^+ \rightarrow \mathrm{H} + \mathrm{H}$	Dissociative recombination
10. $\mathrm{H}^+ + \mathrm{H}_2 + \mathrm{e} \rightarrow \mathrm{H} + \mathrm{H} + \mathrm{H}$	MAR via H^-

Table 3.1: List of collisional reactions (1-3) in the atom model and the reactions (4-10) in the molecule model

ionisation, dissociation, molecular charge exchange and molecular activated recombination (MAR) via H^- (see Appendix A). In equation 3.12 $\mathbf{q}_{\mathrm{H}_2}$ is the energy convection flux of neutral molecules. Following the effective parallel velocity of atoms, a parallel velocity v_{H_2} with the cross-field neutral diffusion $\left(\frac{B_\phi}{B_\theta}\right)^2 = 10$. The total molecule collision frequency is calculated by the sum of molecular charge exchange rate, non-dissociative ionisation rate and neutral-neutral collision rate [36][48].

The equations of the charged molecule H_2^+ are consistently with the equations of atomic species and the equations of neutral species. A similar set of three equations for H_2^+ is also added in SD1D: the sources, sinks ($S_{\mathrm{H}_2^+}$ and $E_{\mathrm{H}_2^+}$) and friction force ($F_{\mathrm{H}_2^+}$) in the equations of density $n_{\mathrm{H}_2^+}$, pressure $p_{\mathrm{H}_2^+}$ and momentum $n_{\mathrm{H}_2^+}\ v_{\mathrm{H}_2^+}$ are determined by dissociative excitation, molecular ionisation, dissociative ionisation, dissociative recombination and molecular charge exchange shown in Table 3.1 (reaction 4, 6, 7, 8 and 9) [48].

3.4.2 Boundary conditions and important assumptions for H_2 and H_2^+

The boundary conditions for H_2 are listed below:

(1) The recycling fraction of ion flux to the target is set to $f_{\mathrm{H}_2,\ \mathrm{recl}} = \frac{\Gamma_{\mathrm{H}_2,\mathrm{recl}}}{\Gamma^t_{\mathrm{ion}}}$ where $\Gamma_{\mathrm{H}_2,\mathrm{recl}}$ is the flux of H_2 produced by recycling in the final grid point at the target. The temperature of recycled neutral molecules is given based on the temperature of the facing material (Set 0.1eV in this work), but the velocity of recycled H_2 is equal

to zero.

(2) The temperature boundary and density boundary of H_2 are free.

Two neutral species (atoms and molecules) are now contained in this version of SD1D. According to experimental observations in divertors, both atoms and molecules are important plasma recycling channels, their relative ratio depending on the target material (e.g. carbon and tungsten) [91][129]. In Chapter 4, a comparison is made to study divertor detachment with different proportions of recycled atoms and molecules.

The boundary conditions for H_2^+ are:

(1) Bohm boundary conditions are used for H_2^+ at the target. So the parallel plasma velocity at the target is $v_{\|,H_2^+} \geq c_{s,H_2^+}$, where $c_{s,H_2^+} = \sqrt{\frac{2\times T_{H_2^+}}{m_{H_2^+}}}$.

(2) The density and pressure boundaries of H_2^+ are 'free'.

(3) The temperature gradient of H_2^+ at the sheath entrance is zero.

(3) The energy flux is related to a sheath heat transmission of $q_{H_2^+} = \gamma n_{H_2^+} T_{H_2^+} c_{s,H_2^+}$ where $\gamma = 6$.

Important assumptions

To compare the simulations of the upgraded SD1D to the previous work, the assumptions made in the original version are still used in the upgraded SD1D, including equal isotropic ion and electron temperatures $T_{H^+} = T_e$ and quasineutrality $n_{H^+} = n_e$

Since H_2^+ is a changed particle species together with H^+, introducing H_2^+ in simulation may change the quasineutrality assumption, which should be $n_{H^+} + n_{H_2^+} = n_e$. But the H_2^+ density $n_{H_2^+}$ is small ($\frac{n_{H_2^+}}{n_{H_2^+} + n_{H^+}} < 0.022$ when $T_e < 7$eV) and is only distributed in a very narrow area in front of the target (discussed in section 4.3). Therefore, a **trace assumption** is used for H_2^+, which means $n_{H_2^+}$ does not affect the quasineutrality assumption $n_{H^+} = n_e$. Since the upgraded SD1D aims to study the divertor detachment (related to low target temperatures), it is expected that the trace assumption will not affect the main physics of divertor detachment (e.g. the rollover of target flux, momentum loss and photon emission).

However during attachment T_e in the recycling region is high (e.g. $T_e > 15\text{eV}$), such that $\frac{n_{H_2^+}}{n_{H_2}}$ can be over 7% and $\frac{n_{H_2^+}}{n_{H_2^+} + n_{H+}}$ will no longer be negligible in front of the target. So if future studies focus on the cases with high target temperatures, the trace assumption on H_2^+ may not be suitable. In this case, it requires changes to the electron equations.

3.4.3 Hydrogen reaction rate coefficients and hydrogen emissivity

As mentioned in section 3.2.1, the reaction rate coefficients used in the original SD1D only depend on the electron temperature T_e (electron-ion recombination rates included density variation), but it was not very precise since rate coefficients have a n_e dependence as well.

As discussed in section 2.2, the n_e dependence of the plasma-neutral interactions is crucial, because the electron density in the divertor can greatly change in different operating conditions and is sensitive to the variation of the upstream density, heat and particle flux. Once divertor detachment is achieved by increasing upstream density, the peak electron density in the divertor will be several times larger than during attachment, while the divertor electron density can decrease when the divertor is fully detached. As a result, it is crucial to consider electron density variation in the calculation of rate coefficients and hydrogenic radiation.

In order to solve this problem, the 'Amjuel' database is now been used in SD1D module. Amjuel uses a double polynomial fitting expression as a function of electron temperature and density to calculate the rate coefficients of electron-atom, electron-ion and electron-molecule interactions (i.e. ionisation, dissociation, recombination and the reactions related to molecules as shown in table 3.1) . For the ion-atom, ion-molecule interactions (i.e. charge exchange), its double polynomial expression is a function of energies of the two collided particles [44].

Hydrogen excitation radiation

Apart from collisional reactions, the hydrogen atom radiation caused by atom-plasma or molecule-plasma interactions is also crucial for divertor physics [38]. It contributes a significant energy loss from the plasma in the divertor, and it greatly influence the target flux in terms of particle and power balance.

Although the original SD1D considered hydrogen electron-impact excitation radiation and electron-ion recombination, the hydrogen emissivity was an empirical function of T_e, which leads to a large error if the electron density is varied. Same as the rate coefficient discussed above, hydrogen emissivity should also have a dependence of both T_e and n_e. Additionally just obtaining the total hydrogen excitation radiation power cannot know enough details to fully understand the mechanism of hydrogen excitation radiation and the effect of atomic and molecular radiative reactions, which may play a critical role in a detached case. According to figure 2.5 in section 2.2.3, there are 6 excitation channels to produce excited hydrogen atoms including:

(1) Direct electron-impact excitation (via H)

(2) Electron-ion recombination (via H^+)

(3) Dissociation (via H_2),

(4) Dissociative recombination (via H_2^+)

(5) Dissociative recombination (via H_3^+) (ignored in SD1D pysical model)

(6) Mutual neutralization (via H^-)

The channel (1) direct electron-impact excitation and channel (2) electron-ion recombination are known as the *atomic excitation channel*, while the channels (3)-(6) are the *molecular channels* since hydrogen atoms are excited after molecular break-up. In order to calculate radiation power though the different channels, it requires the population coefficient of excited atoms produced through different channels.

Amjuel databases can be used to solve this problem. The hydrogen radiation power as a function of T_e and n_e can be modelled by the population coefficients obtained from Amjuel. The radiation power produced by every channel is obtained by the following steps:

I_{pq} is the emission intensity from state ‘p’ to ‘q’ and is defined as

$$I_{pq} = n_e N_0 \chi_{pq}^{eff} \tag{3.13}$$

$$\chi_{pq}^{eff} = R_{0p} A_{pq} \tag{3.14}$$

$$R_{0p} = \frac{N_p}{n_e N_0} \tag{3.15}$$

where χ_{pq}^{eff} is the effective emission rate coefficient and R_{0p} Einstein coefficient or rate of transmitting from state ‘p’ to ‘q’ [130]; N_0 is the density of the reacting species which collides with electrons to generate atoms in the excited state ‘p’ (e.g for direct electron-impact excitation N_0 represents the density of hydrogen atom). Depending on equation 3.13, 3.14 and 3.15, we can get the emission intensity of the excited atom from state ‘p’ to ‘q’ in equation 3.16 [46][48].

$$I_{pq} = n_e N_0 \chi_{pq}^{eff} = n_e N_0 \times \frac{N_p}{n_e N_0} \times A_{pq} = N_p A_{pq} \tag{3.16}$$

Then multiplying the emission intensity I_{pq} by the energy gap between any two states E_{pq} [130], the radiation power density W/m^3 produced by the excited atoms in a certain state ‘p’ is obtained by equation 3.17.

$$\varepsilon_{\mathrm{rad},pq} = E_{pq} \times I_{pq} \tag{3.17}$$

Through summing the radiation power density over energy level transitions (only Lyman series of p= 2-6 → 1 is considered), the radiation power density of an excitation channel can be written as [131]

$$\varepsilon_{\mathrm{rad},p\to 1}^{\mathrm{channel}} = \sum_{p=2}^{6} E_{p\to 1} N_p A_{p\to 1} \tag{3.18}$$

Repeat the calculation for all the 6 excitation channels, and we can get the total hydrogen atom radiation power per volume (e.g in the unit W/m^3) by summing the radiation power density of all channels [48]. The hydrogen emissivity through different channels is shown in section 2.2.3

Since the upgraded SD1D ignores the dynamics of H_3^+ due to its negligible density and limited contribution to the energy loss in experiment [38][132], the excitation channel via H_3^+ is also ignored. Therefore in the upgraded SD1D, 5 excitation channels have been considered in the physical model including H, H_2, H^+,H_2^+ and H^-.

One thing need to be noted: the calculation of the hydrogen photon emission coefficient is similar to hydrogen emissivity. For example, the intensity of H_{alpha} photon emission (Balmer lines 3 →2) through the different excitation channels is

$$I^{channel}_{\mathrm{photon},3\to 2} = N_3 A_{3\to 2} \tag{3.19}$$

3.4.4 Conclusion

After the code upgrade in this section, there are some highlighted changes compared to the original version:

(1) SD1D includes five particle species: H, H_2, H^+, H_2^+ and H^-. But H^- is only considered in the hydrogen radiation model.

(2) The empirical functions used in the hydrogen collision and radiation model have been replaced by Amjuel database, which provides reaction rate coefficients and hydrogen population coefficients (has the dependence of both T_e and n_e) to the upgraded SD1D.

(3) The radiation model includes 5 hydrogen excitation channels: Direct electron-impact excitation (via H) and electron-ion recombination (via H^+) are atomic excitation channels. Dissociation (via H_2), dissociative recombination (via H_2^+) and mutual neutralization (via H^-) are molecular excitation channels.

The upgraded SD1D module is able to numerically simulate the molecular processes and to investigate the role of atomic and molecular processes during the detachment achieved by a density ramp (see Chapter 4).

3.5 Code upgrade: the impurity model in SD1D

Seeding impurity (primarily neon in this work) is another effective way to achieve divertor detachment. To investigate the atomic and molecular processes during impurity seeding in divertor, another upgrade has been made by adding impurity dynamics and impurity radiation into the physical model with molecules (section 3.4)

3.5.1 Equations for Neon

The dynamics of neon impurity at all charge states (from the ground state to the charge state 10+) has been considered, thus all of them have their own density equation, momentum equation and pressure equation in the upgraded SD1D.

First the neutral neon Ne^{0+} model is established in a similar way to the neutral hydrogen atom and molecule models. As shown below, the equations of neutral neon include density $n_{\mathrm{Ne}^{0+}}$ (equation 3.20), pressure $p_{\mathrm{Ne}^{0+}}$ (equation 3.21) and parallel momentum $n_{\mathrm{Ne}^{0+}} v_{||\mathrm{Ne}^{0+}}$ (equation 3.22)

$$\frac{\partial n_{\mathrm{Ne}^{0+}}}{\partial t} = -\nabla \cdot \left[\mathbf{b} v_{||,\mathrm{Ne}^{0+}} n_{\mathrm{Ne}^{0+}}\right] - S_{\mathrm{Ne}^{0+}} \tag{3.20}$$

$$\frac{\partial}{\partial t}\left(\frac{3}{2} p_{\mathrm{Ne}^{0+}}\right) = -\nabla \cdot \mathbf{q}_{\mathrm{Ne}^{0+}} + v_{||,\mathrm{Ne}^{0+}} \partial_{||} p_{\mathrm{Ne}^{0+}} - E_{\mathrm{Ne}^{0+}} \tag{3.21}$$

$$\frac{\partial}{\partial t}\left(m_{\mathrm{Ne}^{0+}} n_{\mathrm{Ne}^{0+}} v_{||,\mathrm{Ne}^{0+}}\right) = -\nabla \cdot \left[m_{\mathrm{Ne}^{0+}} n_{\mathrm{Ne}^{0+}} \mathbf{b} v_{||,\mathrm{Ne}^{0+}}\right] + \partial_{||} p_{\mathrm{Ne}^{0+}} - F_{\mathrm{Ne}^{0+}} \tag{3.22}$$

$$\mathbf{q}_{\mathrm{Ne}^{0+}} = \frac{5}{2} p_{\mathrm{Ne}^{0+}} \mathbf{b} v_{||,\mathrm{Ne}^{0+}} \tag{3.23}$$

The terms of the sources/sinks $S_{\mathrm{Ne}^{0+}}$ in density equation are produced by the impurity seeding, recycling and collisional reactions. The sources/sinks $E_{\mathrm{Ne}^{0+}}$ in pressure equation are mainly caused by collisional reactions and radiation. In this work, Atomic++ (section 3.3) is used to model the radiation power caused by neon impurity.The force term $F_{\mathrm{Ne}^{0+}}$ in the momentum equation is imposed by friction forces, thermal force, collisional reaction and the force due to a parallel electric field. $\mathbf{q}_{\mathrm{Ne}^{0+}}$ is the energy convection; $v_{\|,\mathrm{Ne}(0+)}$is the effective parallel velocity. However the parallel projection $v_{\|,\mathrm{Ne}^{0+}}$of a perpendicular diffusion is not considered in the current neutral neon model, since an unexpected infinity error will be generated in simulation. Thus in the future work, we will find a reasonable way to simulate cross-field transport.

In terms of the neon ions Ne^{Z+}, the equations can be written as below:

$$\frac{\partial n_{\mathrm{Ne}^{Z+}}}{\partial t} = -\nabla \cdot \left[\mathbf{b} v_{\|,\mathrm{Ne}^{Z+}} n_{\mathrm{Ne}^{Z+}}\right] - S_{\mathrm{Ne}^{Z+}} \tag{3.24}$$

$$\frac{\partial}{\partial t}\left(\frac{3}{2} p_{\mathrm{Ne}^{Z+}}\right) = -\nabla \cdot \mathbf{q}_{\mathrm{Ne}^{Z+}} + v_{\|,\mathrm{Ne}^{Z+}} \partial_{\|} p_{\mathrm{Ne}^{Z+}} - E_{\mathrm{Ne}^{Z+}} \tag{3.25}$$

$$\frac{\partial}{\partial t}\left(m_{\mathrm{Ne}^{Z+}} n_{\mathrm{Ne}^{Z+}} v_{\|,\mathrm{Ne}^{Z+}}\right) = -\nabla \cdot \left[m_{\mathrm{Ne}^{Z+}} n_{\mathrm{Ne}^{Z+}} \mathbf{b} v_{\|,\mathrm{Ne}^{Z+}}\right] - \partial_{\|} p_{\mathrm{Ne}^{Z+}} - F_{\mathrm{Ne}^{Z+}} \tag{3.26}$$

$$\mathbf{q}_{\mathrm{Ne}^{Z+}} = \frac{5}{2} p_{\mathrm{Ne}^{Z+}} \mathbf{b} v_{\|,\mathrm{Ne}^{Z+}} \tag{3.27}$$

The sources/sinks of density and pressure $S_{\mathrm{Ne}^{Z+}}$ and $E_{\mathrm{Ne}^{Z+}}$ for the neon ions are primarily produced by collisional reactions, while the force $F_{\mathrm{Ne}^{\mathrm{z}+}}$ imposed on these neon ions is due to friction force, collisional reactions, thermal forces (section 3.5.3) and parallel electric field ($E_{\|}$).

The parallel electric field is calculated using the electron force balance [133][134][135][136], which balances all the forces on electron $F_{\mathrm{e,total}}$, including the electron pressure gradient, collisional friction and thermal force. It can be written as $-\nabla \cdot p_e + F_{\mathrm{e,total}} = n_e E_{\|}$. Thus the force due to the parallel electric field on all charged particles are $F_{p,E_{\|}} = Z n_p^Z E_{\|}$ 'p' represents ion species and Z is the charge number.

Impurity seeding

In experiments, neon gas is injected with a constant inflowing flux localized within a region in front of the target. To model this process, a constant particle flux $\Gamma_{\mathrm{Ne}^{0+}}$ localized in parallel direction is set for neutral neon density. To avoid numerical instability caused by the sharp gradient in parallel direction, the inflowing flux is set as an exponential function:

$$\Gamma_{\mathrm{Ne}^{0+}} = \Gamma_{\mathrm{peak,Ne}^{0+}} \mathrm{exp}\left(-\mathrm{C}\left(\theta - \theta_{1/2}\right)^2 / \left(0.5\mathrm{w}_{\mathrm{flux}}\right)^2\right) \tag{3.28}$$

where $\Gamma_{\mathrm{peak,\ Ne}^{0+}}$ is the peak value in the inflowing flux profile and C is a constant for adjusting the exponential distribution. The injection flux is localized in a parallel range $\theta_0 < \theta < \theta_1$ in parallel direction and the centre of the flux is $\theta_{1/2} = 0.5\left(\theta_0 + \theta_1\right)$. $w_{\mathrm{flux}} = \theta_1 - \theta_0$ is the parallel width of the inflowing flux.

Boundary conditions

The boundary conditions for neutral neon are listed below:

(1) The recycling fraction of neon ion flux (for any charge state) to the target is set to $f_{\mathrm{Ne}^{0+},\ \mathrm{recl}} = \frac{\Gamma_{\mathrm{Ne}0+,\mathrm{recl}}}{\Gamma^t_{\mathrm{Ne}^{Z+}}}$, where $\Gamma_{\mathrm{H}_2,\mathrm{recl}}$ is the flux of neutral neon produced by recycling in the final grid point at the target. Similar to the neutral molecules, the temperature of recycled neutral neon is given by the temperature of the facing material. The velocity of recycled neutral neon is equal to zero.

(2) The temperature boundary and density boundary of neutral neon are free.

The boundary conditions for the neon ions are:

(1) Bohm boundary conditions are used for Ne^{Z+} at the target. So the parallel plasma velocity at the target is $v_{\|,\mathrm{Ne}^{Z+}} \geq c_{s,\mathrm{Ne}^{Z+}}$, where $c_{s,\mathrm{Ne}^{Z+}} = \sqrt{\frac{2\times T_{\mathrm{Ne}^{Z+}}}{m_{\mathrm{Ne}^{Z+}}}}$

(2) The density and pressure boundaries of neon ions are ‘free’.

(3) The temperature gradient of neon ions at the sheath entrance is zero.

(4) The energy flux related to a sheath heat transmission ($\gamma = 6$) is:
$q_{\mathrm{Ne}^{Z+}} = \gamma n_{\mathrm{Ne}^{Z+}} T_{\mathrm{Ne}^{Z+}} c_{s,\mathrm{Ne}^{Z+}}$

Important assumptions

Since neon ions are included in physical model, the trace assumption used in section 3.4.2 will not be available any more. Therefore the quasineutrality assumption $n_e = n_{\mathrm{H}^+}$ cannot be used in the new SD1D. In this upgrade, it is assumed that $n_e = n_{\mathrm{H}^+} + n_{\mathrm{H}_2^+} + \sum_{Z=0}^{10} Z n_{\mathrm{Ne}^{Z+}}$ thus the H^+ temperature of and electron temperature are different in the new model.

3.5.2 Collision model

In the collision model, (1) the collision between charged particles, (2) the collision between charge particles and neutrals and (3) the collision between neutral particles are included.

Based on the collision model in the Hermes module of BOUT++ [136][135][19], the force on a charged particle 'a' due to collisions with particle species 'b' is

$$F_{a,b} = C_m V_{ab} m_a n_a (v_b - v_a) \tag{3.29}$$

The energy exchange is also caused by the collision. For instance, the energy transferred from species 'b' to 'a' due to the temperature difference can be written as:

$$Q_{a,b} = V_{ab} \frac{3 m_a n_a (T_b - T_a)}{m_a + m_b} \tag{3.30}$$

In these two expressions, C_m is the coefficient for parallel flows. For most situation it equals 1, but for electron-ion collision $C_m = 0.51$. V_{ab} is the collision frequencies, which is:

$$V_{ab} = \frac{1}{3\pi^{3/2}\epsilon_0^2} \frac{Z_a^2 Z_b^2 n_b ln\Lambda}{\left({v_a}^2 + {v_b}^2\right)^{3/2}} \frac{\left(1 + \frac{m_a}{m_b}\right)}{{m_a}^2} \tag{3.31}$$

The Coulomb logarithm $\ln \Lambda$ is different for ion-ion collision and electron-ion collision.

(1) For thermal electron-electron collisions:

$$\ln \lambda_{ee} = 30.4 - \frac{1}{2}\ln\left(n_e\right) + \frac{5}{4}\ln\left(T_e\right) - \sqrt{10^{-5} + \left(\ln T_e - 2\right)^2/16} \tag{3.32}$$

(2) Electron-ion collisions have four situations:

$$\ln \lambda_{ei} = 10 \qquad\qquad if\ T_e < 0.1eV\ or\ n_e < 10^{10}m^{-3} \tag{3.33}$$

$$\ln \lambda_{ei} = 30 - \frac{1}{2}\ln\left(n_e\right) - \ln(Z) + \frac{3}{2}\ln\left(T_e\right) \qquad\qquad if\ \ T_i m_e/m_i < T_e < 10Z^2 \tag{3.34}$$

$$\ln \lambda_{ei} = 31 - \frac{1}{2}\ln\left(n_e\right) + \ln\left(T_e\right) \qquad\qquad if\ \ T_i m_e/m_i < 10Z^2 < T_e \tag{3.35}$$

$$\ln \lambda_{ei} = 23 - \frac{1}{2}\ln\left(n_i\right) + \frac{3}{2}\ln\left(T_i\right) - \ln\left(Z^2 m_i\right) \qquad\qquad if\ T_e\ < T_i m_e/m_i \tag{3.36}$$

(3) Ion-ion collisions:

$$\ln \lambda_{ii'} = 29.91 - \ln\left[\frac{ZZ'\left(m_i + m_{i'}\right)}{m_i T_{i'} + m_{i'} T_i}\left(\frac{n_i Z^2}{T_i} + \frac{n_{i'} {Z'}^2}{T_{i'}}\right)^{1/2}\right] \tag{3.37}$$

More details of its definition can be found in [136][135][19].

In terms of neutral-neutral collisions, the collision rate is defined as

$$V_{ab}{}' = \sqrt{\frac{eT_a}{m_a} + \frac{eT_b}{m_b}} n_b \sigma \tag{3.38}$$

where $\sqrt{\frac{eT_a}{m_a} + \frac{eT_b}{m_b}}$ represents the mean relative velocity of species ‘a’ and ‘b’. The cross-section $\sigma = \pi\left(\frac{d_a+d_b}{2}\right)^2$. where d_a and d_b are the kinetic diameters of the two particle species.

The collision between neutrals and neon ions is also considered in the new model. But for simplicity, just take a value $5 \times 10^{-19}\mathrm{m}^2$ from the NRL formulary [136][137]

3.5.3 Thermal forces

Based on the thermal force used in the Hermes module of BOUT++ [136][19], the thermal force induced by electron temperature gradient is defined as:

$$F_{\mathrm{th,e}} = 0.71 n_{\mathrm{Ne}^{Z+}} Z^2 \nabla_{\|} T_e \tag{3.39}$$

For the thermal force induced by ion temperature gradient, it can be written as:

$$F_{\mathrm{th,H^+}} = \beta n_{\mathrm{Ne}^{Z+}} \nabla_{\|} T_{\mathrm{H^+}} \tag{3.40}$$

where $\beta = \frac{3\left(\mu+5\sqrt{2}Z^2\left(1.1\mu^{\frac{5}{2}}-0.35\mu^{\frac{3}{2}}\right)-1\right)}{2.6-2\mu+5.4\mu^2}$ and $\mu = m_{\mathrm{Ne}^{Z+}}/\left(m_{\mathrm{Ne}^{Z+}} + m_{\mathrm{H^+}}\right)$. The force on the light ion fluid is equal and opposite.

3.6 Conclusions

Based on the upgraded SD1D in section 3.4, we added neon impurities in the SD1D physical model including its parallel dynamics and radiation. To model neon parallel transport which is mainly determined by the parallel force balance, the friction force, electron- and ion- thermal force, the force due to a parallel electric field and the force due to collisional reactions have been included based on the Hermes module in BOUT++ [136],

After the code upgrades, the density, momentum and pressure of all neon species can be simulated by the new SD1D, which can be used to study the divertor detachment induced by neon seeding in different divertor configurations. In Chapter 5, we implemented simulation to investigate the detachment process during neon seeding scan and compare the role of atomic and molecular processes during detachment caused by the upstream density ramp and neon seeding.

Chapter 4

The role of atomic and molecular processes during divertor detachment

Material in this chapter was published as part of the paper: *Investigation of the role of hydrogen molecules in 1D simulation of divertor detachment,* Yulin Zhou et al 2022 Plasma Phys. Control. Fusion 64 065006 [48]

4.1 Motivation

The MAST-U tokamak was the first to be designed with a so-called 'super-X' divertor, which extends the divertor leg in order to spread the arriving heat over a much larger area [138][139]. Tests at MAST-U, which began operating in October 2020, have shown at least a tenfold reduction in the heat on materials with the Super-X system [23]. To understand the divertor performance and to design divertors for the future devices, it is essential to understand the complex atomic and molecular processes in divertor conditions, to explain and extrapolate these results. The surface recycling process, which significantly affects plasma-neutral interactions near the target, is much different on different plasma-facing materials. The ratio of recycled atoms and recycled molecules that depends on the target material can be varied on different materials [91]. Since the future reactors will probably have metal walls and many current devices including MAST-U have carbon walls, it is important to investigate the effects of the different recycling conditions on the divertor physics, especially divertor detachment.

Most detachment experiments are implemented to study the macroscopic processes such as heat flux, target temperature, volumetric radiation. Less attention has been put on the underlying atomic and molecular reactions, which play a crucial role in the particle, power and momentum balance [35]. In this work, we numerically study the role of atomic and molecular procresses during detachment in MAST-U super-X divertor conditions. The newly developed code 'SD1D' (section 3.4) is used to model the individual atomic and molecular processes and can provide deeper insight in the detachment physics.

4.2 Setup and initial parameters

Investigating the variation of the plasma flux reaching the divertor target is a useful way to define the plasma detachment in both numerical simulation and experimental research. In this chapter, the rollover of the target plasma flux Γ_{target} is studied in the scans of upstream density. We compare the target particle flux and target temperature to investigate the effects of atomic and molecular processes during detachment with 1% carbon [48]. The simulations in this chapter are implemented using the upgraded SD1D code (without impurity seeding) described in section 3.4

To set up the simulations, the expected MAST-U Super-X divertor conditions are applied for the following work in this chapter: [48][36][140]

(1) The parallel heat flux is $50\mathrm{MWm}^{-2}$ at the X-point;

(2) The connection length is 30m (20 m from X-point to target);

(3) The upstream density scan is from $1.5 \times 10^{19}\mathrm{m}^{-3}$ to $4.5 \times 10^{19}\mathrm{m}^{-3}$.

(4) The effect of gradients in total magnetic field is considered with an area expansion factor (the ratio of $\frac{Total\ field\ at\ X-point}{Total\ field\ at\ target}$)) of 2 between X-point and target.

(5) Recycling fraction equals 99%, which means 99% of plasma ion flux arriving at the target is recycled for neutrals.

Since ions can be converted to neutral atoms or neutral molecules at the target, their relative ratio depending on the target material (and to a lesser extent, conditions) can be varied [91]. Here we include both recycling channels by changing such a ratio in a way that either atoms or molecules prevail. We have approached the problem by choosing three cases: one with just molecules as the recycling output, another with just atoms and a third with ions recycling as atoms or molecules with equal probability [48]. As mentioned in section 3.4, the recycling temperature of neutral molecules and neutral atoms are $T_{\mathrm{H_2,recycle}} = 0.1\mathrm{eV}$ (based on the temperature of the facing material) and $T_{\mathrm{H,recycle}} = 3.5\mathrm{eV}$ (based on the Franck-Condon energy [115]) in our simulations.

4.3 Study of the divertor detachment with different recycling conditions

In this section, we implemented a comparison of the target plasma rollover and target temperature in the three recycling regimes: (1) only neutral atoms produced by recycling (labelled '$\mathrm{H^+ \to H}$'), (2) only neutral molecules produced by recycling (labelled '$\mathrm{H^+ \to H_2}$') and (3) recycled atoms or recycled molecules with equal probability (labelled '$50\%(\mathrm{H^+}- > \mathrm{H})\&50\%(\mathrm{H^+}- > \mathrm{H_2})$'). In the case with a larger recycling fraction for hydrogen molecules in figure 4.1. it is found that the flux rollover occurs at a higher n_{up} (varied from $1.67 \times 10^{19}\mathrm{m}^{-3}$ to $1.92 \times 10^{19}\mathrm{m}^{-3}$) with a larger peak target flux, and the target temperatures at rollover gradually become lower. It indicates that using the target material that produces more recycled atoms may reduce the requirements for achieving divertor detachment. The reason is that the generation of hydrogen molecules from recycled ions reduces the atom source and thus atom density decreases. It leads to a lower direct electron-impact excitation radiation power loss and weaker the atom-plasma interactions, which are the main energy sinks and momentum sinks before rollover in the divertor (more details can be found in section 4.5. As shown in figure 4.2), the ratio of total amounts of molecules to atoms $\frac{\int n_{\mathrm{H_2}} dV}{\int n_{\mathrm{H}} dV}$ in the divertor can be up to 50% when all recycled plasma ions become molecules. Thus the plasma-atom collisional and radiative interactions are mitigated due to the smaller atom density.

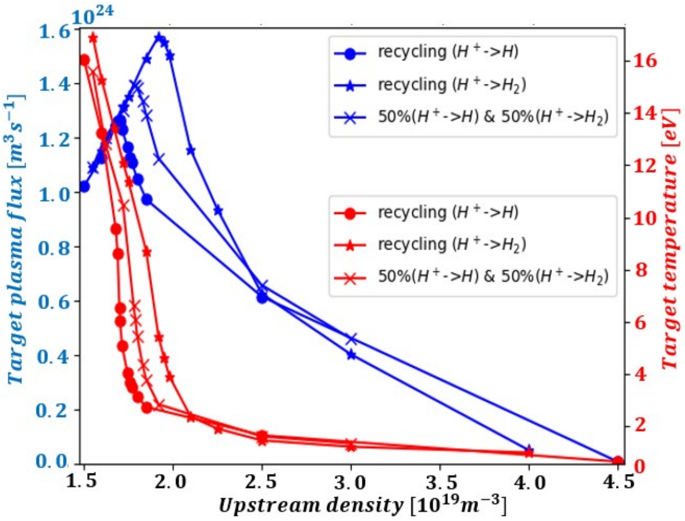

Figure 4.1: Upstream density scan for the cases (a) with 1% carbon impurity and without molecules labelled ‘recycling ($H^+ \rightarrow H$)’, (b) with 1% carbon and hydrogen molecules (All recycled ions becomes molecules in this case), labelled ‘recycling ($H^+ \rightarrow H_2$)’, and (c) with 1% carbon and hydrogen molecules (half recycled ions becomes molecules and half becomes atoms in this case), labelled ’50%($H^+ - > H$)&50%($H^+ - > H_2$)’.

The density profiles of H^+, H, H_2 and $H_2{}^+$ in figure 4.2 indicate that the plasma ion flux moving towards the target first interacts with neutral atoms, resulting in a strong ionisation source which leads to a ramp of ion density in front of the target. But the ion density dramatically decreases before hitting the molecule cloud (H and H_2^+) near the target because the ionisation source becomes small in the recycling region. Since the plasma density and electron temperature near the target (where molecular species are located) are relatively lower compared to the other regions, the hydrogen radiation from excited atoms after molecular break-up involving (H_2, H^-, H_2^+) is found to be much smaller than the direct electron-impact excitation radiation. Thus direct electron-impact excitation radiation power loss is larger than the power loss produced by molecular excitation channels.

After the target ion flux rollover in figure 4.1, the plasma ion flux reaching the target starts dropping with the increase of upstream density. Since the recycling flux is proportional to the target ion flux, the molecule density is found to quickly rise at the beginning of detachment and then decreases with the drop of target ion flux in deep detachment phase. When $T_e < 1$eV, more atoms can be produced by recombination in the divertor.

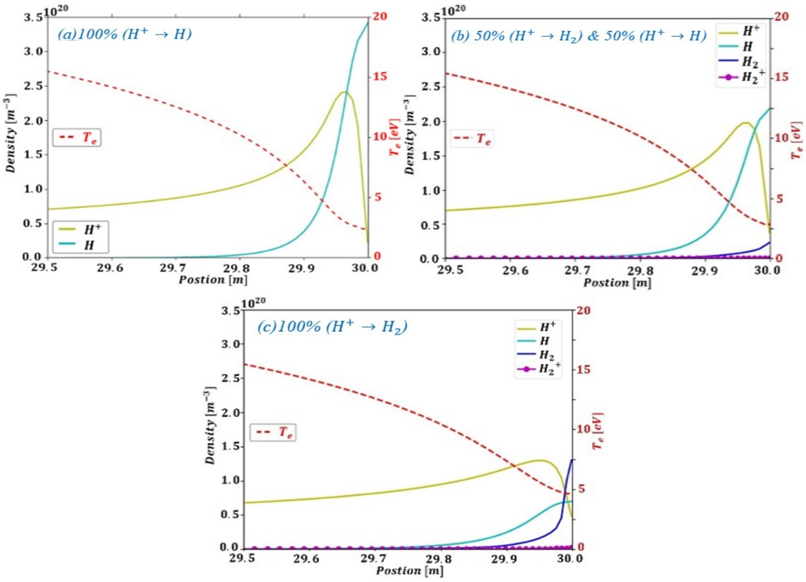

Figure 4.2: Density profiles of H$^+$, H, H$_2$, H$_2^+$ and temperature profile of electron in the case with (a) all the recycled ions converting into atoms (H$^+ \rightarrow$H), (b) 50% recycled ions becoming atoms and the other half becoming molecules (50%(H$^+ - >$ H)&50%(H$^+ - >$ H$_2$)), and (c) all the recycled ions converting into molecules (H$^+ \rightarrow$H$_2$). The upstream density is $n_{up} = 1.92 \times 10^{19}$m^{-3} for all the three cases, corresponding to the three cases at $n_{up} = 1.92 \times 10^{19}$m^{-3} in figure 4.1. The target is located at the position of 30m.

In figure 4.2, the H$_2{}^+$ density is small compared to other species, but it cannot be ignored and it even plays an important role during divertor detachment. H$_2{}^+$ is a crucial intermediate product of molecular activated recombination (MAR) and it is also an important excitation channel which affects the hydrogen excitation radiation, both of which can affect the particle, momentum and power balance in the divertor. Additionally H$_2{}^+$ is a crucial channel for photon emissions, which will become strong during the detachment phase.

To further understand the role of atomic and molecular reactions, section 4.5 discusses the region of the different reactions along parallel direction and the effects of different reaction types on plasma momentum loss.

4.4 Power and particle balance

Our calculations also allow us to gain insight into the dissipation mechanisms at play. According to the pressure balance in the Two Point Model [19], the upstream and target static pressures can be written as $p_{up} = 2p_{target}$ if no momentum losses are considered. If the plasma-neutral interactions are considered, the plasma momentum will be varied along the SOL. According to equation 2.23, a momentum loss factor is defined as:

$$f_m = 1 - 2p_{target}/p_{up} \tag{4.1}$$

The studies using the original SD1D in the same MAST Upgrade like conditions [36] found that this momentum loss factor could be written as an exponential function:

$$\frac{2p_{target}}{p_{up}} = 1 - f_m = 0.9\left[1 - e^{(\frac{-T_{target}}{2.1})}\right]^{2.9} \tag{4.2}$$

To make quantitative comparison, the momentum loss factor is estimated by the Self-Ewald model, which uses charge exchange to ionisation ratio measurements [36][141][19]. The momentum loss factor calculated by the Self-Ewald model can be written as a function of ionisation and charge exchange rate coefficients [141]: $1 - f_m = \left[\frac{\alpha}{\alpha+1}\right]^{(\alpha+1)/2}$, where $\alpha = <\sigma v>_{ion}/\left(<\sigma v>_{ion} + <\sigma v>_{cx}\right)$. It assumes that the atom-ion charge exchange imposes a drag force on the plasma ions, while ionisation produces plasma ions. This momentum loss mechanism is determined by ionisation and charge exchange, but it ignores many other factors, e.g. molecule-plasma interactions. In figure 4.3, it is found that the simulation result is qualitatively similar to the Self-Ewald result, both of which show that the ratio of $\frac{2p_{target}}{p_{up}}$ is about flat when $T_e > 10$eV at the target and steeply drops when the target temperature is lower than 10eV. But the Self-Ewald solution overestimates the momentum loss factor f_m leading to a lower ratio of$\frac{2p_{target}}{p_{up}}$ compared to the simulation results. The reason could be that it is assumed momentum loss in the Self-Ewald model is due to charge exchange events, which have the higher reaction rate coefficient compared to the other reactions. The Self-Ewald also assumes that every charge-exchange event completely removes that ion's momentum from the system. In the SD1D the momentum is transferred to the neutral species, and may be transferred back to the ions by another charge-exchange event. The rate of momentum loss is therefore much less than the Self-Ewald would predict.

In the upgraded SD1D, the main atomic and molecular processes have been significantly improved, such that the momentum loss factor obtained in simulations is based on a more complete collision model compared to the Self-Ewald model. As a consequence, we can plot $\frac{2p_{target}}{p_{up}}$ from the SD1D simulations in figure 4.3, with the data well fitted by an exponential expression for the momentum loss factor (the black solid line) [48]

$$\frac{2p_{target}}{p_{up}} = 1 - f_m = 0.889\left[1 - e^{(-\frac{T_{target}}{2.62})}\right]^{1.65} \tag{4.3}$$

Taking the target pressure from the expression above, we can now calculate the target ion flux: $\Gamma_{target} \propto n_{target}\sqrt{T_{target}} = p_{target}/\sqrt{T_{target}}$. Using the static pressure at the target $p_{target,static} = \frac{(1-f_m)p_{up,static}}{2}$ from equation 4.1, we can obtain the target ion flux Γ_{target} written as (static pressure at the target is $p_{target,static} = 2n_{target}T_{target} = 2p_{target}$:

$$\Gamma_{target} = p_{up,static}\frac{(1-f_m)}{\sqrt{8m_iT_{target}}} \tag{4.4}$$

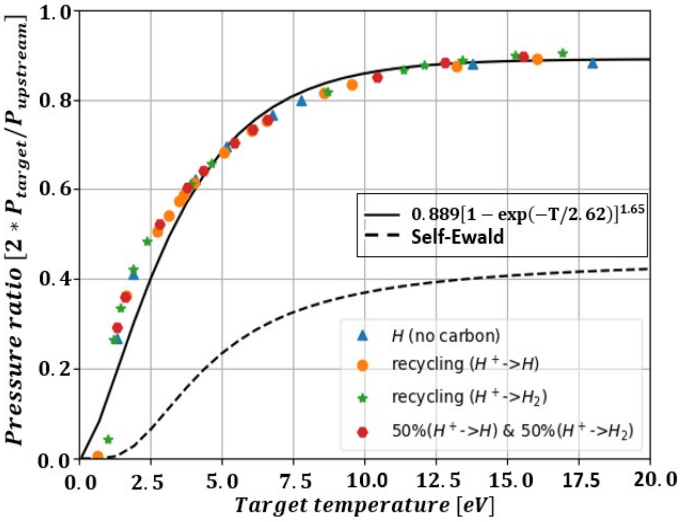

Figure 4.3: Ratio of $\frac{2p_{target}}{p_{up}}$ as a function of target temperature achieved from the simulation cases without molecules (labelled ‘H (no carbon)’ and ’recycling(H$^+$→H)’ and with molecules introduced by different recycling conditions (50%(H$^+-$ > H)&50%(H$^+-$ > H$_2$) and *recycling*(H$^+-$ > H$_2$))

To complement the upstream density scan in figure 4.1, it is interesting to visualize our results in a Γ_{target} versus target temperature plot at fixed p_{up} for the target

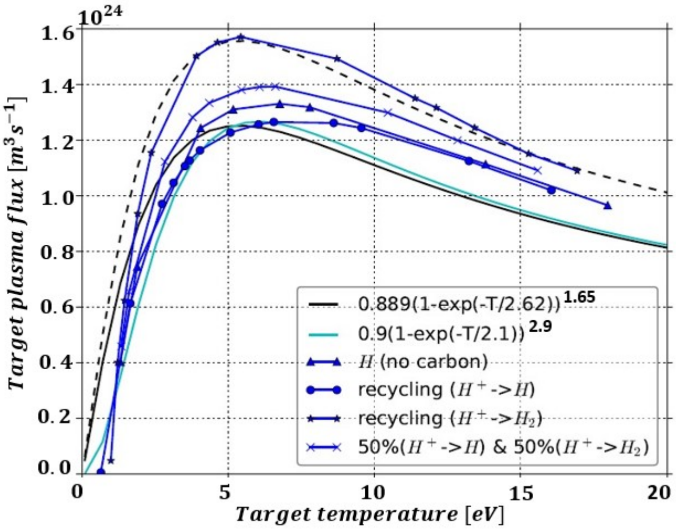

Figure 4.4: Target flux as a function of target temperature for the upstream density scan in the cases: 1) without impurity and molecules labelled ‘H (no carbon)’, 2) with 1% carbon and without molecules labelled ’recycling(H$^+ \to$H)’, 3) with 1% carbon and with hydrogen molecules labelled ’$recycling$(H$^+ -> $ H$_2$)’ and ’50%(H$^+ ->$ H)&50%(H$^+ ->$ H$_2$)’ . The celeste and black solid curves show the target flux calculated with equation 4.4 by using equation 4.2 and equation 4.3. The upstream density is $n_{up} = 1.97 \times 10^{19}/\text{m}^3$ for the black and celeste solid lines, while $n_{up} = 2.35 \times 10^{19}/\text{m}^3$ for the black dashed line.

ion flux. We compare the simulations to the analytical calculations (equation 4.4 obtained using the expressions of momentum loss factor $(1 - f_m)$ in equation 4.2 and equation 4.3. We found that the detachment roll over occurs for all simulations at around 5eV regardless the specific recycling conditions. We could see that equation equation 4.4) together with the exponential expression in equation 4.3 gives a curve for Γ_{target} that rolls over at a fixed target temperature as long as p_{up} does not vary much with the target temperature. To be more specific, we observe a small variation of the plasma temperature at rollover, with higher values (6.7eV) for recycling of pure atoms and smaller values (5.3eV) for pure molecular recycling [48].

According to the Two Point Model in section 2.3.2, the input power P_{in} can be dissipated by (1) impurity radiation P_{imp}, (2) ionisation in the target region P_{ion} and (3) the rest of the power arriving the target P_{target}. According to [68][36], we define the power entering the recycling region as:

$$P_{\text{recl}} = P_{\text{ion}} + P_{target} = (E_{\text{ion}} + \gamma T_{target})\,\Gamma_{target} \tag{4.5}$$

where $\gamma T_{target}\Gamma_{target}$ represents the heat flux at the target and E_{ion} is the effective ionisation energy, which includes the energy loss by hydrogen ionisation (e.g. 13.6eV) and by net hydrogen excitation radiation. Together with the equation 4.4, the detachment parameter $\frac{p_{up}}{P_{\text{recl}}}$ (p_{up} represents upstream pressure) could be obtained [142]:

$$\frac{p_{up}}{P_{\text{recl}}} = \frac{\sqrt{8m_i T_{target}}}{(1-f_m)\,(E_{\text{ion}} + \gamma T_{target})} = \frac{\sqrt{8m_i\gamma}\;{E_{\text{ion}}}^{-\frac{1}{2}}\left(\frac{\gamma T_t}{E_{\text{ion}}}\right)^{\frac{1}{2}}}{(1-f_m)\left(1+\frac{\gamma T_t}{E_{\text{ion}}}\right)} \tag{4.6}$$

As shown in equation 4.3, $1 - f_m = \frac{2p_{target}}{p_{up}}$ is a function of target temperature. Thus, both the target temperature and the effective ionisation energy E_{ion} when rollover occurs determine the detachment threshold $\frac{2p_{target}}{p_{up}}$. When $T_t < 10\text{eV}$, it steeply drops to zero. If a fixed ionisation energy is used in calculation, $\frac{p_{up}}{P_{\text{recl}}}$ grows as the target temperature decreases (dashed line in figure 4.5). We can absorb the effect of neutral radiation in the ionization energy in an ad hoc way, which is an approximation that is sometimes used to capture both effects. If we do so, E_{ion} becomes a function of the target temperature, which now would represent the total energy loss of ionisation plus net hydrogen atom excitation radiation divided by the ionisation rate. This assumes that all ionisation occurs directly at the target (e.g. occurs at a target temperature T_t). We have shown this quantity as a red solid line in figure 4.5, by using our numerical results from the simulation with pure molecular recycling. We have found that the other simulations with different recycling conditions produced similar results. Using this in (equation 4.6, we find that the ratio of $\frac{p_{up}}{P_{\text{recl}}}$ is about 9.5N/MW at high temperatures, and it quickly decreases when $T_t < 10\text{eV}$, as the blue solid line shows in figure 4.5. Generally, the target flux rollover, indicating onset of detachment, occurs when a critical value of the gradient of E_{ion} with respect to T_t is achieved [36][131][48][68][19]),

$$\frac{\partial\, E_{\text{ion}}}{\partial\, T_t} < -\gamma \tag{4.7}$$

For the sheath transmission coefficient γ used in this paper ($\gamma = 6$), we find $T_t = 5.6$eV and the corresponding effective ionisation energy $E_{ion} = 82.23$eV. This corresponds to the value of the detachment parameter given below

$$\frac{p_{up}}{P_{\mathrm{recl}}} = 8.1 \text{ N/MW} \tag{4.8}$$

The simulation results of the original SD1D provide a smaller value of the detachment parameter, which is about 12.6 N/MW [36], while it is 17 N/MW in SOLPS4.3 simulation on DIII-D like equilibria [142]. The different results obtained in the upgraded SD1D and the original version may be due to different effective ionisation energy $E_{\mathrm{ion}} = 60.8$eV in the previous version). Variations in this quantity with model assumptions and inputs are expected: The ratio $\frac{p_{up}}{P_{\mathrm{recl}}}$ is not a universal quantity though it has a physical basis. This quantity is however experimentally measurable, and is an important metric that can be used for comparisons between simulation and experiments [48].

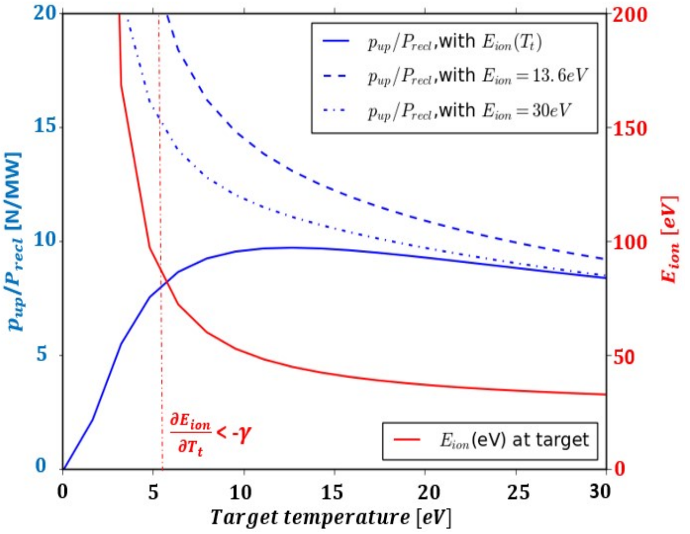

Figure 4.5: $\frac{p_{up}}{P_{\mathrm{recl}}}$ as a function of target temperature and effective ionisation energy E_{ion} (equation 4.6). $\frac{p_{up}}{P_{\mathrm{recl}}}$ is calculated with fixed $E_{\mathrm{ion}} = 13.6\mathrm{eV}, 30\mathrm{eV}$ and with the $E_{\mathrm{ion}}(T_t)$ as a function of target temperature (which is the total energy loss of ionisation and hydrogen atom emission divided by the ionisation rate as the red solid line shows). The threshold in equation 4.7 is marked by the vertical red dashed line.

4.5 Study of the role of atomic and molecular processes in divertor detachment

Plasma-atom and plasma-molecule interactions play a crucial role in the divertor, which significantly affect the divertor particle, momentum and energy balance and thus influence the divertor detachment process. As discussed in section 4.3, a recycling process producing fewer molecules leads to a smaller molecule density. In order to better study the role of molecular species, cases with just molecules as the recycling output are used in this section, including an attachment case $n_{up} = 1.55 \times 10^{19}/\mathrm{m}^3$, a case at about rollover $n_{up} = 1.92 \times 10^{19}/\mathrm{m}^3$, and a case at about detachment $n_{up} = 4.0 \times 10^{19}/\mathrm{m}^3$.

4.5.1 The particle sources and sinks of H^+ and H_2^+

First we investigated the parallel profile of sources and sinks of the main plasma ion (H^+). In SD1D simulations,

(1) The sources include ionisation ($\mathrm{e} + \mathrm{H} \rightarrow 2\mathrm{e} + \mathrm{H}^+$), dissociative ionisation (DI) ($\mathrm{e} + \mathrm{H}_2^+ \rightarrow 2\mathrm{e} + \mathrm{H}^+ + \mathrm{H}^+$) and dissociative excitation (DE)
($\mathrm{e} + \mathrm{H}_2^+ \rightarrow \mathrm{e} + \mathrm{H}^+ + \mathrm{H}$)

(2) The sinks include electron-impact recombination (EIR) ($\mathrm{H}^+ + \mathrm{e} \rightarrow \mathrm{H}$), molecular charge exchange ($\mathrm{H}^+ + \mathrm{H}_2 \rightarrow \mathrm{H}_2^+ + \mathrm{H}$)

Figure 4.6 shows the profile of the different reactions along parallel direction to the target (at 30m), indicating that ionisation is the main source of H^+ during attachment and detachment, while DE contributes a small part of the ion source in figure 4.6(a) and figure 4.6(b). All sinks are small in the attachment case, and then at rollover molecular charge exchange significantly increases and becomes the main sink during detachment. The ionisation region is located away from the target, further than the regions of molecular reactions since molecules are mainly concentrated near the target due to recycling at the target. With the increase of upstream density, the ionisation region starts moving upstream, while the plasma-molecule reactions still

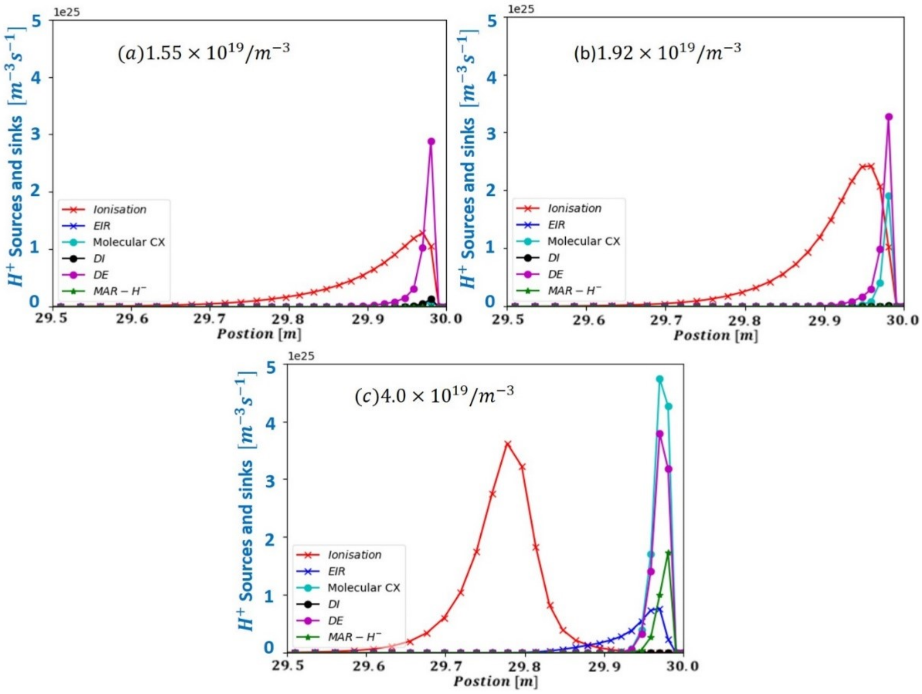

Figure 4.6: Parallel profile of sources and sinks of H$^+$ in the case with (a) $n_{up} = 1.55 \times 10^{19}/\text{m}^3$, (b) $n_{up} = 1.92 \times 10^{19}/\text{m}^3$ and (c) $n_{up} = 4.0 \times 10^{19}/\text{m}^3$

occur mainly near the target. It is also found that the peak of all the reactions (except DI) becomes higher at larger upstream densities. Together with H$_2^+$, H$^-$ is another intermediate product of MAR. It is found that MAR via H$^-$ accounts for a small part of ionisation sink in deep detachment phase (figure 4.6(c)), while it is negligible in the attached case and the rollover case. According to the electron-impact recombination reaction rate coefficient (in section 2.2.2), this process may become intensive when $T_e < 1$eV. In our simulation, a growth of recombination sink can be found in the deep detachment case, but it is still small compared to the main ion sink (molecular charge exchange) since T_e at the target is not low enough.

Compared to figure 4.2(c), the plasma-atom and plasma-molecule reaction region in figure 4.6(b) corresponds to the density profile of the neutral atom and the neutral molecule. The ionisation region is primarily determined by the neutral atom profile, thus it is found that the parallel range of ionisation region and atom density profile are distributed in a similar region (from about 29.7m to 30m). The ionisation source can significantly affect the ion density profile. The ramp of ionisation source near the target contributes to the ion density ramp in front of the target. The steep decrease of plasma ion density is caused by the drop of ion source near the target. The same for molecular reactions, the density profile of molecular species (primarily H_2 and H_2^+) determines the location of plasma-molecule interactions.

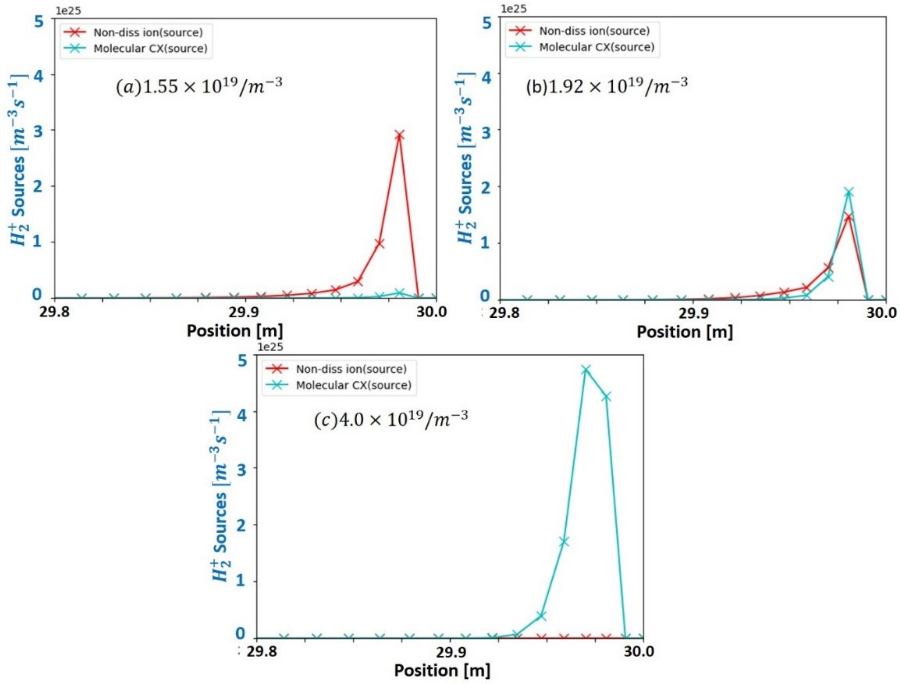

Figure 4.7: Parallel profile of sources of H_2^+ in the case with (a) $n_{up} = 1.55 \times 10^{19}/\mathrm{m}^3$, (b) $n_{up} = 1.92 \times 10^{19}/\mathrm{m}^3$ and (c) $n_{up} = 4.0 \times 10^{19}/\mathrm{m}^3$

As discussed in section 2.2.2 and section 2.2.3, H_2^+ is an important particle species in divertor plasma. Although the density of H_2^+ is small compared to the main ion density, investigating the sources and sinks of H_2^+ is crucial to understand its effect on particle, momentum and energy balance during divertor detachment. As shown in figure 4.7, the sources of H_2^+, including non-dissociative ionisation $\mathrm{e} + H_2 \rightarrow 2\mathrm{e} + H_2^+$ and molecular charge exchange $H^+ + H_2 \rightarrow H_2^+ + \mathrm{H}$ (see table 3.1) are located in the region close to the target. In the attached case, non-dissociative ionisation is the dominant H_2^+ source compared to molecular charge exchange in figure 4.7(a), while molecular charge exchange becomes stronger at rollover figure 4.7(b) and dominates over the H_2^+ source in the detached case figure 4.7(c). In terms of the sinks in figure 4.8, dissociative excitation is always the main H_2^+ sink from attachment to detachment, but it does not increase much at different upstream densities, while dissociative

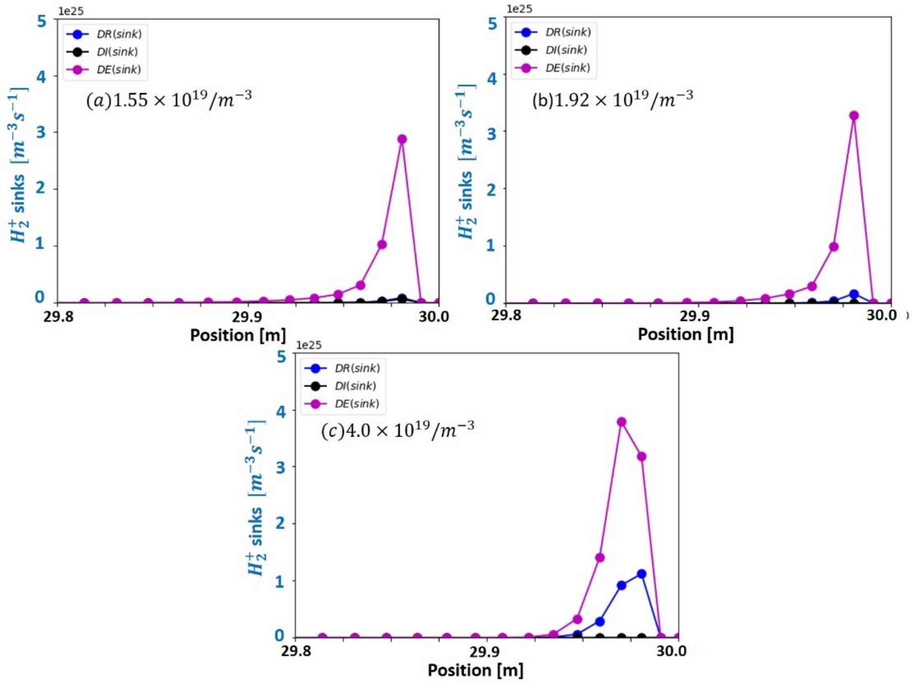

Figure 4.8: Parallel profile of sinks of H_2^+ in the case with (a) $n_{up} = 1.55 \times 10^{19}/\mathrm{m}^3$, (b) $n_{up} = 1.92 \times 10^{19}/\mathrm{m}^3$ and (c) $n_{up} = 4.0 \times 10^{19}/\mathrm{m}^3$

recombination slightly increases in the detachment case. With increasing upstream density, the reaction region of the H_2^+ sources and sinks do not vary, remaining in a narrow region in front of the target. It indicates that the interactions with H_2^+ (e.g. MAR via H_2^+) mainly affect the atomic and molecular process within this narrow region.

When $T_e < 3\mathrm{eV}$ the dissociation process ($\mathrm{e} + \mathrm{H}_2 \rightarrow \mathrm{e} + \mathrm{H} + \mathrm{H}$) will become weak due to the steep decrease of its reaction rate coefficient in figure 2.2 in section 2.2.2, while the most neutral atoms near the target are produced by interaction with H_2^+ and H^- (e.g. dissociative recombination, dissociative excitation and MAR via H^-) due to their higher rate coefficient in figure 2.3 in section 2.2.2. Although the density of H_2^+ (and probably H^-) is small compared to the density of other species, interactions with H_2^+ and H^- may be important to determine the neutral density profile below the ionisation region.

4.5.2 Hydrogen excitation radiation through different channels

As discussed in section 3.4.3, there are 5 excitation channels considered in the new SD1D physical model, including two atomic excitation channels: direct electron-impact excitation (via H) and electron-ion recombination (via H^+), and three molecular excitation channels: dissociation (via H_2), dissociative recombination (via H_2^+) and mutual neutralization (via H^-). Figure 4.9 shows the parallel profile of hydrogen excitation radiation power through the different excitation channels. It is found that direct electron-impact excitation is the dominant excitation channel in the three cases, while its profile moves up to the X-point with increasing upstream density. The movement of hydrogen radiation profile strongly corresponds to the variation of ionisation source profile in figure 4.6, both of which are mainly determined by the neutral atom density profile. Similar to the molecular reaction region, the profile of radiation power produced by molecular excitation channels is primarily distributed in the narrow region in front of the target and it does not move towards the X-point with increasing upstream density.

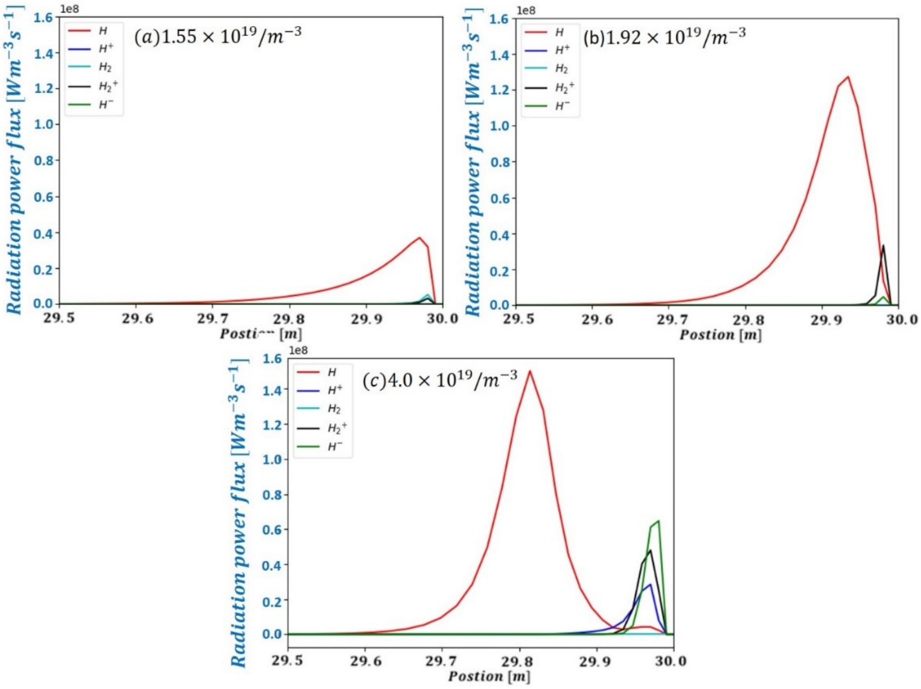

Figure 4.9: Parallel profile of hydrogen excitation radiation power though different excitation channels in the case with (a) $n_{up} = 1.55 \times 10^{19}/\mathrm{m}^3$, (b) $n_{up} = 1.92 \times 10^{19}/\mathrm{m}^3$ and (c) $n_{up} = 4.0 \times 10^{19}/\mathrm{m}^3$

In figure 4.9(a), molecular channels provide a small part of the hydrogen excitation radiation power and then the dissociative recombination (via H_2^+) and mutual neutralization (via H^-) becomes stronger in figure 4.9(c). Although they are still small compared to the direct electron-impact excitation radiation which contributes over 85% of hydrogen radiation power loss in the detachment case, the channel H_2^+ and channel H^- are the main excitation channel in front of the target. Together with the discussion of particle sources and sinks, it indicates that the plasma and neutral profiles in front of the target are primarily determined by molecular species during detachment.

Although the density profile of H_2^+ is small (less than 2% of neutral molecule density when Te is about 2eV), it is found that dissociative recombination (via H_2^+) and mutual neutralization (via H^-) become the main molecular excitation channels in the deep detachment phase. It is expected from their reaction rate coefficient (section 2.2.3) that the two channels will be stronger at lower target temperatures. This result indicates that although the atomic and molecular processes depends on their density which may be small near the target during the detachment process, the reaction probability may become large at low electron temperatures. Thus the effect of atomic and molecular processes on divertor physics depends on both their density and the electron temperature. For instance, the density of neutral molecule H_2 is much larger than H_2^+ density, but the hydrogen excitation radiation via H_2 is negligible due to its small emissivity at low temperatures compared to H_2^+.

4.5.3 The role of plasma-atom and plasma-molecule in volumetric momentum loss and H_{alpha} photon emission

The sources and sinks of the main ion shown in section 4.5.1 and section 4.5.2 can not only affect the divertor particle balance and energy balance, but also significantly impact the momentum balance in the divertor. In the high recycling regime, the neutral density becomes very high (the peak density of neutrals can be over $5 \times 10^{21} \mathrm{m}^{-3}$ during deep detachment) near the target, which can effectively reduce the plasma ion momentum before the ion flux reaching the target. The momentum loss is primarily through the plasma-neutral collisions, including plasma-atom change exchange, plasma-atom elastic collision, plasma-molecule charge exchange, and plasma-molecule elastic collision.

The study in [38][131] found that the molecular charge exchange between the main ion and hydrogen molecules ($H^+ + H_2 \rightarrow H_2^+ + H$) may lead to a rise of plasma ion momentum loss in the low temperature region. It will be interesting to compare the momentum loss produced by the different collisions. In this work, we use a momentum loss factor $f_{momloss} = \left(\sum_p \int_{up}^{target} F_{\mathrm{H+-p}} dl\right) / p_{up}$, where $\sum_p \int_{up}^{target} F_{\mathrm{H+-p}} dl$ is the total pressure loss of H^+ by the collisions with other particle species 'p' ($F_{\mathrm{H+-p}}$ represents collision force).

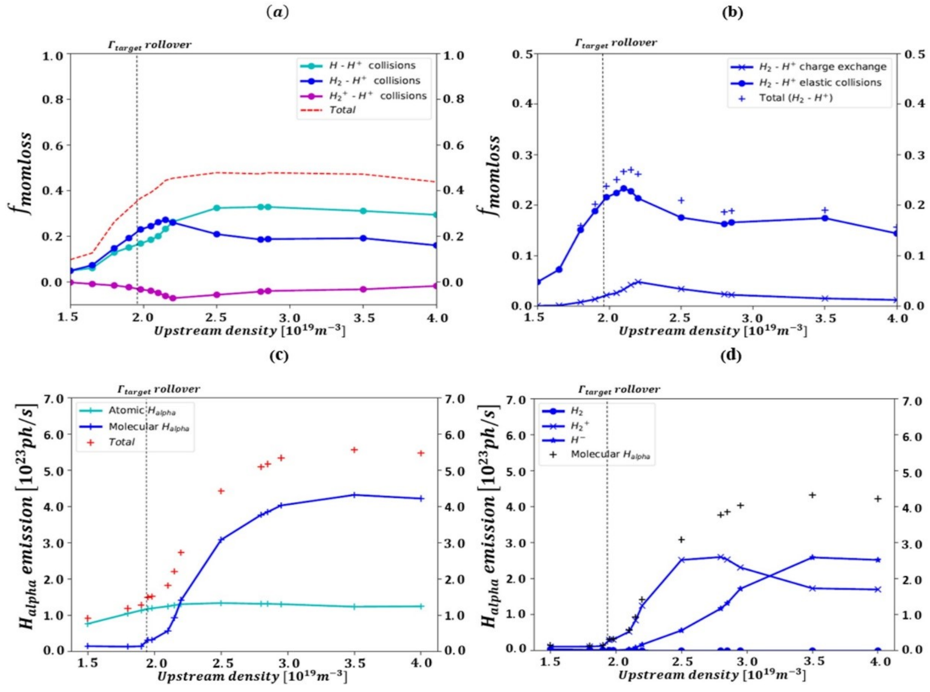

Figure 4.10: (a) Decomposition of momentum loss factor $f_{momloss}$ due to different reaction types, labelled as '$\mathrm{H} - \mathrm{H}^+$', '$\mathrm{H}_2 - \mathrm{H}^+$', '$\mathrm{H}_2^+ - \mathrm{H}^+$' collisions, and their total $f_{momloss}$ (the red dashd) when all recycled ions become molecules; (b) Decomposition of $f_{momloss}$ caused by $\mathrm{H}_2 - \mathrm{H}^+$ collisions.(c) decomposition of total $\mathrm{H}_{\mathrm{alpha}}$ photon emission due to atomic and molecular channel, (d) decomposition of $\mathrm{H}_{\mathrm{alpha}}$ photon emission through molecular channels. Vertical dashed lines indicates the position of Γ_{target} rollover.

In this section, all the relevant collision forces are obtained from the case (recycling $\mathrm{H}^+ \rightarrow \mathrm{H}_2$) with different upstream density. We found that plasma-molecule collisions account for a rapid rise of momentum loss at the beginning of upstream density scan in figure 4.10(a). At the beginning of detachment, the momentum loss caused by plasma-molecule collisions grows faster compared to plasma-atom collisions. The reason could be that the density of neutral molecule rapidly increases near the target at the beginning of detachment due to the large recycling neutral flux (when upstream density $n_{up} < 2.2 \times 10^{19}/\mathrm{m}^3$), resulting in the neutral molecule density n_{H_2} larger than the neutral atom density n_{H}. But when the n_{up} becomes larger, the growth of momentum loss by plasma-molecule collisions becomes slower since the molecule density is found to increase slowly and it even decreases at high upstream densities ($n_{up} > 3.5 \times 10^{19}/\mathrm{m}^3$) due to the decrease of recycling source (plasma ion flux at the target Γ_{target}). With the decrease of target ion flux in the deep detachment phase, it is found that $n_{\mathrm{H}_2} < n_{\mathrm{H}}$ near the target, such that plasma-atom collisions can provide a larger part of momentum loss compared to plasma-molecule collisions in the deep detachment phase. In figure 4.10(b), it compares the momentum loss caused by the two main plasma-molecule collisions, charge exchange and elastic collision. The simulation results predict that the momentum loss mechanism via plasma-molecule interactions is primarily due to plasma-molecule elastic collisions, instead of molecular charge exchange. The main reason is that the rate coefficient of plasma-molecule elastic is about 10 times larger than molecular charge exchange when $T_e < 10\mathrm{eV}$ [44].

$\mathrm{H}_{\mathrm{alpha}}$ **photon emission**

As discussed in section 4.5.2, there are 5 excitation channels considered in SD1D physical model, including two atomic excitation channels: direct electron-impact excitation (via H) and electron-ion recombination (via H^+), and three molecular excitation channels: dissociation (via H_2), dissociative recombination (via H_2^+) and mutual neutralization (via H^-). The excited atoms produced via different excitation channels can affect the $\mathrm{H}_{\mathrm{alpha}}$ photon emission (section 2.2.4), which is crucial for tokamak experiment diagnostics, and conveys information on neutral density and neutral-plasma interactions. Since it is still a challenge to experimentally measure the molecular processes, the part of $\mathrm{H}_{\mathrm{alpha}}$ photon emission attributing to plasma-molecule interactions is usually ignored in experimental results. To fully understand the $\mathrm{H}_{\mathrm{alpha}}$ photon emission during detachment, we use the upgraded SD1D code developed in this work to investigate the importance of different excitation channels in the case with different upstream density. In figure 4.10(c), simulations found that atomic channels (primarily direct electron-impact excitation) dominate $\mathrm{H_{alpha}}$ emission before Γ_{target} rollover and then change little during detachment, while molecular channels account for the strong rise of $\mathrm{H_{alpha}}$ signal, which grows to be about 5 times the $\mathrm{H_{alpha}}$ emission at Γ_{target} rollover ($n_{up} = 1.92 \times 10^{19}/\mathrm{m}^3$). This is mainly due to the fast growth of molecule density near the target at the beginning of detachment and then due to the increase of $\mathrm{H_{alpha}}$ emission coefficients via dissociative excitation '$\mathrm{H_2^+}$' and mutual neutralization '$\mathrm{H^-}$' (see figure 2.7) with the decrease of T_e when $Te < 3\mathrm{eV}$. This result well matches the measured and predicted photon emission on TCV [143]. Further analysis of the decomposition of molecular channels in figure 4.10(d) shows the rise of $\mathrm{H_{alpha}}$ signal is firstly due to $\mathrm{H_2^+}$ channel ($1.92 \times 10^{19}/\mathrm{m}^3 < \mathrm{n_{up}} < 2.5 \times 10^{19}/\mathrm{m}^3$) and then $\mathrm{H^-}$ channel becomes more important when the target gets further detached ($n_{up} > 2.5 \times 10^{19}/\mathrm{m}^3$).

4.6 Comparison of SD1D simulations of divertor detachment with SOLPS-ITER results

We use the SOLPS-ITER code to investigate divertor detachment in the MAST-U super-X divertor configuration and compare against SD1D results. To make the simulations of the two codes comparable, the set of particle species and their reactions are same in the SOLPS-ITER and the SD1D, including both atomic and molecular processes (all based on the Amjuel database). Since there are no drift effects in a 1D code, the SOLPS-ITER is run with drifts turned off. All radial diffusivities are $1\mathrm{m}^2\mathrm{s}^{-1}$ in the SOLPS-ITER code. The input power across the core-facing flux surface is set to 2.5MW, while the radial SOL widths are $\lambda_q = 6\mathrm{mm}$, $\lambda_n = 17\mathrm{mm}$ and $\lambda_{T_e} = 24\mathrm{mm}$. The corresponding input power flux for SD1D simulations is set to 70MW. In SOLPS-ITER simulations, the strength of the $\mathrm{D_2}$ puff at the inner mid-plane is varied in order to achieve an upstream density scan, which is from $0.5 \times 10^{19}\mathrm{m}^{-3}$ to $2.5 \times 10^{19}\mathrm{m}^{-3}$. An identical upstream density scan is carried out in SD1D simulations. Intrinsic impurity (carbon) is considered in both SOLPS-ITER and SD1D simulations, with a chemical sputtering yield of 3% in SOLPS-ITER code and a fixed carbon concentration of 3% in SD1D code. There are no extrinsic impurities in these simulations. The recycling rate is fixed to 99%.

We analyse the third flux tube of the Super-X grids in the SOLPS-ITER code, for which the target heat flux density is maximum in the attached regime. The corresponding connection length from X-point to the target is set to 20m in SD1D simulations.

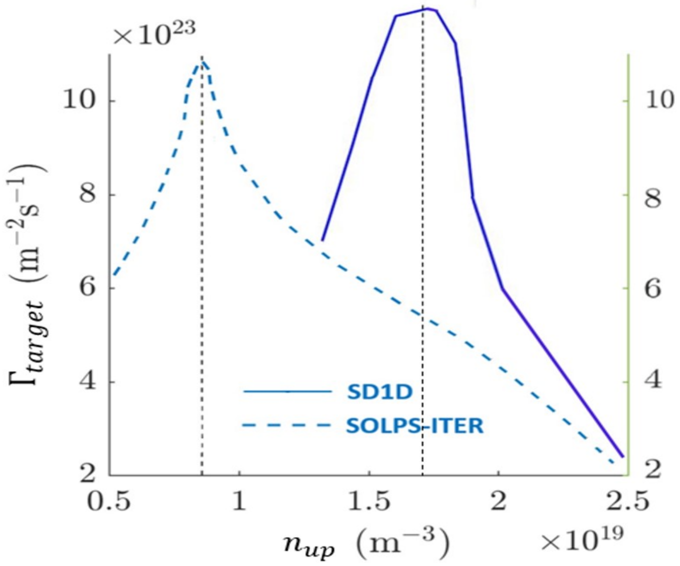

Figure 4.11: Parallel plasma flux density at the target along the 3rd flux tube in the Super-X grid, as a function of the upstream density (dashed line obtained by SOLPS-ITER). Comparison to the upgraded SD1D results (solid line) is also shown.

In figure 4.11, SOLPS-ITER results show that the target plasma flux quickly ramps up at the beginning of upstream density scan, then rolls over at about $0.85 \times 10^{19}\mathrm{m}^{-3}$ and fast decreases after rollover. A similar variation of target plasma flux in the density scan can be found in SD1D results, but a higher upstream density (about $1.7 \times 10^{19}\mathrm{m}^{-3}$) is needed to achieve target flux rollover, while the peak value of target flux is also higher. The cross-field transport and the difference of recycling conditions in 1D and 2D simulations are probably the main reasons of causing this difference. The comparison between the SOLPS-ITER and another 1D code (the Div1D) also finds the cross-field transport leads to big differences between a 1D and a 2D code [144]. In SD1D results, all recycled ions are converted into neutral molecules at the target, while in SOLPS-ITER simulations the particle reflection rate for neutral atoms and molecules is determined by the TRIM database. As a result, more neutral atoms can be obtained by recycling at the target in SOLPS-ITER cases, which are more effective for causing plasma energy loss (discussed in figure 4.1 and in section 4.5.2). Additionally, SOLPS-ITER simulations include recycling process on the wall, which is caused by the radial transport of plasma ions, thus interactions with neutrals are stronger such that it can further reduce threshold of achieving detachment onset.

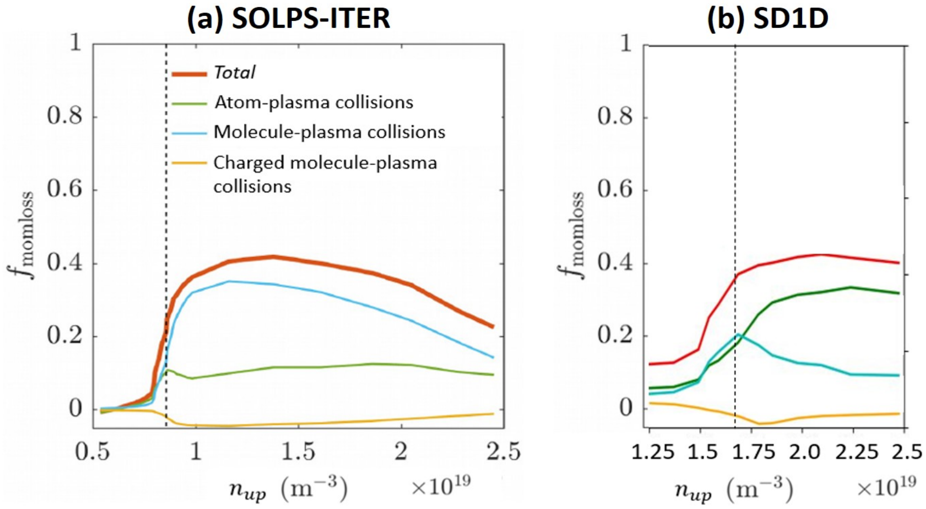

Figure 4.12: Decomposition of $f_{momloss}$ due to different reactions types, including atom-plasma collisions, molecule-plasma collisions and charged molecule-plasma collisions, obtained by (a) SOLPS-ITER and (b) SD1D.

In the SD1D and the SOLPS-ITER code, the same atomic and molecular processes are considered, including atom-plasma collisions (elastic collision, ionisation, recombination, charge exchange and dissociation), molecule-plasma collisions (elastic collision, non-dissociative ionisation and molecular charge exchange) and charged molecule-plasma collisions (dissociative ionisation, dissociative excitation, dissociative recombination,). The plasma momentum loss caused by different reaction types has been studied using the two codes, which are compared in figure 4.12. We can find that a similar variation of total momentum loss factor caused by the all collisions (red line) can be found in figure 4.12(a) and figure 4.12(b), which shows that the total momentum loss rapidly increases at around the rollover and then decreases a little after reaching the peak ($f^{peak}_{momloss,tot}$ is about 0.4). The momentum loss caused by charged molecule-plasma collisions also varies similarly in the two code's results.

The main difference between the results in figure 4.12(a) and figure 4.12(b) is that molecule-plasma collisions are the main plasma momentum loss factor in SOLPS-ITER simulations, while in SD1D results both atom and molecule play a crucial role at around the rollover and then after the rollover atom-plasma collisions become the dominant momentum loss in deep detachment. The main reason is that the dissociation of neutral molecules produces a large amount of neutral atoms in front of the target in the detachment cases, but the cross-field transport of neutrals in SOLPS-ITER simulations is able to mitigate the fast density ramp-up of neutral atoms (which can be found in SD1D simulations) and obtain a lower peak atom density in SOLPS-ITER simulations. Thus comparing to a 2D or 3D code, a 1D code (e.g. SD1D) without the effects of cross-field transport may overestimate the importance of atom-plasma collisions, especially in deep detachment cases.

4.7 Conclusions

First we implemented a comparison of the target plasma rollover and target temperature in the three recycling regimes:

(1) only neutral atoms produced by recycling ($H^+ \rightarrow H$)

(2) only neutral molecules produced by recycling ($H^+ \rightarrow H_2$)

(3) recycled atoms or recycled molecules with equal probability
(50% $H^+ \rightarrow H$ &50% $H^+ \rightarrow H_2$)

It is found that molecules play an important role in the flux rollover, which occurs at a higher upstream density and a slightly lower target temperature if a larger proportion of H_2 produced by the recycling process. It indicates that using the target material that produces more recycled atoms may reduce the requirement of achieving divertor detachment.

Generally the target flux rollover, indicating onset of detachment, occurs when a critical value of the gradient ofE_{ion} with respect to T_{target} is achieved: $\frac{\partial\, E_{\mathrm{ion}}}{\partial\, T_t} < -\gamma$

[68][19][36]. In this work the sheath transmission coefficient γ equals 6, thus the target electron temperature at rollover is found that $T_t = 5.6$eV and the corresponding effective ionisation energy E_{ion} is 82.23eV. In the simulations, we also calculated the momentum loss factor $f_m = 1 - 2p_{target}/p_{up}$ and obtained $\frac{2p_{target}}{p_{up}}$ as a function of target temperature: $\frac{2p_{target}}{p_{up}} = 1 - f_m = 0.889\left[1 - e^{(-\frac{T_{target}}{2.62})}\right]^{1.65}$. This corresponds to the value of the critical detachment parameter (equation 4.6) given as $\frac{p_{up}}{P_{recl}} = 8.1$ N/MW which is smaller than the value found by the previous version of SD1D [36].

The density profile of neutral atoms and neutral molecules determines the source of the main ion and charged molecules. With increasing upstream density, the source of main ions moves towards the target, while the source of charged molecule remains localised in a narrow region in front of the target. Corresponding to ionisation source, the radiation power profile of the direct excitation channel is the dominant excitation channel moving towards X-point during the density ramp, while the molecular excitation channels corresponding to the plasma-molecule reactions remain located in front of the target during detachment. It indicates that molecular species, which concentrate near the target, determine the plasma and neutral profiles in front of the target during detachment and thus play a crucial role in the target performance.

SD1D simulations predict that both molecule–plasma and atom–plasma collisions account for the rise of plasma momentum loss at the beginning of detachment. The part of total moment loss attributing to plasma-molecule collisions is larger compared to the momentum loss by plasma-atom collisions, primarily due to the molecule density larger than atom density at around the flux rollover. The decomposition of plasma-molecule collisions shows that the momentum loss mechanism via plasma-molecule interactions is primarily due to plasma-molecule elastic collisions, not molecular charge exchange, during the upstream density scan from attachment to detachment. The main reason is that rate coefficient of plasma-molecule elastic is much higher than the rate coefficient of molecular charge exchange when $T_e < 10$eV.

H_{alpha} emission is also considered in SD1D simulations, which found a strong rise of H_{alpha} signal when the upstream density is increased after rollover. The H_2^+ channel accounts for the most growth of H_{alpha} at the onset of detachment and then the H^- channel contributes more when the target becomes further detached [145][146][147]. In deuterium or tritium operation, the peak electron density and neutral density might become higher in the divertor [145]. Divertor detachment is expected to be started at a higher target temperature and a lower upstream density, due to the injection of strongly radiating impurity species [68][146]. SD1D has a wide applicability, and is able to simulate divertor detachment in different plasma conditions and in different divertor configurations. In future studies, it will be interesting to investigate the effects of molecular species on divertor detachment in other divertor configurations. Another interesting avenue is to investigate the effect of mass rescaling on divertor detachment.

Chapter 5

Comparison of divertor detachment achieved by density ramp and neon seeding

Divertor detachment can be driven by either an increase in the hydrogen plasma density via core fuelling or divertor gas puff, or via seeding of neon impurities. We implemented code upgrades in SD1D by adding a impurity (neon) model in the physical model (section 3.5), such that the new SD1D can be used to model atomic and molecular processes during ether upstream density ramp or neon seeding. This chapter presents simulation results which investigate divertor detachment induced by a density ramp and neon impurity seeding. In the following content, the motivation for doing this work is presented in section 5.1; the initial parameters are given in section 5.2; differences in atomic and molecular processes during the two detachment regimes are presented in section 5.3; and finally the parallel transport of neon impurities is discussed in section 5.4. The simulations in this chapter are mainly carried out using the new SD1D with impurity dynamics (see section 3.5.1).

5.1 Motivation

Apart from increasing upstream density, seeding impurity in divertor is another effective way to achieve divertor detachment (section 2.2.5). In recent experiments in MAST-U tokamak [148][149], valves for seeding impurity gas have been installed in the Super-X divertor volume (e.g. the position in front of the target). Helium impurity seeding has been planned in the second MAST-U campaign (with relatively low input powers) for reducing heat load in the divertor. However it will not be enough when the double beam box is installed and more NBH (Neutral Beam Heating) power is available in future experiments. In this situation the impurity leading to a higher radiation power loss will be used. As discussed in section 2.2.5, noble gases (e.g. neon) are the main candidates for this task since the radiative properties of noble gasses are close to those of carbon, with a high radiative efficiency for the range of temperature typically encountered in the divertor region, yet remaining relatively low in the plasma core [65].

In order to achieve divertor detachment by neon impurity seeding in the MAST-U conditions, it is crucial to understand the transport of neon impurity and the role of atomic and molecular processes during impurity seeding. Therefore implementing a scan of upstream density and impurity seeding rate respectively from the same steady state to detached cases can be helpful for understanding the mechanism by which the two approaches achieve detachment.

5.2 Setup and initial parameters

The SD1D code (section 3.5) numerically solves the equations for the main plasma ions, hydrogen atoms, hydrogen molecules, hydrogen charged molecules, neutral neon atoms and neon ions at all charge states. In this work, divertor detachment is achieved by two approaches: a density ramp and neon impurity seeding. The initial parameters in the two cases are detailed below:

Upstream density ramp

The MAST-U Super-X divertor conditions are also used for the simulations in this Chapter. The initial parameters related to hydrogenic species are the same as the parameters listed in section 3.5, including (1) the parallel heat flux at the X-point ($50MW/m^2$), (2) connection length of 30m (containing 20 m from X-point to target), (3) area expansion factor of 2 between X-point and the target, (4) 99% of plasma ion flux arriving at the target is recycled into neutrals, and (5) the scan of upstream density is from $1.65\times10^{19}\mathrm{m}^{-3}$ to $4.0\times10^{19}\mathrm{m}^{-3}$. However in this chapter it is assumed that the recycling produces just molecules as the recycling output in the following content.In this density ramp scan, there is no neon considered in the simulations.

Therefore there is no effect of neon impurity.

Impurity seeding rate scan

In order to compare the two detachment approaches, the initial parameters related to hydrogenic species are all the same as the case of density ramp scan presented above (except upstream density which is not varied). In terms of neon impurity, the initial parameters are listed below:

(1) The steady state with only hydrogenic species (the upstream density equals $1.65 \times 10^{19}\mathrm{m}^{-3}$ to $4.0 \times 10^{19}\mathrm{m}^{-3}$ in the density ramp case) is used as the initial state before impurity seeding.

(2) Neutral neon is injected in front of the target (located at 30m in figure 5.1) as an exponential distribution (shown in section 3.5.1). To achieve the injection rate scan, different peak injection flux $\Gamma_{peak,\ \mathrm{Ne}^{0+}}$ is used in simulations. $\Gamma_{peak,\ \mathrm{Ne}^{0+}}$ is varied from 0.1×10^{20} to 13×10^{20} [particles/m^2/s]. The figure 5.1 shows the neon injection flux profile for the case of attachment, rollover and detachment respectively. The corresponding neon seeding rate is from 0.14×10^{20} [particles/s] to 1.81×10^{21} [particles/s], which will be shown in the following figures. The peak of the flux profile is located at the target $\theta_{1/2} = \theta_{target} = 2\pi$ and parallel injection flux width $w_{flux} = 0$ The parallel profile of neon injection flux is shown below, including a case of attachment, a case around flux rollover, and a case of detachment.

(3) The electron-impact reactions and charge exchange reactions are considered as the sinks/sources in the density and energy equations and as the force in the momentum equation. The reactions include:

Ionisation (from Ne^{0+} to Ne^{9+}): $\mathrm{Ne}^{Z+} + e \rightarrow\ \mathrm{Ne}^{Z+1} + 2e$

Recombination (from Ne^{+} to Ne^{10+}): $\mathrm{Ne}^{Z+} + e \rightarrow\ \mathrm{Ne}^{Z-1}$

Charge exchange (from Ne^{+} to Ne^{10+}): $\mathrm{Ne}^{Z+} + \mathrm{H} \rightarrow \mathrm{Ne}^{\mathrm{Z}-1} + \mathrm{H}^{+}$

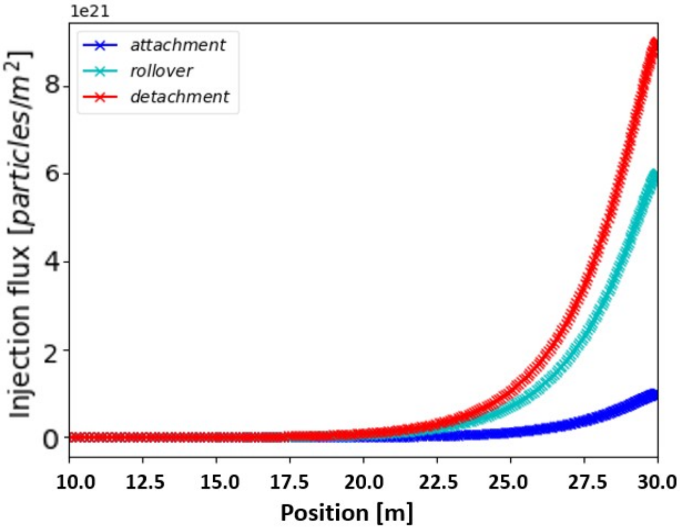

Figure 5.1: The profile of neon injection flux in three cases: attachment ($\Gamma_{peak,\ \mathrm{Ne}^{0+}} = 1.0 \times 10^{20}$ [particles/m^2/s]), rollover ($\Gamma_{peak,\ \mathrm{Ne}^{0+}} = 6.0 \times 10^{20}$ [particles/m^2/s]) and detachment ($\Gamma_{peak,\ \mathrm{Ne}^{0+}} = 9.0 \times 10^{20}$ [particles/m^2/s]).

5.3 The role of plasma-atom and plasma-molecule interactions during detachment – differences between density ramp and impurity seeding

5.3.1 The plasma ion flux and temperature at the target

Detachment induced by density ramp – Testing the trace assumption

The simulations in Chapter 4 are based on a trace assumption for H_2^+. However this assumption will not be applicable if a non-negligible amount of impurities are considered in the simulations (e.g. neon seeding in this section). This is due to the extra electrons produced from the plasma-impurity interactions and thus the density of electron and the main plasma ion will be different in this case. Here it is assumed that $n_e = n_{\mathrm{H}^+} + n_{\mathrm{H}_2^+} + \sum_{Z=0}^{10} Z n_{\mathrm{Ne}^{Z+}}$. This section starts with a comparison between the model with trace assumption and without trace assumption for H_2^+. As figure 5.2 shows, the result of upstream density scan for the target plasma flux and the target temperature is similar in the two cases. The simulation shows that trace assumption for H_2^+ does not greatly change the important results, such as the rollover of target flux and the reduction of target temperature. This is primarily due to the small portion of H_2^+ in the divertor. The ratio of $\frac{N_{H_2^+}}{N_{H_2^+} + N_{H+}}$ is just about 0.022 when electron temperature is lower than 7eV. The electron density is still approximately equal to the main plasma ion density. However if the molecule density greatly increases in the divertor due to either external fueling or a stronger recycling process for neutral molecules, the density H_2^+ may quickly increase and therefore this assumption will not be valid any more.

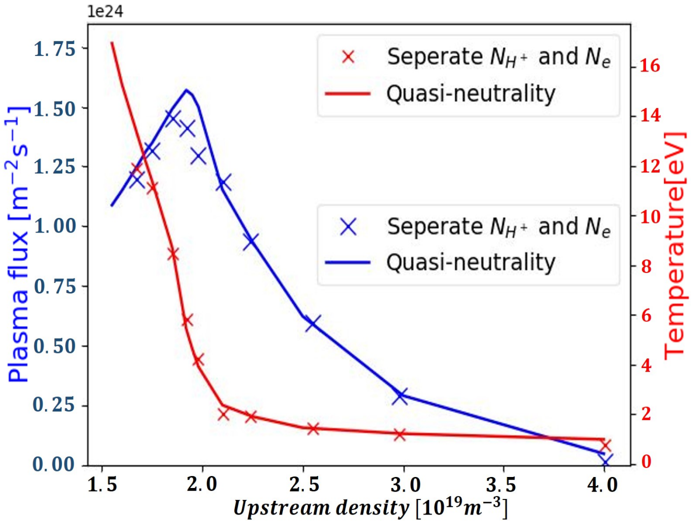

Figure 5.2: A upstream density scan for plasma ion flux and electron temperature at the target in the case with and without trace assumption.

Detachment induced by neon seeding

To make the two approaches comparable, the attached case with upstream density $1.65 \times 10^{19} \text{m}^{-3}$ in the density ramp scan is used as the initial state before impurity seeding. Based on this initial state, cases with different neon seeding rates from 0.14×10^{20} [particles/s] to 1.81×10^{20} [particles/s] are simulated and eventually reach a steady-state solution. Thus a scan of the neon seeding rate for the target plasma flux and target temperature can be made as shown in figure 5.3. It is found that increasing neon seeding rate can effectively reduce the target temperature and a rollover of target plasma flux is achieved at a seeding rate between 2.5×10^{20} [particles/s] and 5.0×10^{20} [particles/s]. The target flux rollover occurs when the target temperature is about 6eV, slightly higher than the required temperature (about 5eV) for rollover in the density ramp cases. Another difference is that the target temperature cannot be further reduced by a larger seeding rate when it drops to about 2.8eV, while the target plasma flux can still be effectively reduced.

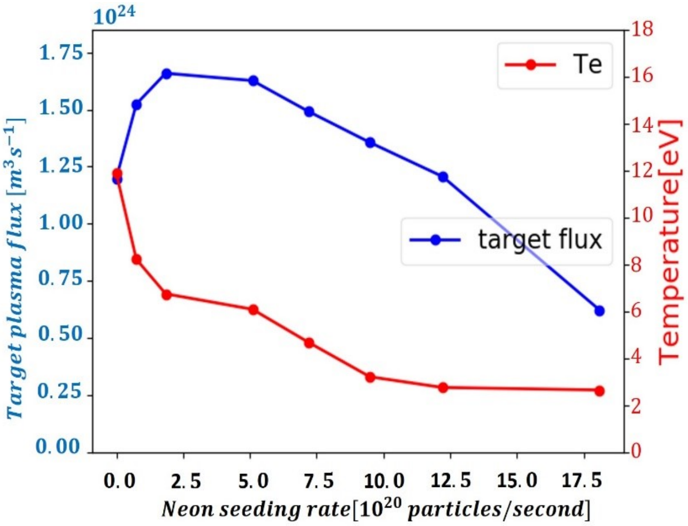

Figure 5.3: A neon seeding rate scan for plasma ion flux and electron temperature. The upstream density is fixed at $1.65 \times 10^{19}\text{m}^{-3}$

According to studies of the particle, momentum and power balance in the divertor [19][4][35], the target flux can be reduced through three ways:

(1) Reducing the heat flux entering the recycling region (e.g. though impurity radiation);

(2) Increasing the energy cost of ionisation (e.g. through upstream density ramp);

(3) Reducing the ion density in the divertor (e.g. through volumetric recombination).

During a neon seeding rate scan the radiation power loss increases primarily in the high temperature region (around 20eV, see figure 2.9) such that the heat flux can be effectively reduced by neon impurity radiation before entering the recycling region (see figure 5.5). Although the ionisation and recombination (see figure 5.7(b)) do not become more intensive at higher seeding rates, neon impurity radiation (see figure 5.9(b)) is powerful enough to achieve rollover of the target flux and even achieve a deeper detachment phase. The different energy costs of ionisation in the two detachment regimes may be the main reason that causes the different minimum target temperature in the two detachment regimes. This will be studied in more detail in next section.

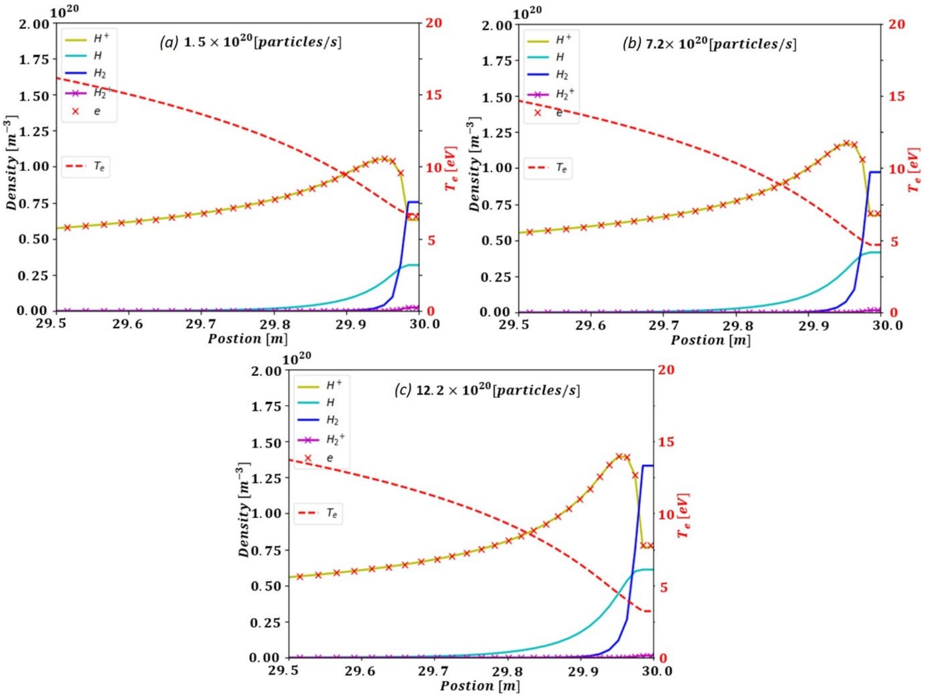

Figure 5.4: Density profile of H^+, H, H_2 and H_2^+, and the profile of electron density and temperature in the case of neon seeding rate (a) 1.5×10^{20} [particles/s], (b) 7.2×10^{20} [particles/s] and (c) 12.2×10^{20} [particles/s]. The upstream density is fixed at $1.65 \times 10^{19}\mathrm{m}^{-3}$. The target is located at 30m.

In figure 5.4, the parallel density profile of hydrogenic species gradually increases in the cases with a higher seeding rate, but the increase is not as sharp as the increase during the density ramp. It is mainly due to the plasma ion flux entering the recycling region, which changes little during impurity seeding. The recycling process at the target cannot produce a large neutral flux even using a high impurity seeding rate. Additionally the ideal temperature for hydrogenic reactions like recombination and molecular activated recombination (MAR) is generally lower than 2.8eV (the minimum target temperature achieved in figure 5.3). Thus fewer neutrals are produced by recycling and recombination near the target compared to the density ramp cases which has a larger ion flux flowing into the recycling region. The effect of some hydrogen atomic and molecular processes during neon seeding may be not as crucial as their effect is during density ramp detachment. The following sections will further discuss the role of atomic and molecular processes during the two detachment regimes.

5.3.2 Comparison of the plasma-atom and plasma-molecule interactions during detachment induced by density ramp and neon seeding

The profile of sink and source of the main plasma ion H^+ and charged molecule H_2^+ during a density ramp has been discussed in Chapter 4. That chapter primarily investigates the region of sinks and sources in the direction parallel to the magnetic field. In this section, a comparison is carried out to study the role of atomic and molecular processes in the particle, power and momentum balance of the two detachment regimes: density-ramp and impurity-seeded.

Parallel heat flux and pressure profile

The parallel heat flux and pressure profile are directly related to the power and momentum balance in the parallel direction. In the simulations, it is assumed that the recycled neutral flux is produced at the target (section 3.4.2), thus the plasma and the neutral density profile increase in a relatively small region in front of the target. The kinetic convection of heat therefore only affects the small ionisation region near the target. If the recycled neutrals are redistributed evenly along the parallel direction, the kinetic convection may become stronger in the region away from the target. Although the heat flux arriving at the target may also be affected by the convection of the charged molecules and neon ions, their convection is small compared to the heat conduction and the main plasma flux in the simulations.

Two cases of neon seeding (figure 5.5(a) and figure 5.5(b)) and two cases of density ramp scan (figure 5.5(c) and figure 5.5(d)) are studied in this section. It is found that

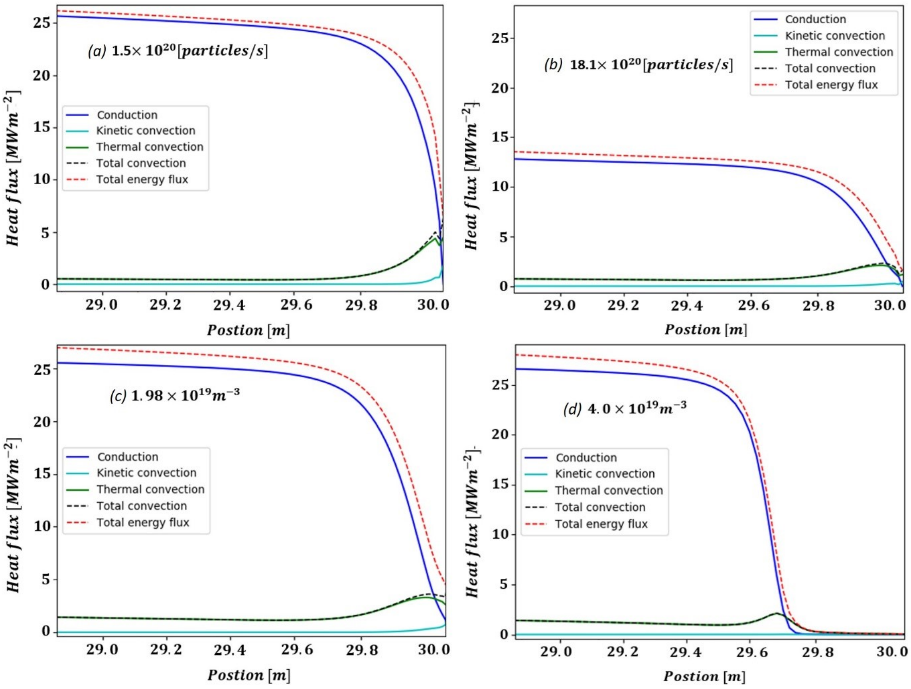

Figure 5.5: Decomposition of heat flux profile in the case of neon seeding rate (a) 1.5×10^{20} [particles/s] and (b) 18.1×10^{20} [particles/s], and in the case of upstream density ramp (c) $1.98 \times 10^{19}\mathrm{m}^{-3}$ and (d) $4.0 \times 10^{19}\mathrm{m}^{-3}$. The upstream density is fixed at $1.65 \times 10^{19}\mathrm{m}^{-3}$ for the cases of neon seeding. The target is located at 30m.

the heat flux is effectively reduced by neon impurity radiation before it approaches the target (The neon radiation profile is discussed in figure 5.13 in next section), while in the density scan the heat flux mainly decreases in the narrow recycling region in front of the target. One thing needs to be noted that the heat flux is about $25\mathrm{MWm}^{-2}$ at 29m if the volumetric power loss mainly occurs near the target, since the flux expansion factor equals 2 (input heat flux at X-point is $50\mathrm{MWm}^{-2}$ for all cases).

Figure 5.6 shows the plasma pressure profile in the cases of attachment and detachment. Similar to the heat flux profile, figure 5.6(a) shows that the plasma pressure can be effectively reduced by a higher neon seeding rate in the region apart from the target, while in figure 5.6(b) it decreases in the narrow recycling region in front of the target and the plasma pressure profile can be largely increased by a larger upstream density (in the region in front of 29.6m). Although the plasma pressure is approximately constant from the recycling region to X-point, the plasma pressure at 29m is smaller than the pressure at the X-point due to the effect of neon radiation power loss.

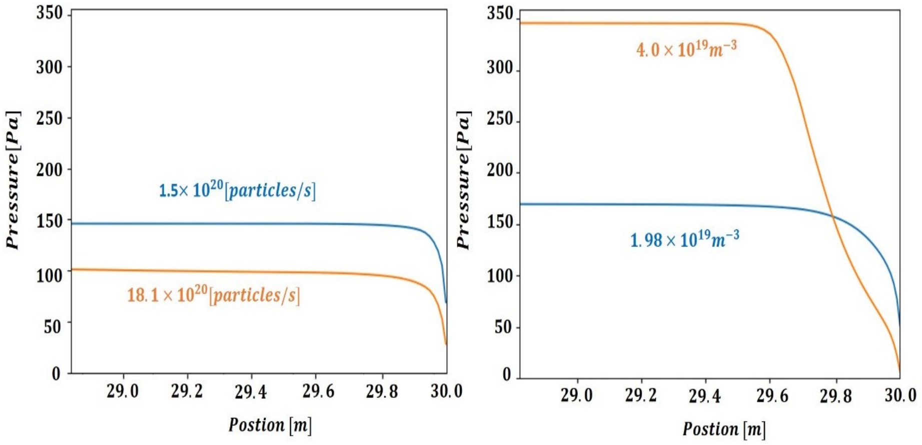

Figure 5.6: Plasma pressure profile in the case of neon seeding rate 1.5×10^{20} [particles/s] and 18.1×10^{20} [particles/s] (left), and in the case of upstream density ramp $1.98 \times 10^{19}\text{m}^{-3}$ and $4.0 \times 10^{19}\text{m}^{-3}$ (right). The upstream density is fixed at $1.65 \times 10^{19}\text{m}^{-3}$ for the cases of neon seeding. The target is located at 30m.

The sources/sinks of H^+ and H_2^+ during a density ramp and a neon seeding

Divertor particle balance is related to the sources and sinks of the main plasma ion (H^+, which are determined by the plasma-atom and the plasma-molecule interactions in the divertor. In the SD1D simulations, the source includes ionisation, dissociative ionisation (DI) and dissociative excitation (DE), while the sink includes electron-impact recombination (EIR), molecular charge exchange and molecular activated recombination (MAR) (see table 3.1). Figure 5.7 shows the decomposition of H^+ sink and source in the scan of (a) upstream density and (b) neon impurity seeding rate. It is found that ionisation is always the dominant particle source of the main ion in the two detachment regimes. In figure 5.7(a), a sharp increase of ionisation source can be found with the increase of upstream density and it eventually becomes double the source in the attached regime. The source produced by dissociative excitation is varies in a similar way to the ionisation source in the density ramp case. It increases quickly after rollover and eventually becomes a significant source in the deeply detached cases. In terms of the sinks, molecular charge exchange leads to most of the main ion particle loss, while electron-impact recombination and MAR are negligible at the beginning of the detachment and then gradually becomes important in the more deeply detached phase. The result indicates the plasma-molecule interactions can result in additional ion sources/sinks compared to just atomic processes. Both atomic and molecular reactions are crucial for the particle balance during the detachment induced by a density ramp.

During neon seeding (figure 5.7(b)) the ionisation source slightly increases with the enhancement of neon seeding rate and then slowly decreases after rollover. The dissociative excitation source becomes smaller at a higher neon seeding rate. compared to the density ramp case, the two ion sources (ionisation and molecular charge exchange) are all much smaller than the source in figure 5.7(a). The volumetric ion sink during neon seeding is tiny at the beginning of detachment, and even at high seeding rates only molecular change exchange contributes to a small part of the ion loss. It is primarily due to the minimum target temperature in the seeding rate scan is about 2.8eV, which is not the ideal temperature for the electron-impact recombination (< 1eV) and MAR (< 2.5eV).

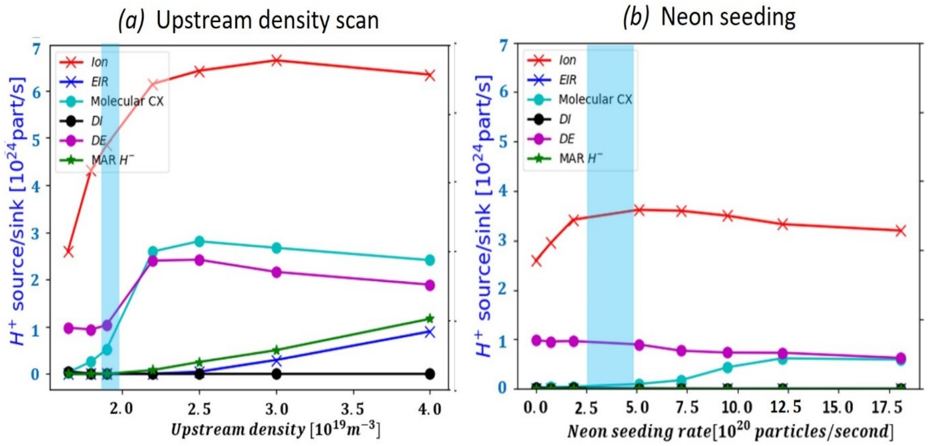

Figure 5.7: (a) The upstream density scan and (b) the neon seeding rate scan for plasma ion sources/sinks. The vertical blue column represents the rollover of target ion flux.

The main reason for the relatively high target temperatures in the seeded cases may be the different intensity of ionisation in the two detachment regimes. According to Two Point Model(see section 2.3.1), the heat flux arriving the target is $q_t = \gamma n_t T_t c_s$

where n_t and T_t are the plasma density and temperature at the target. The sound speed of ion is $c_s = \sqrt{\frac{2T_t}{m_{\mathrm{H}+}}}$. Thus the heat flux at the target is $q_t = \gamma p_t \sqrt{\frac{2T_t}{m_{\mathrm{H}+}}}$ and the target temperature can be written as:

$$T_t = \frac{2m_{\mathrm{H}+}}{\gamma^2} \left(\frac{q_t}{p_t} \right)^2 \tag{5.1}$$

Since the sheath transmission coefficient $\gamma = 6$ in simulations (section 3.2.2), the target temperature is determined by the ratio of the heat flux and plasma pressure at the target. According to two point model (section 2.3.2) the heat flux and plasma pressure at the target are affected by volumetric power loss and volumetric momentum loss respectively, thus equation 5.1 indicates that

(1) Volumetric power loss strongly decreases the target temperature;

(2) Volumetric momentum loss strongly increases the target temperature.

During the density ramp, a high recycling regime occurs and produces a high neutral density near the target, which can effectively reduce the volumetric plasma momentum. However increasing upstream density can increase the initial plasma pressure at upstream (in figure 5.6(b)), which increases up to 348Pa ($n_{up} = 4.0 \times 10^{19}/\mathrm{m}^3$) in simulations. As a result, the plasma-neutral interaction becomes more intensive at higher upstream densities, but about 10% of plasma ion momentum can still reach the target in the case of $n_{up} = 4.0 \times 10^{19}/\mathrm{m}^3$ (the corresponding plasma pressure at the target is about 17Pa).

As discussed in figure 5.4, the recycling process during neon seeding is relatively weak and cannot produce a large density of neutrals near the target, therefore the plasma-neutral interaction in this case cannot effectively reduce the volumetric plasma momentum. However in figure 5.6(a) increasing neon seeding can effectively decrease the plasma pressure apart from the target, which can be significantly enhanced by increasing upstream density (figure 5.6(b)). Thus we can still achieve a small plasma pressure at the target during the scan of neon seeding rate. As shown in figure 5.6

(a), the plasma pressure at the target is about 28Pa at the highest neon seeding rate 1.81×10^{21} [particles/s], which corresponds to a smaller volumetric momentum loss ($< 60\%$)

According to the volumetric power loss in figure 5.6, the heat flux entering the target is just about 0.3 MW/m^{2}in the case with a high upstream density ($n_{up} = 4.0 \times 10^{19}/\text{m}^3$) and it is about 2.0 MW/m^2 in the case with the highest neon seeding rate 1.81×10^{21} [particles/s]. Thus with the same input heat flux at X-point 50 MW/m^2 in the simulations, the upstream density scan achieves a lower heat flux compared to the scan of neon seeding rate. The reason is: (1) The net hydrogen excitation radiation power loss at high upstream density in figure 5.9(a) is close to the total radiation power loss at high seeding rate in figure 5.9(b); (2) the ionisation source in figure 5.7(a) is much larger than the one in figure 5.7(b), thus the corresponding ionisation energy cost is also much higher in the case with the density ramp. Since hydrogen volumetric cooling process is related to power loss by ionisation energy cost and the net excitation radiation, the total volumetric power loss during the upstream density scan is higher than the seeding rate scan.

Putting the parameters ($p_{t,density\ ramp} = 17$Pa, $q_{t,density\ ramp} = 0.3$ MW/m^2 for the density ramp and the parameters ($p_{t,neon\ seeding} = 28$Pa, $q_{t,density\ ramp} = 2.0$ MW/m^2) for the neon seeding scan into equation 5.1, it is found that the density ramp can achieve a lower minimum target temperature than the neon seeding scan in our simulations. Summarily, it is mainly due to (1) the higher energy cost caused by the larger ionisation source (including net hydrogen excitation radiation power loss and ionisation energy cost) during the density ramp, which can further reduce the heat flux at the target, (2) both of the two approaches can achieve a low plasma pressure at the target.

Although a higher neon seeding rate can further reduce the heat flux, it will lead to some crucial problems such as the neon concentration in the core plasma larger than the fatal fraction [150]. The fatal fraction is the concentration above which the total core radiation is more than the sum of fusion and input power. It could be different in different devices. Additionally, all the volumetric power sinks (including ionisation in figure 5.7(b), hydrogen excitation radiation and impurity radiation in figure 5.9(b)) and volumetric momentum loss (plasma-neutral interactions in figure 5.10(b)) tend to be flat in the simulations. Thus as shown in figure 5.3 the target temperature changes little in the deep detachment phase ($> 1.0 \times 10^{21}$ [particles/s])

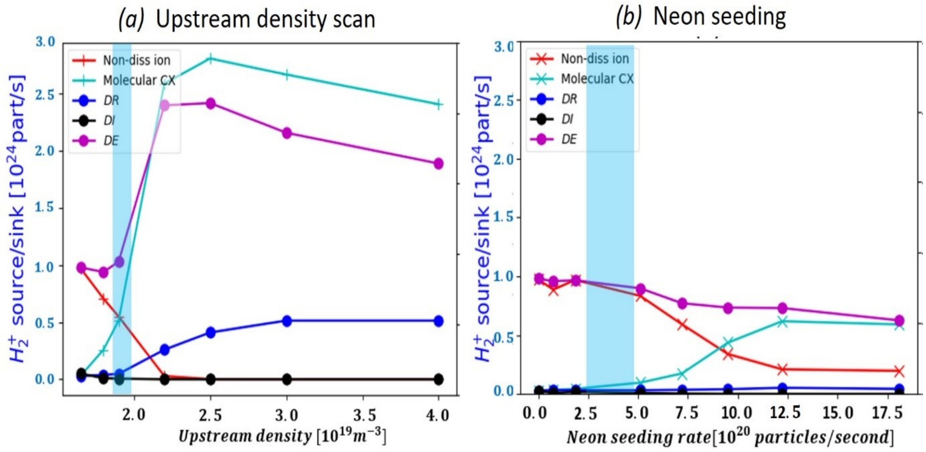

Figure 5.8: (a) The upstream density scan and (b) the neon seeding rate scan for H_2^+ sources. The vertical blue column represents the rollover of target ion flux.

The charged molecule H_2^+ play a crucial role during divertor detachment. It is involved in the plasma-molecule interactions such as molecular activated recombination (MAR)) and hydrogen excitation radiation, which significantly affect the particle balance and power balance during divertor detachment if low target temperature are achieved (< 2.5eV). Photon emission (e.g. H_{alpha} photon) in the divertor is also significantly affected by the dynamics of H_2^+, which is a crucial excitation channel to produce excited atoms. Therefore to understand the effect of the charged molecules in the two detachment regimes, it is essential to compare its sources and sinks using the scans in figure 5.8

The source of H_2^+ includes molecular charge exchange and non-dissociative ionisation and the sink includes dissociative ionisation (DI), dissociative excitation (DE) and dissociative recombination (DR), as shown in table 1. During a density ramp (figure 5.8(a)), non-dissociative ionisation is the dominant source for the charged molecule and DE is the main sink. With the increase of upstream density, the temperature in front of the target quickly drops to the ideal reaction temperature for molecular charge exchange to occur, which dramatically enhances and becomes the main source for the charged molecules during detachment. Since the rate coefficient of non-dissociative ionisation becomes tiny at low temperatures, it becomes less important with the decrease of target temperature. The crossover of the two sources in figure 5.8(a) occurs around rollover (where the electron temperature is about 5eV). It corresponds to the crossover of rate coefficients of the two reactions which also occurs at about 5eV in figure 2.2 in section 2.2.2.

In figure 5.8(b), the crossover of the two charged molecule sources (non-dissociative ionisation and molecular charge exchange) occurs after rollover. It is primarily due to the relatively higher target temperature (about 6eV) that is required to achieve detachment during neon seeding (discussed in figure 5.3). Since neutral molecule density cannot be effectively enhanced by recycling in the seeding ramp, the sources of the charged molecule is much smaller than its sources in density ramp cases and thus the sinks are smaller as well. As a result, the simulations predicts that the role of charged molecules may be more important during detachment induced by density ramp than in neon seeded cases. The following discussion of radiation power loss, volumetric momentum loss and H_{alpha} photon emission will further confirm this prediction.

The radiative power loss

Radiative power loss significantly influences the divertor power balance. Hydrogen excitation radiation plays an important role in the power loss in both density ramp cases and neon seeding cases.

Figure 5.9(a) shows that radiation loss through direct excitation ('H') is the main hydrogenic radiation channel in the density ramp, contributing about 80% of total hydrogenic radiation loss in deep detachment. The other channels like recombination ('H^+'), dissociative recombination ('H_2^+') and mutual neutralization ('H^-') are negligible at the beginning of the density ramp and slowly increase at high upstream

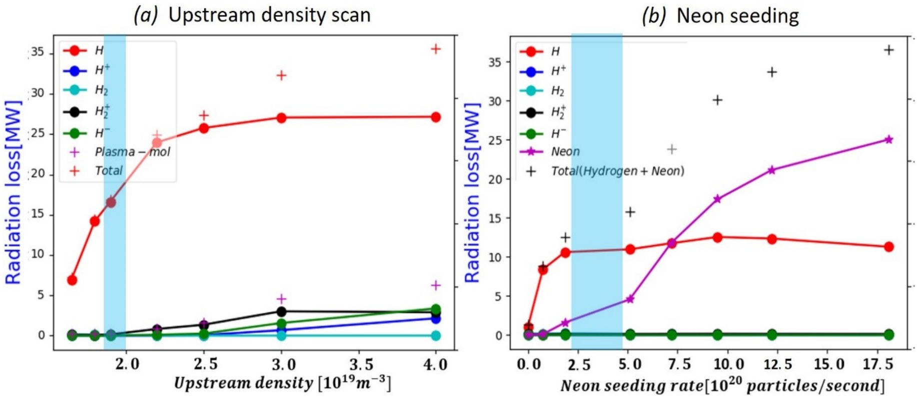

Figure 5.9: (a) The upstream density scan and (b) the neon seeding rate scan for H_2^+ sinks. The vertical blue column represents the rollover of target ion flux.

densities. The molecular excitation channels ('H_2^+' and 'H^-') contributes 20% of the total radiation power of hydrogen. It can be more if an external neutral source (e.g. gas puffing) is used in the divertor. If cross-field transport is considered (as in 2D modelling with e.g. SOLPS), the radiation loss produced by excited atoms after molecular break-up (e.g. 'H_2', 'H_2^+' and 'H^-' channels) may become larger than in a 1D case.

In figure 5.9(b), the direct excitation radiation is also the dominant hydrogenic radiation, but it is much lower than the result in density ramp cases since fewer neutrals (hydrogenic atoms or molecules) can be produced by recycling or recombination during neon seeding. The rest of the radiation channels (including recombination and all the molecular channels) are negligible during the seeding rate scan, since the relatively higher target temperature discussed above leads to a small reaction rate for these loss channels. With the increase of seeding rate, neon impurity radiation power loss quickly increases and thus makes up the difference of radiation power loss to achieve a deep detachment phase.

The volumetric momentum loss

Figure 5.10(a) investigates the decomposition of volumetric momentum loss in the diveror induced by plasma-atom collisions, plasma-molecule collisions and colli-

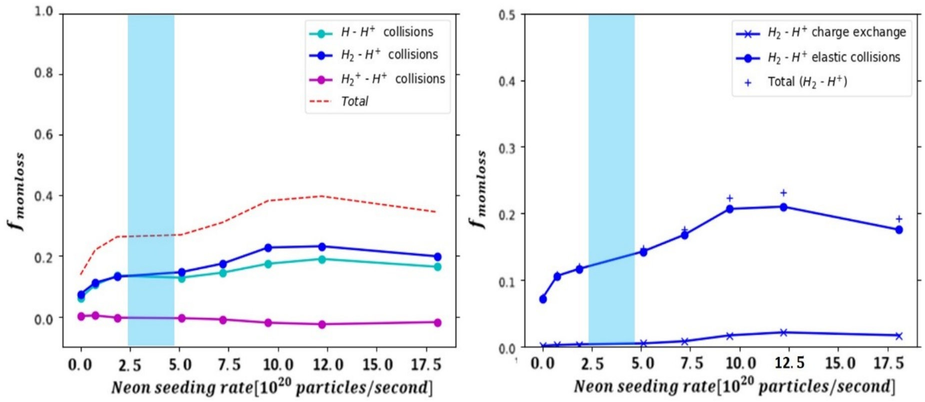

Figure 5.10: The neon seeding rate scan for the momentum loss factor $f_{momloss}$ caused by plasma-atom and plasma-molecule collsions (left); Decompositon of the $f_{momloss}$ caused by plasma-molecule collisions, including elastic collsion and charge exchange (right). The vertical blue column represents the rollover of target ion flux.

sions between plasma main ions and charged molecules. Similar to the density ramp cases (see section 4.5.3), plasma-molecule collisions (including molecular charge exchange and plasma-molecule elastic collision) are as essential as the plasma-atom collisions in this scan. Due to the small charged molecule density, collisions with plasma cannot significantly affect the divertor momentum balance. In figure 5.10(b), plasma-molecule collisions are primarily due to molecular elastic collisions instead of molecular charge exchange. The difference between the two detachment regimes is that:

(1) During the density ramp a much stronger rise of momentum loss can be found near rollover;

(2) During the density ramp the momentum loss factor (up to about 50%, see section 4.5.3) is generally higher than the loss during neon seeding (about 27% after rollover and then slowly increasing to just 40% in the deep detachment phase).

Based on the Two Point Model, volumetric momentum loss is a crucial factor to reduce the target ion flux $\Gamma_t \propto \frac{(1-f_{\text{mom}})^2(1-f_{\text{conv}})^{4/7}}{(1-f_{\text{pow}})^2}$ where the convection factor does not significantly affect the target temperature). It is mainly caused by the ion-atom and the ion-molecule collisions. Compared to the density ramp, neon seeding is unable to greatly raise the particle densities (of both neutrals and plasma), such that the ion-neutral collision in this situation cannot be as strong as the density ramp cases. As discussed above, the volumetric momentum loss factor during the density ramp is generally higher than the loss during the seeding rate scan. Therefore in order to reduce the target ion flux, volumetric momentum loss is more important in the density ramp cases than the momentum loss in neon seeding cases (which mainly depends on the strength of the volumetric power loss).

H_{alpha} **photon emission**

As discussed in section 4.5.3, H_{alpha} emission is crucial for divertor research since it conveys information on neutral density and neutral-plasma interactions, which significantly affect the particle, momentum and power balance in the divertor. In this work, SD1D models the H_{alpha} emission during the scan of neon seeding rate. It predicts that direct electron-impact excitation 'H' dominates H_{alpha} emission and it changes little in the detachment phase, while the dissociative recombination 'H_2^+' is tiny until the seeding rate increasing up to about 1.2×10^{21} [particles/s] where H_{alpha} emission rate through H_2^+ channel reach the peak, but it is less than a quarter of the total H_{alpha} emission rate. Compared to the density ramp cases, neon seeding cannot achieve the strong rise of H_{alpha} emission rate that has been found during the density ramp (section 4.5.3), and the total H_{alpha} emission rate in figure 5.11 is much lower than the rate in the upstream density scan (about 4 times smaller).

Similar to the discussion of the other atomic and molecular processes above, the main reason causing the difference here is also about the different minimum target temperature and the different ion flux flowing into the recycling regime. The ideal temperature for the H_{alpha} emission through molecular channels is lower than 2.5eV (lower than the minimum temperature 2.8eV achieved in the neon seeding cases), and the recycling process in the neon seeding cases cannot provide more molecules at the target and thus cannot produce more excited hydrogen atoms through dissociative recombination (H_2^+) or dissociative excitation (H_2).

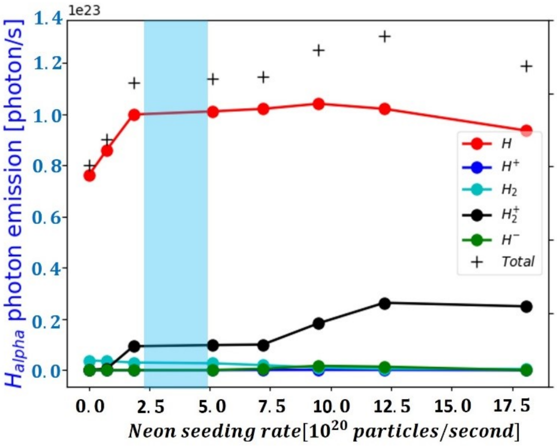

Figure 5.11: Decomposition of total $\mathrm{H_{alpha}}$ photon emission due to atomic channels (H and $\mathrm{H^+}$) and molecular channels ($\mathrm{H_2}$, $\mathrm{H_2^+}$ and $\mathrm{H^-}$), Vertical column indicates the rollover of target ion flux.

5.4 Parallel transport of neon impurity

Seeding impurity in the divertor is an effective way to achieve divertor detachment, which can effectively reduce the heat load on the target plates [64][151][66]. However the impurity transport in divertor leads to variations of impurity profiles, which tend to move towards the core plasma, such that the impurity radiation will impact the core plasma if the impurities move into the core plasma, and even damage the plasma confinement if the impurity concentration in the core plasma is larger than the fatal fraction [150]. Thus it requires a high concentration of neon in the divertor, but a low concentration in the core plasma/upstream plasma.

As discussed in figure 5.5 and figure 5.6, SD1D simulation results show that seeding impurity in the divertor can effectively reduce the heat flux and plasma pressure in a wide region in the divertor. To understand the mechanism of neon impurity transport in parallel direction, we investigated the effect of parallel force balance on the parallel profiles of neon impurities.

5.4.1 Neon concentration and neon radiation

Impurity radiation plays a crucial role in the divertor power balance. Three cases with different neon seeding rates discussed in section 5.3.2 are used for analysing the neon concentration and radiation power loss in the direction parallel to the magnetic

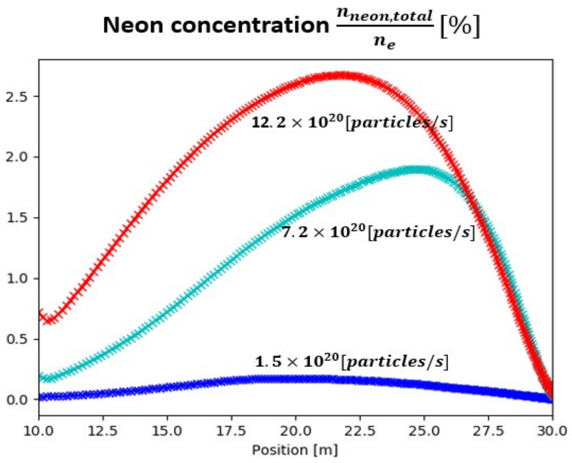

Figure 5.12: The profile of neon concentration in the case of neon seeding rate 1.5×10^{20} [particles/s], 7.2×10^{20} [particles/s] and 12.2×10^{20} [particles/s]. The upstream density is fixed at $1.65 \times 10^{19} \mathrm{m}^{-3}$. The target is located at 30m.

field. It includes (1) an attached case (seeding rate equals 1.5×10^{20}[particles/s]), (2) a case at the beginning of detachment (7.2×10^{20}[particles/s])) and (3) a deep detachment case (12.2×10^{20}[particles/s])). In figure 5.12, the parallel profile of neon concentration is defined by the ratio of total density of neon species (including all charge states) by the electron density. It is found that the peak of neon concentration is mainly located at the region away from the target in three cases. The front of the concentration profile upstream when the divertor transitions from attachment to detachment. The peak concentration and the concentration at the X-point quickly increase with the increase of seeding rate.

Compared to figure 5.13, the variation of neon radiation profile strongly corresponds to the variation of neon concentration. It shows that the peak radiation power is located at a similar region to the peak neon concentration, and the front of neon radiation power moves upstream with the increase of seeding rate. Since the peak radiation power is primarily determined by the main cooling species (e.g. $\mathrm{Ne}^{3+} - \mathrm{Ne}^{6+}$ shown in figure 5.14) the variation of neon radiation power reflects the changes of the cooling species such as the density and fraction abundance of different charge states.

Similar to the other impurities, there is a maximum seeding rate for neon in certain divertor conditions. If the seeding rate is higher than this limit, the neon impurity

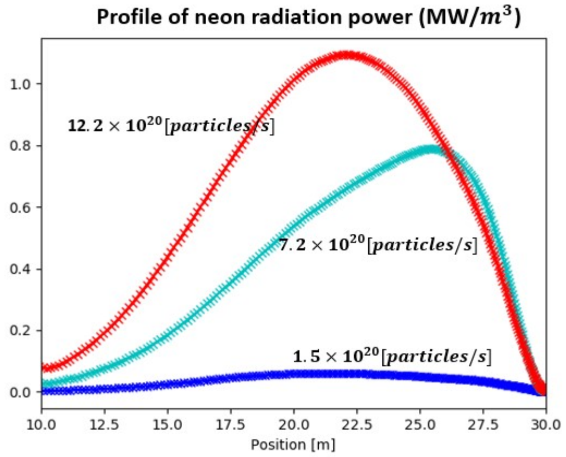

Figure 5.13: The profile of neon radiation power in the case of neon seeding rate 1.5×10^{20} [particles/s], 7.2×10^{20} [particles/s] and 12.2×10^{20} [particles/s]. The upstream density is fixed at $1.65 \times 10^{19}\text{m}^{-3}$. The target is located at 30m.

transports into the edge plasma will produce powerful radiation power inside the separatrix, dissipating the core plasma energy, thus affects plasma performance in the confined region [150][152]. According to [150], the neon impurity fraction in the core plasma cannot be over a fatal fraction, which is about 2.5%. In ITER or other devices, the fatal fraction will be slightly different due to different density limits and operating parameters.

5.4.2 Investigate the parallel momentum balance of neon ions $\text{Ne}^{3+} - \text{Ne}^{6+}$

In order to improve the understanding of parallel transport of neon impurities, this section investigates the parallel force balance of neon ions. Four neon species ($\text{Ne}^{3+} - \text{Ne}^{6+}$) are studied in the following parts, all of which are the main cooling charge states of neon impurity and all significantly affect the volumetric power loss in the divertor. To implement this work, (1) the detached case (neon seeding rate 12.2×10^{20} [particles/s] discussed in the previous section is used to analyse the density, fractional abundance and radiation of neon ions with parallel transport, while the 0D code 'Atomic++' [59] is used to analyse the quantities at the equilibrium with different electron temperatures (the temperature in divertor conditions from 0eV to 50eV). To make the simulations of the two codes comparable, the initial parameters of Atomic++ simulation are provided from the SD1D detached case, including the total neon impurity and the electron density as a function of electron temperature.

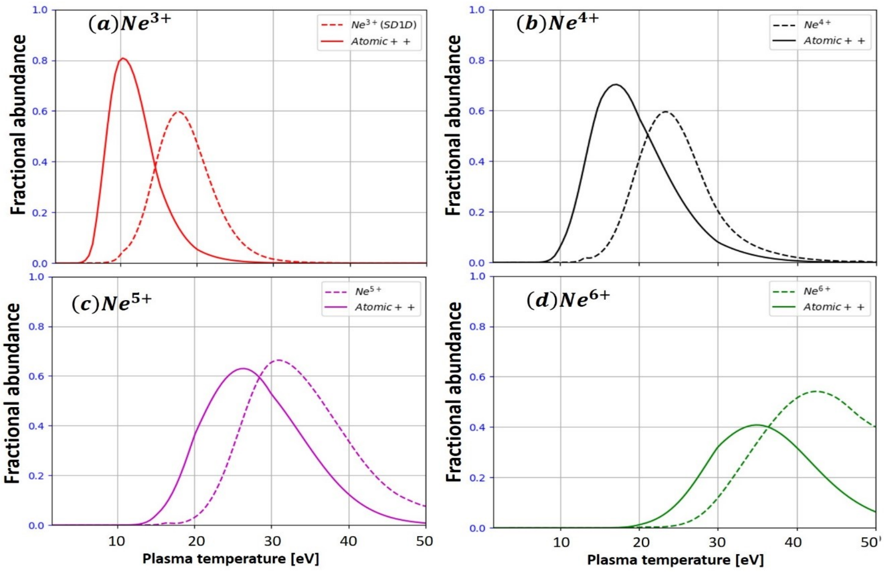

Figure 5.14: Solid line: Fractional abundance of neon ions ($\mathrm{Ne}^{3+} - \mathrm{Ne}^{6+}$) at the equilibrium with different electron temperatures, provided by the 0D code 'Atomic++'; Dashed line: Fractional abundance of neon ions ($\mathrm{Ne}^{3+} - \mathrm{Ne}^{6+}$) provided by SD1D simulation (the case with the neon seeding rate of 12.2×10^{20} [particles/s]. SD1D simulation provides initial parameters for Atomic++ simulation, including the total neon impurity and the electron density as a function of electron temperature.

Figure 5.14 shows the fractional abundance of the four neon ion species, presenting that the fractional abundance of every ion species provided by SD1D is located at a higher temperature compared to the Atomic++ result (which does not include transport). This indicates that the parallel transport pushes the neon ions towards the high temperature region (i.e. moves neon upstream). It is also found that the neon ion of a higher charge state is located at higher temperatures.

Parallel force balance

To understand why parallel transport changes the distribution of neon ions, it is necessary to investigate the force balance on these neon ions and analyse the effect of the forces on the parallel momentum balance. Corresponding to the fractional abundance, the density of neon ions from SD1D simulation in figure 5.15(a), figure 5.16(a), figure 5.17(a) and figure5.18(a) is located at higher temperatures compared to the neon ions without transport (from Atomic++). In figure 5.15(a) the neon radiation region is thus pushed upstream as well. The forces imposed on neon ions significantly influence their density distribution, including:

(1) force due to the electric field (section 3.5.1),

(2) friction forces between neon ions and other particle species,

(3) ion- and electron- thermal forces generated along temperature gradients due to coulomb collisions (section 3.5.3) and

(4) other collisional reactions (e.g. charge exchange recombination (CXR) and ionisation in section 5.2).

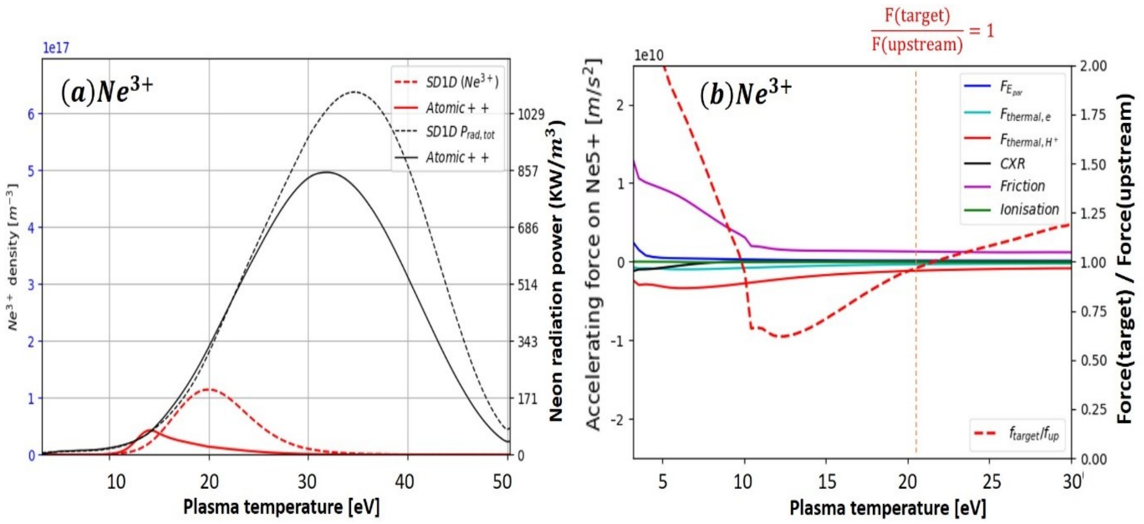

Figure 5.15: Solid line : density of Ne^{3+} (red) and the total neon radiation power (black) at the equilibrium with different electron temperatures, provided by the 0D code 'Atomic++'; Dashed line: the results provided by SD1D simulation (the case with the neon seeding rate of 12.2×10^{20} [particles/s]

Figure 5.15(b) shows the acceleration of Ne^{3+} caused by the forces. A positive acceleration means the direction is towards the target, while a negative acceleration means towards upstream. It is found that the friction force between Ne^{3+} and other particle species (primarily the H^+) is the dominant force towards the target, while the force caused by the parallel electric field is small and it affects the ion transport near the target since the plasma pressure gradient occurs in a small region in front of the target (Figure 5.6(a)).

The forces pushing Ne^{3+} back upstream include ion- and election- thermal forces, CXR and ionisation. Compared to the thermal forces, the force due to CXR and ionisation is small and is located near the target. Since neon seeding cannot effectively increase the plasma and neutral density near the target, collisional reactions cannot become stronger even in the detached phase, thus the reaction rate of CXR and ionisation remains relatively small. Here we calculate a ratio of the total force towards the target and the total force towards upstream $\frac{F(target)}{F(upstream)}$. It is found that the peak of Ne^{3+} density is located at the temperature where the ratio equals 1, which means all forces are eliminated and the acceleration of Ne^{3+} is zero. As shown in figure 5.15, the force in front of this location (at lower temperatures) pushes Ne^{3+} back to upstream and the force behind this position (at higher temperatures) pushes Ne^{3+} to the target, resulting in an exponential distribution of density. Since the friction force and the ion- and electron- thermal forces have Z dependence, both of them increase at the higher charge states in figure 5.16, figure 5.17 and figure 5.18. For the higher charge states, the position of ratio $\frac{F(target)}{F(upstream)} = 1$ is located at the higher temperature region, thus the peak density of the neon ion at higher charge states is located at higher temperatures (or further away from the target).

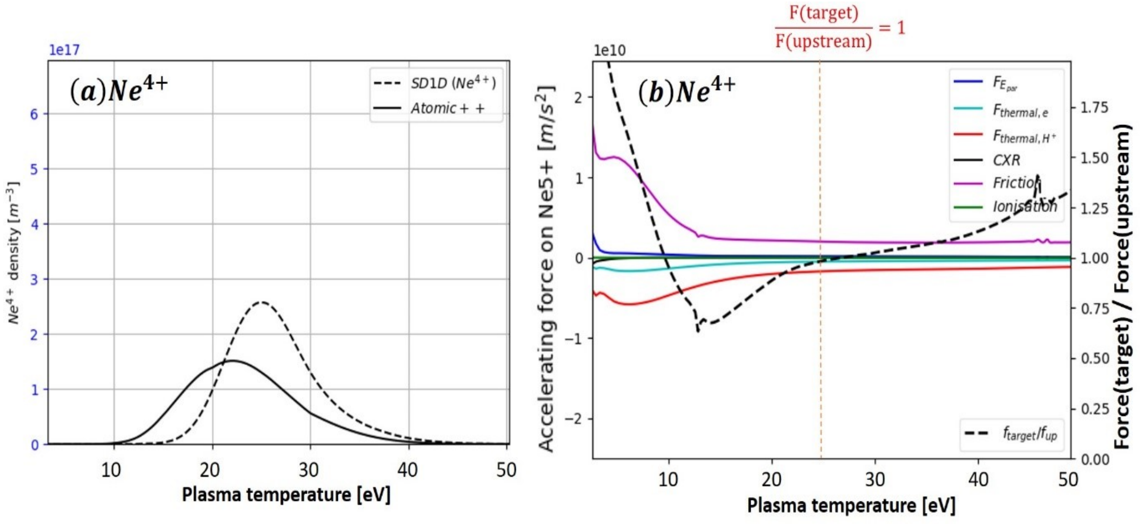

Figure 5.16: Solid line : density of Ne^{4+} (red) and the total neon radiation power (black) at the equilibrium with different electron temperatures, provided by the 0D code 'Atomic++'; Dashed line: the results provided by SD1D simulation (the case with the neon seeding rate of 12.2×10^{20} [particles/s]

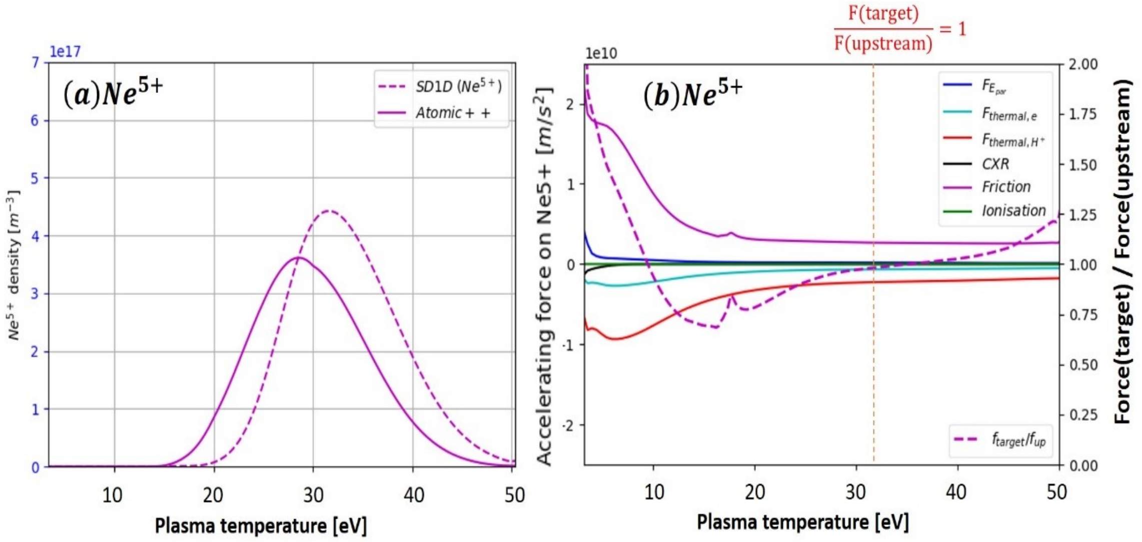

Figure 5.17: Solid line : density of Ne^{5+} (red) and the total neon radiation power (black) at the equilibrium with different electron temperatures, provided by the 0D code 'Atomic++'; Dashed line: the results provided by SD1D simulation (the case with the neon seeding rate of 12.2×10^{20} [particles/s]

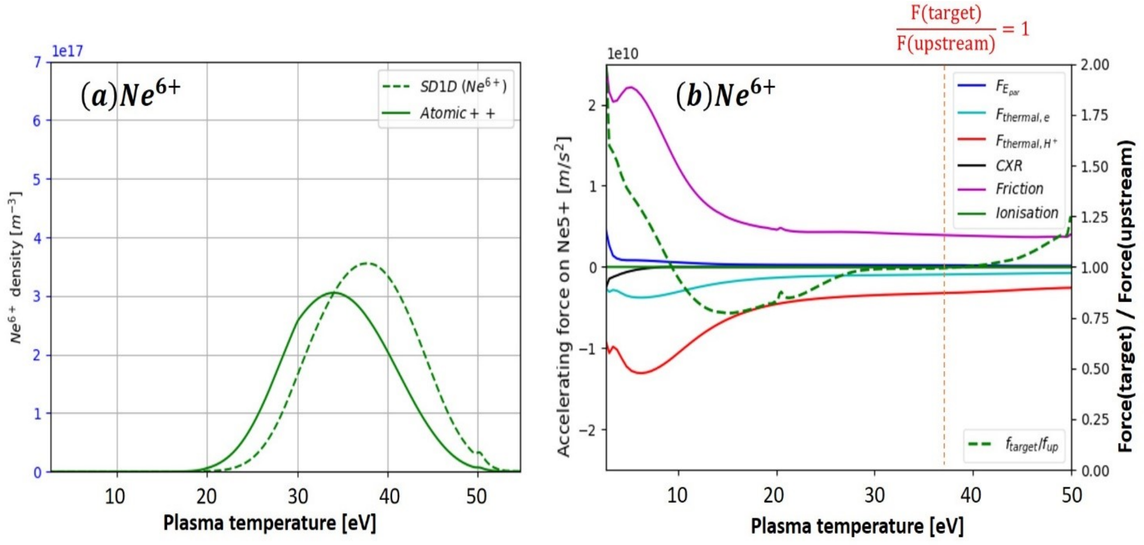

Figure 5.18: Solid line : density of Ne^{6+} (red) and the total neon radiation power (black) at the equilibrium with different electron temperatures, provided by the 0D code 'Atomic++'; Dashed line: the results provided by SD1D simulation (the case with the neon seeding rate of 12.2×10^{20} [particles/s]

5.5 Conclusions

Both density ramp and impurity seeding in the divertor are effective ways to achieve divertor detachment. In this chapter we have carried out simulations to compare the atomic and molecular physics in the two detachment regimes using the upgraded SD1D module. We set up simulations using MAST-U Super-X divertor conditions (section 5.2) [36] and implement two scans to achieve divertor detachment: (1) a scan of upstream density from $1.65 \times 10^{19}\text{m}^{-3}$ to $4.0 \times 10^{19}\text{m}^{-3}$ and (2) a scan of neon seeding rate is from 0.14×10^{20} [particles/s] to 1.81×10^{21} [particles/s]. To make the two scan comparable, the upstream density is fixed at $1.65 \times 10^{19}\text{m}^{-3}$ in the scan of neon seeding rate.

We found the rollover of the target plasma flux can be achieved during the two scans, and both the target temperature and the target plasma flux are effectively reduced in the detachment phase. But some crucial differences were found in the comparison including:

(1) Increasing neon seeding rate obtains a higher minimum target temperature (about 2.8eV) compared to the approach of increasing upstream density;

(2) The peak density of both plasma and neutral during the seeding rate scan increase much slowly near the target due to the relatively weak recycling process compared to the upstream density scan.

(3) The heat flux and plasma pressure can be effectively reduced by neon radiation power loss in the region apart from the recycling region, while they are mainly reduced in the recycling region in front of the target during the scan of upstream density.

Since the plasma-atom and plasma-molecule interations are sensitive to the variations of density and temperature. The differences of the two detachment regimes may lead to a different role of the atomic and molecular processes during the divertor detachment. (1) The dominant source of the main ion is ionisation, which is much higher during density ramp than the ionisation source during neon seeding. The lower ionisation during neon seeding is caused by the relatively low neutral density. (2) The direct excitation dominates hydrogenic radiation power loss and similar to the ionisation source it is much higher during the density ramp. (3) The molecular processes become more intensive during density ramp detachment, while it cannot be effectively intensified by increasing neon seeding rate since the minimum temperature is not the ideal temperature for plasma-molecule interactions (< 2eV). The different minimum temperature is found caused by the different volumetric power loss primarily due to the different hydrogenic cooling rate (sum of the net excitation radiation power and ionisation energy cost) in the two detachment regimes.

This chapter also investigates the parallel transport of neon impurities. We found that the parallel transport processes tend to push the neon ions towards the high temperature region (or towards upstream) and the parallel distribution of neon density is mainly determined by the parallel force balance. The peak density of the neon ions is located at the position where the ratio of the total force towards the target and the total force towards upstream $\frac{F(target)}{F(upstream)} = 1$

Chapter 6

Conclusions

6.1 Conclusions

Exhaust problem is a crucial problem for tokamak fusion research, which leads to large heat and particle flux flowing out from the fusion plasma and causes massive heat load on the facial materials (on vessel wall or divertor target plate). The heat load could reach or even become higher than the material limit and thus lead to serious facial material erosion. Divertor detachment is a potential solution to this problem, which can effectively reduce heat load on the target plates. Generally divertor detachment can be achieved through two ways: (1) increasing the plasma density at upstream or (2) seeding impurity in the divertor. But the process involves a complex atomic and molecular physics, which significantly affect the particle, momentum and energy balance in the divertor volume.

To investigate the role of atomic and molecular processes in the two detachment regimes, we implement upgrades in the original SD1D code in order to add the molecular process and neon impurity effects in the physical model (Chapter 3). After the upgrades, SD1D includes five hydrogenic species: H, H_2, H^+, H_2^+ and H^-, and the neon impurity in all charge states. The empirical functions used in hydrogen collision and radiation model have been replaced by the Amjuel database, which provides reaction rate coefficients and hydrogen population coefficients (have the dependence of both T_e and n_e) to the upgraded SD1D, while the ADAS database is used to provide the collision data for reactions of neon species. The upgraded SD1D module is able to (1) numerically simulate the molecular processes to investigate the role of atomic and molecular processes during the detachment achieved by a density ramp (see Chapter

4), and (2) it is able to model the divertor detachment achieved through impurity (neon) seeding (Chapter 5). Using the upgraded SD1D, we investigate the role of atomic and molecular species in MAST-U Super-X divertor conditions. In order to achieve divertor detachment in simulations, two scans (including upstream density scan and impurity (neon) seeding rate scan) have been implemented.

During the upstream density scan, we focus on the target plasma rollover and target temperature in the three recycling regimes:

(1) only neutral atoms produced by recycling (recycling ($H^+ -> H$)),

(2) only neutral molecules produced by recycling (recycling $H^+ -> H_2$)

(3) recycled atoms or recycled molecules with equal probability ($50\%H^+ -> H$ and $50\%H^+ -> H$)

It is found that molecules play an important role in the flux rollover, which occurs at a higher upstream density and a slightly lower target temperature if a larger proportion of H_2 produced by the recycling process. It indicates that using the target material that produces more recycled atoms may reduce the requirement of achieving divertor detachment. The molecule–plasma collisions are predicted to be as crucial as the atom–plasma collisions during the upstream density scan. Both of them account for the rise of plasma momentum loss at the beginning of detachment. The decomposition of plasma-molecule collisions shows that the momentum loss mechanism via plasma-molecule interactions is primarily due to plasma-molecule elastic collisions instead of molecular charge exchange during either attachment or detachment. The main reason is that the rate coefficient of plasma-molecule elastic is much higher than the rate coefficient of molecular charge exchange when $T_e < 10$eV.

Comparing the parallel profile of different reactions to the density profile of different particle species, we found that the distribution of plasma-atom reactions strongly corresponds to the atom density profile, while it is the same for molecular species.

The plasma-atom interactions is found to occur in the region apart from the target and the plasma-molecule interactions mainly occur near the target. The position of recycling region (at the target) and the lower temperature (especially during detachment) near the target may be the main reason that causes a high possibility for the plasma-molecule interaction occurring near the target. With the increase of upstream density, the source of the main ion moves towards the target, while the source of charged molecule is still located in a narrow region in front of the target. Corresponding to ionisation source, the profile of hydrogenic excitation radiation (primarily produced through direct excitation channel) moves towards X-point during the density ramp, while the molecular excitation channels are still located in front of the target. Although about 85% of hydrogenic excitation radiation attributes to direct excitation channel, molecular species that concentrate near the target determine the plasma and neutral profiles in front of the target during detachment and thus play a crucial role in the target performance.

Apart from the scan of upstream density, we carried out a scan of impurity (neon) seeding rate to achieve divertor detachment. We compared the effect of atomic and molecular processes on the particle, momentum and energy balance in the two detachment regimes. Crucial differences were found during the two scans: (1) Increasing neon seeding rate obtains a higher minimum target temperature (about 2.8eV) compared to the approach of increasing upstream density; (2)The peak density of both plasma and neutral during the seeding rate scan increase much more slowly near the target due to the relatively weak recycling process compared to the upstream density scan; (3) Neon radiation leads to a wider cooling region, which effectively reduces the heat flux and plasma pressure in the region apart from the recycling region, while upstream density ramp causes the reduction of heat flux and pressure occurring in the recycling region in front of the target.

The differences caused by the two detachment approaches may lead to a different role of the atomic and molecular processes during the divertor detachment, since the plasma-atom and plasma-molecule interactions are sensitive to the variations of density and temperature. First we found that ionisation is the main source of plasma ion in the two scans, but due to the larger neutral density during the upstream density ramp it becomes much larger compared to the ionisation source during the scan of neon seeding rate. Then we found the direct excitation corresponding to the ionisation source dominates hydrogenic radiation power loss, and it is much higher during density ramp compared to the case of seeding rate scan. Furthermore, it is very interesting that the plasma-molecule interactions become more intensive during the density ramp detachment, while it cannot be effectively intensified in the scan of seeding rate since the minimum temperature (about 2.8eV) achieved in simulations by neon seeding is not the ideal temperature for plasma-molecule interactions (< 2eV). The steep rise of both the momentum loss factor caused by plasma-molecule collisions and the H_{alpha} photon emission (which can be found during the upstream density ramp) does not occur during the neon seeding rate scan.

The main reason of different minimum target temperature may be caused by the momentum and energy balance, which are found to be different in the cases using the different detachment approach, thus the target temperature determined by the ratio of heat flux and plasma pressure at the target is also varied differently. The SD1D simulation found that the scan of neon seeding rate achieves a lower volumetric power loss and a similar target pressure compared to the density ramp case, thus neon seeding scan obtains a higher target temperature in the deep detachment phase. Although a lower heat flux at the target may be achieved by a higher neon seeding rate, the increase of neon seeding rate may lead to some crucial problems such as the neon concentration in edge plasma larger than the fatal fraction. Additionally in the simulations, the volumetric power sinks and volumetric momentum loss tend to be flat, thus the target temperature changes slowly at about the minimum target temperature in the deep detachment phase.

Besides the atomic and molecular processes, we also investigated parallel transport of neon impurity. We found that the parallel force balance tends to push the neon ions towards the high temperature region (or towards upstream) and the force balance determines the parallel profile of neon density. The peak density of neon ions is located at the position where the ratio of the total force towards the target and the total force towards upstream $\frac{F(target)}{F(upstream)} = 1$

6.2 Future work

This thesis focuses on the divertor detachment in the hydrogen plasma conditions. But the impact of isotope mass on particle, momentum and energy balance could be crucial for divertor physics [145][146][147]. Since SD1D has a wide applicability, it is able to simulate divertor detachment in different plasma conditions and in different divertor configurations. In future studies, it will be interesting to investigate the effects of molecular species on divertor detachment in other divertor configurations.

Divertor detachment control is a challenge for the detachment research. The code SOLPS has been used to model the detachment front location sensitivity to the control parameter variation (e.g. upstream density and input power) [153]. However, a main quantitative mismatch is found between the SOLPS and DLS mode predictions. DLS model predicts a faster upstream movement of the detachment front near the target after detachment onset compared to SOLPS simulation results. The main reason caused the mismatch is probably that DLS model assumes the thermal front width to be small compared to the divertor size and that plasma-neutral pressure balance is not considered. It is possible that the assumption of a thin thermal front may be maybe satisfied when the model is applied to reactor-level parallel heat fluxes [153]. As a result, further work needs to be done for understanding the dependence of the thermal front width on the power entering the divertor and on the impurity seeded in divertor to reduce the heat flux. It motivates further work using SD1D to study at the impact of the power entering the divertor and plasma-neutral pressure balance on the thermal front width and movement.

Appendix A

The definition of sources and sinks

The source and sink terms in the density equation(S), momentum equation(F) and energy equation(E and R) caused by the collisional reactions shown in table 1 are defined as below [48]:

Ionisation:

$$S_{\mathrm{H}}^{\mathrm{ion}} = -S_{\mathrm{H^+}}^{\mathrm{ion}} = n_{\mathrm{H}} n_e < \sigma v >_{\mathrm{ion}}$$
$$F_{\mathrm{H}}^{\mathrm{ion}} = -F_{\mathrm{H^+}}^{\mathrm{ion}} = m_{\mathrm{H}} V_{\mathrm{H}} n_{\mathrm{H}} n_e < \sigma v >_{\mathrm{ion}}$$
$$E_{\mathrm{H}}^{\mathrm{ion}} = -E_{\mathrm{H^+}}^{\mathrm{ion}} = \tfrac{3}{2} T_{\mathrm{H}} n_{\mathrm{H}} n_e < \sigma v >_{\mathrm{ion}}$$
$$R_e^{\mathrm{ion}} = 13.6\mathrm{eV} \times \mathrm{n_H n_e} < \sigma \mathrm{v} >_{\mathrm{ion}}$$

Electron-ion Recombination:

$$S_{\mathrm{H^+}}^{\mathrm{rec}} = -S_{\mathrm{H}}^{\mathrm{rec}} = n_{\mathrm{H^+}} n_e < \sigma v >_{\mathrm{rec}}$$
$$F_{\mathrm{H^+}}^{\mathrm{rec}} = -F_{\mathrm{H}}^{\mathrm{rec}} = m_{\mathrm{H^+}} V_{\mathrm{H^+}} n_{\mathrm{H^+}} n_e < \sigma v >_{\mathrm{rec}}$$
$$E_{\mathrm{H^+}}^{\mathrm{rec}} = -E_{\mathrm{H}}^{\mathrm{rec}} = \tfrac{3}{2} T_{\mathrm{H^+}} n_{\mathrm{H^+}} n_e < \sigma v >_{\mathrm{rec}}$$

Charge exchange (CX):

$$F_{\mathrm{H^+}}^{\mathrm{cx}} = -F_{\mathrm{H}}^{\mathrm{cx}} = n_{\mathrm{H^+}} n_{\mathrm{H}} < \sigma v >_{\mathrm{cx}} m_{\mathrm{H^+}} \left(V_{\mathrm{H^+}} - V_{\mathrm{H}}\right)$$
$$E_{\mathrm{H^+}}^{\mathrm{cx}} = -E_{\mathrm{H}}^{\mathrm{cx}} = n_{\mathrm{H^+}} n_{\mathrm{H}} < \sigma v >_{\mathrm{cx}} \tfrac{3}{2} \left(T_{\mathrm{H^+}} - T_{\mathrm{H}}\right)$$

Non-dissociative ionisation:

$$
\begin{aligned}
&S_{\mathrm{H_2}}^{\mathrm{ion}} = -S_{\mathrm{H_2}^+}^{\mathrm{ion}} = n_{\mathrm{H_2}} n_e {<}\, \sigma v\, {>}_{\mathrm{ion}}^{\mathrm{H_2}} \\
&F_{\mathrm{H_2}}^{\mathrm{ion}} = -F_{\mathrm{H_2}^+}^{\mathrm{ion}} = m_{\mathrm{H_2}} V_{\mathrm{H_2}} n_{\mathrm{H_2}} n_e {<}\, \sigma v\, {>}_{\mathrm{ion}}^{\mathrm{H_2}} \\
&E_{\mathrm{H_2}}^{\mathrm{ion}} = -E_{\mathrm{H_2}^+}^{\mathrm{ion}} = \tfrac{3}{2} T_{\mathrm{H_2}} n_{\mathrm{H_2}} n_e {<}\, \sigma v\, {>}_{\mathrm{ion}}^{\mathrm{H_2}}
\end{aligned}
$$

Dissociation:

$$
\begin{aligned}
&S_{\mathrm{H_2}}^{\mathrm{diss}} = -0.5 \times S_{\mathrm{H}}^{\mathrm{diss}} = n_{\mathrm{H_2}} n_e {<}\, \sigma v\, {>}_{\mathrm{diss}}^{\mathrm{H_2}} \\
&F_{\mathrm{H_2}}^{\mathrm{diss}} = -F_{\mathrm{H}}^{\mathrm{diss}} = m_{\mathrm{H_2}} V_{\mathrm{H_2}} n_{\mathrm{H_2}} n_e {<}\, \sigma v\, {>}_{\mathrm{diss}}^{\mathrm{H_2}} \\
&E_{\mathrm{H_2}}^{\mathrm{diss}} = -E_{\mathrm{H}}^{\mathrm{diss}} = \tfrac{3}{2} T_{\mathrm{H_2}} n_{\mathrm{H_2}} n_e {<}\, \sigma v\, {>}_{\mathrm{diss}}^{\mathrm{H_2}} \\
&R_e^{\mathrm{diss}} = 4.25\mathrm{eV} \times \mathrm{n_{H_2} n_e} {<}\, \sigma \mathrm{v}\, {>}_{\mathrm{diss}}^{\mathrm{H_2}}
\end{aligned}
$$

where 4.25eV is the bind energy of a hydrogen molecule;

Molecular charge exchange:

The momentum and energy of $\mathrm{H_2}$ transfer to $\mathrm{H_2^+}$, while the momentum and energy of $\mathrm{H^+}$ transfer to H.

$$
\begin{aligned}
&S_{\mathrm{H_2}}^{\mathrm{cx}} = S_{\mathrm{H^+}}^{\mathrm{cx}} = -S_{\mathrm{H_2}^+}^{\mathrm{cx}} = -S_{\mathrm{H}}^{\mathrm{cx}} = n_{\mathrm{H_2}} n_{\mathrm{H^+}} {<}\, \sigma v\, {>}_{\mathrm{cx}}^{\mathrm{H_2}} \\
&F_{\mathrm{H_2}}^{\mathrm{cx}} = -F_{\mathrm{H_2}^+}^{\mathrm{cx}} = m_{\mathrm{H_2}} V_{\mathrm{H_2}} n_{\mathrm{H_2}} n_{\mathrm{H^+}} {<}\, \sigma v\, {>}_{\mathrm{cx}}^{\mathrm{H_2}} \\
&F_{\mathrm{H^+}}^{\mathrm{cx}} = -F_{\mathrm{H}}^{\mathrm{cx}} = m_{\mathrm{H^+}} V_{\mathrm{H^+}} n_{\mathrm{H_2}} n_{\mathrm{H^+}} {<}\, \sigma v\, {>}_{\mathrm{cx}}^{\mathrm{H_2}} \\
&E_{\mathrm{H^+}}^{\mathrm{cx}} = -E_{\mathrm{H}}^{\mathrm{cx}} = \tfrac{3}{2} T_{\mathrm{H^+}} n_{\mathrm{H_2}} n_{\mathrm{H^+}} {<}\, \sigma v\, {>}_{\mathrm{cx}}^{\mathrm{H_2}} \\
&E_{\mathrm{H_2}}^{\mathrm{cx}} = -E_{\mathrm{H_2}^+}^{\mathrm{cx}} = \tfrac{3}{2} T_{\mathrm{H_2}} n_{\mathrm{H_2}} n_{\mathrm{H^+}} {<}\, \sigma v\, {>}_{\mathrm{cx}}^{\mathrm{H_2}}
\end{aligned}
$$

Dissociative excitation (DE):

$$
\begin{aligned}
&S_{\mathrm{H_2}^+}^{\mathrm{DE}} = -S_{\mathrm{H^+}}^{\mathrm{DE}} = -S_{\mathrm{H}}^{\mathrm{DE}} = n_{\mathrm{H_2}^+} n_e {<}\, \sigma v\, {>}_{\mathrm{DE}}^{\mathrm{H_2}^+} \\
&F_{\mathrm{H_2}^+}^{\mathrm{DE}} = -2 \times F_{\mathrm{H^+}}^{\mathrm{DE}} = -2 \times F_{\mathrm{H}}^{\mathrm{DE}} = m_{\mathrm{H_2}^+} V_{\mathrm{H_2}^+} n_{\mathrm{H_2}^+} n_e {<}\, \sigma v\, {>}_{\mathrm{DE}}^{\mathrm{H_2}^+} \\
&E_{\mathrm{H_2}^+}^{\mathrm{DE}} = -2 \times E_{\mathrm{H^+}}^{\mathrm{DE}} = -2 \times E_{\mathrm{H}}^{\mathrm{DE}} = \tfrac{3}{2} T_{\mathrm{H_2}^+} n_{\mathrm{H_2}^+} n_e {<}\, \sigma v\, {>}_{\mathrm{DE}}^{\mathrm{H_2}^+}
\end{aligned}
$$

Dissociative ionisation (DI):

$$S^{\mathrm{DI}}_{\mathrm{H_2}^+} = -0.5 \times S^{\mathrm{DI}}_{\mathrm{H^+}} = n_{\mathrm{H_2}^+} n_e < \sigma v >^{\mathrm{H_2}^+}_{\mathrm{DI}}$$
$$F^{\mathrm{DI}}_{\mathrm{H_2}^+} = -F^{\mathrm{DI}}_{\mathrm{H^+}} = m_{\mathrm{H_2}^+} V_{\mathrm{H_2}^+} n_{\mathrm{H_2}^+} n_e < \sigma v >^{\mathrm{H_2}^+}_{\mathrm{DI}}$$
$$E^{\mathrm{DI}}_{\mathrm{H_2}^+} = -E^{\mathrm{DI}}_{\mathrm{H^+}} = \tfrac{3}{2} T_{\mathrm{H_2}^+} n_{\mathrm{H_2}^+} n_e < \sigma v >^{\mathrm{H_2}^+}_{\mathrm{DI}}$$

Dissociative recombination (DR):

$$S^{\mathrm{DR}}_{\mathrm{H_2}^+} = -0.5 \times S^{\mathrm{DR}}_{\mathrm{H}} = n_{\mathrm{H_2}^+} n_e < \sigma v >^{\mathrm{H_2}^+}_{\mathrm{DR}}$$
$$F^{\mathrm{DR}}_{\mathrm{H_2}^+} = -F^{\mathrm{DR}}_{\mathrm{H}} = m_{\mathrm{H_2}^+} V_{\mathrm{H_2}^+} n_{\mathrm{H_2}^+} n_e < \sigma v >^{\mathrm{H_2}^+}_{\mathrm{DR}}$$
$$E^{\mathrm{DR}}_{\mathrm{H_2}^+} = -E^{\mathrm{DR}}_{\mathrm{H}} = \tfrac{3}{2} T_{\mathrm{H_2}^+} n_{\mathrm{H_2}^+} n_e < \sigma v >^{\mathrm{H_2}^+}_{\mathrm{DR}}$$

Molecular activated recombination (MAR) via H^-**:**

$$S^{\mathrm{MAR}}_{\mathrm{H_2}} = S^{\mathrm{MAR}}_{\mathrm{H^+}} = -\tfrac{1}{3} S^{\mathrm{MAR}}_{\mathrm{H}} = n_{\mathrm{H_2}} n_e < \sigma v >^{\mathrm{H_2}}_{\mathrm{MAR}}$$
$$F^{\mathrm{MAR}}_{\mathrm{H_2}} = m_{\mathrm{H_2}} V_{\mathrm{H_2}} n_{\mathrm{H_2}} n_e < \sigma v >^{\mathrm{H_2}}_{\mathrm{MAR}}$$
$$F^{\mathrm{MAR}}_{\mathrm{H^+}} = m_{\mathrm{H^+}} V_{\mathrm{H^+}} n_{\mathrm{H_2}} n_e < \sigma v >^{\mathrm{H_2}}_{\mathrm{MAR}}$$
$$F^{\mathrm{MAR}}_{\mathrm{H}} = -m_{\mathrm{H_2}} V_{\mathrm{H_2}} n_{\mathrm{H_2}} n_e < \sigma v >^{\mathrm{H_2}}_{\mathrm{MAR}} - m_{\mathrm{H^+}} V_{\mathrm{H^+}} n_{\mathrm{H_2}} n_e < \sigma v >^{\mathrm{H_2}}_{\mathrm{MAR}}$$
$$E^{\mathrm{MAR}}_{\mathrm{H_2}} = \tfrac{3}{2} T_{\mathrm{H_2}} n_{\mathrm{H_2}} n_e < \sigma v >^{\mathrm{H_2}}_{\mathrm{MAR}}$$
$$E^{\mathrm{MAR}}_{\mathrm{H^+}} = \tfrac{3}{2} T_{\mathrm{H^+}} n_{\mathrm{H_2}} n_e < \sigma v >^{\mathrm{H_2}}_{\mathrm{MAR}}$$
$$E^{\mathrm{MAR}}_{\mathrm{H}} = -E^{\mathrm{MAR}}_{\mathrm{H_2}} - E^{\mathrm{MAR}}_{\mathrm{H^+}} = -\tfrac{3}{2} T_{\mathrm{H_2}} n_{\mathrm{H_2}} n_e < \sigma v >^{\mathrm{H_2}}_{\mathrm{MAR}} - \tfrac{3}{2} T_{\mathrm{H^+}} n_{\mathrm{H_2}} n_e < \sigma v >^{\mathrm{H_2}}_{\mathrm{MAR}}$$

The energy sink of plasma caused by hydrogen excitation radiation is given by equation 3.18 in section 3.4.3.

Bibliography

[1] World Energy Council. World energy resources. unpublished work, 2016. https://www.worldenergy.org/publications/2016/world-energy-resources-2016/.

[2] Alessandro Clerici and G Alimonti. World energy resources. In *EPJ WEB of conferences*, volume 98, page 01001. EDP Sciences, 2015. doi:10.1051/epjconf/20159801001.

[3] Bert Brunekreef and Stephen T Holgate. Air pollution and health. *The lancet*, 360(9341):1233–1242, 2002. doi:10.1016/S0140-6736(02)11274-8.

[4] Robert Vandenbosch. *Nuclear fission*. Elsevier, 2012. https://books.google.co.uk/books?hl=en&lr=&id=RCeaisb73M0C&oi=fnd&pg=PP1&dq=nuclear+fission&ots=6Acitb2ww9&sig=4tIioHjrzeVGwaSNH-qZVRsjsNM&redir_esc=y#v=onepage&q=nuclear%20fission&f=false.

[5] Anil Markandya and Paul Wilkinson. Electricity generation and health. *The lancet*, 370(9591):979–990, 2007. doi:10.1016/S0140-6736(07)61253-7.

[6] Paris Agreement. Paris agreement. In *Report of the Conference of the Parties to the United Nations Framework Convention on Climate Change (21st Session, 2015: Paris). Retrived December*, volume 4, page 2017. HeinOnline, 2015. https://heinonline.org/HOL/LandingPage?handle=hein.journals/intlm55&div=46&id=&page=.

[7] Catherine Lane. Nuclear energy pros and cons, 2021. https://www.solarreviews.com/blog/nuclear-energy-pros-and-cons.

[8] Richard F Post. *Nuclear fusion*, volume 1. Annual Reviews 4139 El Camino

Way, PO Box 10139, Palo Alto, CA 94303-0139, USA, 1976. `https://www.annualreviews.org/doi/pdf/10.1146/annurev.eg.01.110176.001241`.

[9] Jeffrey P Freidberg. *Plasma physics and fusion energy.* Cambridge university press, 2008. doi:10.1017/CBO9780511755705.

[10] Mitsuru Kikuchi, Karl Lackner, and Minh Quang Tran. Fusion physics. `http://www-pub.iaea.org/books/IAEABooks/8879/Fusion-Physics`, 2012.

[11] Stephen O Dean. Search for the ultimate energy source: a history of the us fusion energy program. `https://link.springer.com/book/10.1007/978-1-4614-6037-4`, 2013.

[12] Norbert Holtkamp et al. An overview of the iter project. *Fusion Engineering and Design*, 82(5-14):427–434, 2007. doi:10.1016/j.fusengdes.2007.03.029.

[13] Sergio Ciattaglia, Gianfranco Federici, Luciana Barucca, Alessandro Lampasi, Simone Minucci, and Ivo Moscato. The european demo fusion reactor: Design status and challenges from balance of plant point of view. In *2017 IEEE International Conference on Environment and Electrical Engineering and 2017 IEEE Industrial and Commercial Power Systems Europe (EEEIC/I&CPS Europe)*, pages 1–6. IEEE, 2017. doi:10.1109/EEEIC.2017.7977853.

[14] G Federici, C Baylard, A Beaumont, and J Holden. The plan forward for eu demo. *Fusion Engineering and Design*, 173:112960, 2021. doi:10.1016/j.fusengdes.2021.112960.

[15] Tetsuo Tanabe. Tritium: Fuel of fusion reactors. `https://link.springer.com/book/10.1007/978-4-431-56460-7`, 2017.

[16] John Wesson and David J Campbell. *Tokamaks*, volume 149. Oxford university press, 2011. doi:10.1080/00107514.2012.720285.

[17] Yuhong Xu. A general comparison between tokamak and stellarator plasmas. *Matter and Radiation at Extremes*, 1(4):192–200, 2016. doi:10.1016/j.mre.2016.07.001.

[18] Francesca Maria Poli. Integrated tokamak modeling: When physics informs engineering and research planning. *Physics of Plasmas*, 25(5):055602, 2018. doi:10.1063/1.5021489.

[19] Peter C Stangeby et al. *The plasma boundary of magnetic fusion devices*, volume 224. Institute of Physics Pub. Philadelphia, Pennsylvania, 2000.

[20] IT Chapman, J Adamek, RJ Akers, S Allan, L Appel, O Asunta, M Barnes, N Ben Ayed, T Bigelow, W Boeglin, et al. Overview of mast results. *Nuclear Fusion*, 55(10):104008, 2015. doi:10.1088/0029-5515/55/10/104008.

[21] Tomejiro Yamagishi. Toroidal divertor tokamak. `https://inis.iaea.org/search/searchsinglerecord.aspx?recordsFor=SingleRecord&RN=19097300`, 1988.

[22] Th Eich, A Herrmann, G Pautasso, P Andrew, N Asakura, JA Boedo, Y Corre, ME Fenstermacher, JC Fuchs, W Fundamenski, et al. Power deposition onto plasma facing components in poloidal divertor tokamaks during type-i elms and disruptions. *Journal of nuclear materials*, 337:669–676, 2005. doi:10.1016/j.jnucmat.2004.09.051.

[23] Alexandre Fil, Bruce Lipschultz, David Moulton, Andrew Thornton, Ben Dudson, Omkar Myatra, Kevin Verhaegh, et al. Comparison between mast-u conventional and super-x configurations through solps-iter modelling. *arXiv preprint arXiv:2202.12604*, 2022. doi:10.1088/1741-4326/ac81d8.

[24] DD Ryutov, RH Cohen, TD Rognlien, and MV Umansky. The magnetic field structure of a snowflake divertor. *Physics of Plasmas*, 15(9):092501, 2008. doi:10.1063/1.2967900.

[25] JP Gunn, S Carpentier-Chouchana, F Escourbiac, T Hirai, S Panayotis, RA Pitts, Y Corre, R Dejarnac, M Firdaouss, M Kočan, et al. Surface heat loads on the iter divertor vertical targets. *Nuclear Fusion*, 57(4):046025, 2017. doi:10.1088/1741-4326/aa5e2a.

[26] B Lipschultz, X Bonnin, G Counsell, A Kallenbach, A Kukushkin, K Krieger, A Leonard, A Loarte, R Neu, RA Pitts, et al. Plasma–surface interaction,

scrape-off layer and divertor physics: implications for iter. *Nuclear Fusion*, 47(9):1189, 2007. doi:10.1088/0029-5515/47/9/016.

[27] H Reimerdes, S Alberti, P Blanchard, P Bruzzone, R Chavan, S Coda, BP Duval, A Fasoli, B Labit, B Lipschultz, et al. Tcv divertor upgrade for alternative magnetic configurations. *Nuclear Materials and Energy*, 12:1106–1111, 2017. doi:10.1016/j.nme.2017.02.013.

[28] C Theiler, B Lipschultz, J Harrison, B Labit, H Reimerdes, C Tsui, WAJ Vijvers, JA Boedo, BP Duval, S Elmore, et al. Results from recent detachment experiments in alternative divertor configurations on tcv. *Nuclear Fusion*, 57(7):072008, 2017. doi:10.1088/1741-4326/aa5fb7.

[29] A Kallenbach, M Bernert, R Dux, F Reimold, M Wischmeier, and ASDEX Upgrade Team. Analytical calculations for impurity seeded partially detached divertor conditions. *Plasma Physics and Controlled Fusion*, 58(4):045013, 2016. doi:10.1088/0741-3335/58/4/045013.

[30] Hans-Joachim Kunze. Introduction to plasma spectroscopy. `https://link.springer.com/book/10.1007/978-3-642-02233-3`, 2009.

[31] M Bernert, M Wischmeier, A Huber, F Reimold, B Lipschultz, C Lowry, S Brezinsek, R Dux, T Eich, A Kallenbach, et al. Power exhaust by sol and pedestal radiation at asdex upgrade and jet. *Nuclear Materials and Energy*, 12:111–118, 2017. doi:10.1016/j.nme.2016.12.029.

[32] Steffen Potzel. Experimental classification of divertor detachment. 2012. `https://pure.mpg.de/rest/items/item_2146310/component/file_2146309/content`.

[33] AJ Thornton, A Kirk, MAST Team, et al. Scaling of the scrape-off layer width during inter-elm h modes on mast as measured by infrared thermography. *Plasma Physics and Controlled Fusion*, 56(5):055008, 2014. doi:10.1088/0741-3335/56/5/055008.

[34] K-U Riemann. Plasma—sheath transition and bohm criterion. *Contributions to Plasma Physics*, 32(3-4):231–236, 1992. doi:10.1002/ctpp.2150320309.

[35] Kevin Verhaegh. *Spectroscopic investigations of detachment on TCV: Investigating the role of atomic physics on the ion current roll-over and the dynamics of detachment in TCV.* PhD thesis, University of York, 2018. `https://etheses.whiterose.ac.uk/22523/`.

[36] Benjamin Daniel Dudson, J Allen, T Body, Ben Chapman, C Lau, Luke Townley, D Moulton, J Harrison, and Bruce Lipschultz. The role of particle, energy and momentum losses in 1d simulations of divertor detachment. *Plasma Physics and Controlled Fusion*, 61(6):065008, 2019. doi:10.1088/1361-6587/ab1321.

[37] DE Post. A review of recent developments in atomic processes for divertors and edge plasmas. *Journal of nuclear materials*, 220:143–157, 1995. doi:10.1016/0022-3115(94)00453-6.

[38] Kevin Verhaegh, Bruce Lipschultz, JR Harrison, BP Duval, Alex Fil, Mirko Wensing, Chris Bowman, DS Gahle, Andrei Kukushkin, David Moulton, et al. The role of plasma-molecule interactions on power and particle balance during detachment on the tcv tokamak. *Nuclear Fusion*, 61(10):106014, 2021. doi:10.1088/1741-4326/ac1dc5.

[39] F Reimold, M Wischmeier, S Potzel, L Guimarais, D Reiter, M Bernert, M Dunne, T Lunt, et al. The high field side high density region in solps-modeling of nitrogen-seeded h-modes in asdex upgrade. *Nuclear Materials and Energy*, 12:193–199, 2017. doi:10.1016/j.nme.2017.01.010.

[40] F Reimold, M Wischmeier, M Bernert, S Potzel, A Kallenbach, HW Müller, B Sieglin, U Stroth, et al. Divertor studies in nitrogen induced completely detached h-modes in full tungsten asdex upgrade. *Nuclear Fusion*, 55(3):033004, 2015. doi:10.1088/0029-5515/55/3/033004.

[41] A Kallenbach, M Bernert, R Dux, L Casali, Th Eich, L Giannone, A Herrmann, R McDermott, A Mlynek, HW Müller, et al. Impurity seeding for tokamak power exhaust: from present devices via iter to demo. *Plasma Physics and Controlled Fusion*, 55(12):124041, 2013. doi:10.1088/0741-3335/55/12/124041.

[42] RA Pitts, A Kukushkin, A Loarte, A Martin, M Merola, CE Kessel, V Komarov, and M Shimada. Status and physics basis of the iter divertor. *Physica Scripta*, 2009(T138):014001, 2009. doi:10.1088/0031-8949/2009/T138/014001.

[43] HP Summers and MG O'Mullane. Atomic data and modelling for fusion: the adas project. In *AIP Conference Proceedings*, volume 1344, pages 179–187. American Institute of Physics, 2011. doi:10.1063/1.3585817.

[44] D Reiter et al. *The data file AMJUEL: additional atomic and molecular data for EIRENE*, volume 52425. 2000. `http://eirene.de/amjuel.pdf`.

[45] Ratko K Janev, Detlev Reiter, and Ulrich Samm. *Collision processes in low-temperature hydrogen plasmas*, volume 4105. Forschungszentrum, Zentralbibliothek Jülich, 2003. `http://eirene.de/hydhel.pdf`.

[46] D Wünderlich, M Giacomin, R Ritz, and U Fantz. Yacora on the web: Online collisional radiative models for plasmas containing h, h2 or he. *Journal of Quantitative Spectroscopy and Radiative Transfer*, 240:106695, 2020. doi:10.1016/j.jqsrt.2019.106695.

[47] HP Summers, WJ Dickson, MG O'mullane, NR Badnell, AD Whiteford, DH Brooks, J Lang, SD Loch, and DC Griffin. Ionization state, excited populations and emission of impurities in dynamic finite density plasmas: I. the generalized collisional–radiative model for light elements. *Plasma Physics and Controlled Fusion*, 48(2):263, 2006. doi:10.1088/0741-3335/48/2/007.

[48] Yulin Zhou, Benjamin Dudson, Fulvio Militello, Kevin Verhaegh, and Omkar Myatra. Investigation of the role of hydrogen molecules in 1d simulation of divertor detachment. *Plasma Physics and Controlled Fusion*, 64(6):065006, 2022. doi:10.1088/1361-6587/ac6827.

[49] M Groth, EM Hollmann, AE Jaervinen, AW Leonard, AG McLean, CM Samuell, D Reiter, SL Allen, P Boerner, S Brezinsek, et al. Edge2d-eirene predictions of molecular emission in diii-d high-recycling divertor plasmas. *Nuclear Materials and Energy*, 19:211–217, 2019. doi:10.1016/j.nme.2019.02.035.

[50] Ursel Fantz. Emission spectroscopy of hydrogen molecules in technical and divertor plasmas. *Contributions to Plasma Physics*, 42(6-7):675–684, 2002. doi:10.1002/1521-3986(200211)42:6/7¡675::AID-CTPP675¿3.0.CO;2-6.

[51] EM Hollmann, S Brezinsek, NH Brooks, M Groth, AG McLean, A Yu Pigarov, and DL Rudakov. Spectroscopic measurement of atomic and molecular deuterium fluxes in the diii-d plasma edge. *Plasma physics and controlled fusion*, 48(8):1165, 2006. doi:10.1088/0741-3335/48/8/009.

[52] Kevin Verhaegh, Bruce Lipschultz, Basil P Duval, Olivier Février, Alexandre Fil, Christian Theiler, Mirko Wensing, Christopher Bowman, DS Gahle, JR Harrison, et al. An improved understanding of the roles of atomic processes and power balance in divertor target ion current loss during detachment. *Nuclear Fusion*, 59(12):126038, 2019. doi:10.1088/1741-4326/ab4251.

[53] K Verhaegh, Bruce Lipschultz, BP Duval, Alexandre Fil, M Wensing, Christopher Bowman, DS Gahle, et al. Novel inferences of ionisation and recombination for particle/power balance during detached discharges using deuterium balmer line spectroscopy. *Plasma Physics and Controlled Fusion*, 61(12):125018, 2019. doi:10.1088/1361-6587/ab4f1e.

[54] AS Kukushkin, SI Krasheninnikov, AA Pshenov, and D Reiter. Role of molecular effects in divertor plasma recombination. *Nuclear Materials and Energy*, 12:984–988, 2017. doi:10.1016/j.nme.2016.12.030.

[55] Edmond M Dewan. Generalizations of the saha equation. *The Physics of Fluids*, 4(6):759–764, 1961. doi:10.1063/1.1706395.

[56] Ursel Fantz, D Reiter, Bernd Heger, and D Coster. Hydrogen molecules in the divertor of asdex upgrade. *Journal of Nuclear Materials*, 290:367–373, 2001. doi:10.1016/S0022-3115(00)00638-3.

[57] A Yu Pigarov and SI Krasheninnikov. Application of the collisional-radiative, atomic-molecular model to the recombining divertor plasma. *Physics Letters A*, 222(4):251–257, 1996. doi:10.1016/0375-9601(96)00629-9.

[58] Sven Wiesen, Detlev Reiter, Vladislav Kotov, Martine Baelmans, Wouter Dekeyser, AS Kukushkin, SW Lisgo, RA Pitts, Vladimir Rozhansky, Gabriella Saibene, et al. The new solps-iter code package. *Journal of nuclear materials*, 463:480–484, 2015. doi:10.1016/j.jnucmat.2014.10.012.

[59] Tom Body. Simulating radiative cooling and detachment in a divertor plasma, 2017.

[60] Ian H Hutchinson. Thermal front analysis of detached divertors and marfes. *Nuclear Fusion*, 34(10):1337, 1994. doi:10.1088/0029-5515/34/10/I04.

[61] M Carr, A Meakins, A Baciero, M Bernert, A Callarelli, A Field, C Giroud, J Harrison, N Hawkes, S Henderson, et al. Towards integrated data analysis of divertor diagnostics with ray-tracing. In *44th EPS Conference on Plasma Physics*. European Physical Society, 2017. `https://pure.mpg.de/rest/items/item_2551454/component/file_3318129/content`.

[62] MG Dunne, S Potzel, F Reimold, M Wischmeier, E Wolfrum, Lorenzo Frassinetti, M Beurskens, P Bilkova, M Cavedon, R Fischer, et al. The role of the density profile in the asdex-upgrade pedestal structure. *Plasma Physics and Controlled Fusion*, 59(1):014017, 2016. doi10.1088/0741-3335/59/1/014017.

[63] Martin Greenwald, JL Terry, SM Wolfe, S Ejima, MG Bell, SM Kaye, and GH Neilson. A new look at density limits in tokamaks. *Nuclear Fusion*, 28(12):2199, 1988. doidoi.org/10.1088/0029-5515/28/12/009.

[64] Kedong Li, Zhongshi Yang, Huiqian Wang, Guosheng Xu, Qiping Yuan, Houyang Guo, David Eldon, Alan Hyatt, David Humphreys, Meiwen Chen, et al. Comparison of divertor behavior and plasma confinement between argon and neon seeding in east. *Nuclear Fusion*, 61(6):066013, 2021. doi:10.1088/1741-4326/abf418.

[65] O Février, C Theiler, JR Harrison, CK Tsui, K Verhaegh, C Wüthrich, JA Boedo, H De Oliveira, BP Duval, B Labit, et al. Nitrogen-seeded divertor detachment in tcv l-mode plasmas. *Plasma Physics and Controlled Fusion*, 62(3):035017, 2020. doi10.1088/1361-6587/ab6b00.

[66] David Moulton, PC Stangeby, X Bonnin, and RA Pitts. Comparison between solps-4.3 and the lengyel model for iter baseline neon-seeded plasmas. *Nuclear Fusion*, 61(4):046029, 2021. doi:10.1088/1741-4326/abe4b2.

[67] Gijs Lukas Derks. Developing a physics-based dynamic model of the divertor plasma. `https://pure.tue.nl/ws/portalfiles/portal/194477700/0940505_Derks_G.L._MSc_thesis_Thesis_NF.pdf`.

[68] PC Stangeby. Basic physical processes and reduced models for plasma detachment. *Plasma Physics and Controlled Fusion*, 60(4):044022, 2018. doi:10.1088/1361-6587/aaacf6.

[69] Thomas Nicholas. *Reduced simulations of scrape-off-layer turbulence.* PhD thesis, University of York, 2021.

[70] PC Stangeby. Can detached divertor plasmas be explained as self-sustained gas targets? *Nuclear Fusion*, 33(11):1695, 1993. doi:10.1088/0029-5515/33/11/I10.

[71] SI Krasheninnikov and AS Kukushkin. Physics of ultimate detachment of a tokamak divertor plasma. *Journal of Plasma Physics*, 83(5), 2017. doi:10.1017/S0022377817000654.

[72] JL Terry, B Lipschultz, X Bonnin, C Boswell, SI Krasheninnikov, A Yu Pigarov, B LaBombard, DA Pappas, and HA Scott. The experimental determination of the volume recombination rate in tokamak divertors. *Journal of nuclear materials*, 266:30–36, 1999. doi:10.1016/S0022-3115(98)00812-5.

[73] B Lipschultz, JL Terry, C Boswell, JA Goetz, AE Hubbard, SI Krasheninnikov, B LaBombard, DA Pappas, CS Pitcher, F Wising, et al. The role of particle sinks and sources in alcator c-mod detached divertor discharges. *Physics of Plasmas*, 6(5):1907–1916, 1999. doi:10.1063/1.873448.

[74] K Borrass, D Coster, D Reiter, and R Schneider. Study of recombining gas targets. *Journal of nuclear materials*, 241:250–254, 1997. doi:10.1016/S0022-3115(97)80044-X.

[75] D Lumma, JL Terry, and B Lipschultz. Radiative and three-body recombination in the alcator c-mod divertor. *Physics of Plasmas*, 4(7):2555–2566, 1997. doi:10.1063/1.872234.

[76] JL Terry, B Lipschultz, A Yu Pigarov, SI Krasheninnikov, B LaBombard, D Lumma, H Ohkawa, D Pappas, and M Umansky. Volume recombination and opacity in alcator c-mod divertor plasmas. *Physics of Plasmas*, 5(5):1759–1766, 1998. doi:10.1063/1.872845.

[77] EDA ITER et al. Power and particle control. *Nuclear Fusion*, 39(12 ITER physics basis):2391–2469, 1999. doi:10.1088/0029-5515/39/12/304.

[78] AW Leonard, MA Mahdavi, SL Allen, NH Brooks, ME Fenstermacher, DN Hill, CJ Lasnier, R Maingi, GD Porter, TW Petrie, et al. Distributed divertor radiation through convection in diii-d. *Physical review letters*, 78(25):4769, 1997. doi:doi.org/10.1103/PhysRevLett.78.4769.

[79] Arne Kallenbach, M Bernert, M Beurskens, L Casali, M Dunne, T Eich, L Giannone, A Herrmann, M Maraschek, S Potzel, et al. Partial detachment of high power discharges in asdex upgrade. *Nuclear Fusion*, 55(5):053026, 2015. doi:10.1088/0029-5515/55/5/053026.

[80] AW Leonard, MA Mahdavi, CJ Lasnier, TW Petrie, and PC Stangeby. Scaling radiative divertor solutions to high power in diii-d. *Nuclear Fusion*, 52(6):063015, 2012. doi:10.1088/0029-5515/52/6/063015.

[81] SI Krasheninnikov. Physical mechanisms in divertors and their impact on the core. *Czechoslovak journal of physics*, 48(2):97–112, 1998. doi:10.1007/s10582-998-0027-7.

[82] S Potzel, M Wischmeier, M Bernert, R Dux, HW Müller, A Scarabosio, et al. A new experimental classification of divertor detachment in asdex upgrade. *Nuclear Fusion*, 54(1):013001, 2013. doi:10.1088/0029-5515/54/1/013001.

[83] AW Leonard. Plasma detachment in divertor tokamaks. *Plasma Physics and Controlled Fusion*, 60(4):044001, 2018. doi:10.1088/1361-6587/aaa7a9.

[84] A Kallenbach, R Dux, V Mertens, O Gruber, G Haas, M Kaufmann, W Poschenrieder, F Ryter, H Zohm, M Alexander, et al. H mode discharges with feedback controlled radiative boundary in the asdex upgrade tokamak. *Nuclear Fusion*, 35(10):1231, 1995. doi:10.1088/0029-5515/35/10/I07.

[85] A Loarte, B Lipschultz, AS Kukushkin, GF Matthews, PC Stangeby, N Asakura, GF Counsell, G Federici, A Kallenbach, K Krieger, et al. Power and particle control. *Nuclear Fusion*, 47(6):S203, 2007. doi:10.1088/0029-5515/47/6/S04.

[86] K Ikeda. Progress in the iter physics basis. *Nuclear Fusion*, 47(6):E01, 2007. doi:10.1088/0029-5515/47/6/E01.

[87] Martin Greenwald, RL Boivin, F Bombarda, PT Bonoli, CL Fiore, D Garnier, JA Goetz, SN Golovato, MA Graf, RS Granetz, et al. H mode confinement in alcator c-mod. *Nuclear Fusion*, 37(6):793, 1997. doi:10.1088/0029-5515/37/6/I07.

[88] R Aratari, S Adamson, M Bessenrodt-Weberpals, R Buechse, A Carlson, C-C Chu, K Desinger, G Haas, J Hofmann, E Kakoulidis, et al. Comparison of open-closed divertor geometries in asdex. *Journal of nuclear materials*, 176:512–517, 1990. doi:10.1016/0022-3115(90)90098-8.

[89] K Bol, M Okabayashi, and R Fonck. The poloidal divertor experiment (pdx) and the princeton beta experiment (pbx). *Nucl. Fusion*, 25(9):1149–1153, 1985. `https://inis.iaea.org/collection/NCLCollectionStore/_Public/17/007/17007843.pdf#page=48`.

[90] Detlev Reiter, Martine Baelmans, and Petra Boerner. The eirene and b2-eirene codes. *Fusion science and technology*, 47(2):172–186, 2005. doi:10.13182/FST47-172.

[91] I Bykov, DL Rudakov, A Yu Pigarov, EM Hollmann, J Guterl, JA Boedo, CP Chrobak, T Abrams, HY Guo, CJ Lasnier, et al. Impact of divertor material on neutral recycling and discharge fueling in diii-d. *Physica Scripta*, 2020(T171):014058, 2020. doi:10.1088/1402-4896/ab5a2e.

[92] B Viola, G Calabró, AE Jaervinen, I Lupelli, G Rubino, S Wiesen, M Wischmeier, and JET EFDA Contributors. Impact of poloidal flux expansion on jet divertor radiation. In *44th EPS Conference on Plasma Physics*. European Physical Society, 2017. `https://pure.mpg.de/rest/items/item_2553820/component/file_3318222/content`.

[93] A Loarte and PJ Harbour. Effect of the magnetic flux geometry of a poloidal divertor on the profiles and parameters at the target. *Nuclear fusion*, 32(4):681, 1992. doi:10.1088/0029-5515/32/4/I13.

[94] VA Soukhanovskii, RE Bell, A Diallo, S Gerhardt, S Kaye, E Kolemen, BP LeBlanc, A McLean, JE Menard, SF Paul, et al. Advanced divertor configurations with large flux expansion. *Journal of Nuclear Materials*, 438:S96–S101, 2013. doi:10.1016/j.jnucmat.2013.01.015.

[95] Alexandre Fil, B Lipschultz, D Moulton, BD Dudson, O Février, O Myatra, C Theiler, K Verhaegh, M Wensing, MST EUROfusion, et al. Separating the roles of magnetic topology and neutral trapping in modifying the detachment threshold for tcv. *Plasma Physics and Controlled Fusion*, 62(3):035008, 2020. doi:10.1088/1361-6587/ab69bb.

[96] D Moulton, J Harrison, B Lipschultz, and D Coster. Using solps to confirm the importance of total flux expansion in super-x divertors. *Plasma Physics and Controlled Fusion*, 59(6):065011, 2017. doi:10.1088/1361-6587/aa6b13.

[97] James Robert Harrison. Characterisation of detached plasmas on the mast tokamak, 2010. `https://etheses.whiterose.ac.uk/1524/`.

[98] Francis F Chen. Langmuir probe diagnostics. In *Mini-Course on Plasma Diagnostics, IEEEICOPS meeting, Jeju, Korea*, pages 20–111, 2003. `http://www.seas.ucla.edu/~ffchen/Publs/Chen210R.pdf`.

[99] Gerald Schubert. *Treatise on geophysics*. Elsevier, 2015. `https://books.google.co.uk/books?hl=en&lr=&id=Rg6dBAAAQBAJ&oi=fnd&pg=PP1&dq=P.+Falkner,+R.+Schulz,+in+Treatise+on+Geophysics+(Second+`

`Edition),+2015&ots=VJ82PxR08E&sig=mX7USN-MAQx1rL-9-OR2EpVk3wE&redir_esc=y#v=onepage&q&f=false`.

[100] Ian H Hutchinson. Principles of plasma diagnostics. *Plasma Physics and Controlled Fusion*, 44(12):2603, 2002. doi:10.1088/0741-3335/44/12/701.

[101] O Février, C Theiler, H De Oliveira, B Labit, N Fedorczak, and A Baillod. Analysis of wall-embedded langmuir probe signals in different conditions on the tokamak à configuration variable. *Review of Scientific Instruments*, 89(5):053502, 2018. doi:10.1063/1.5022459.

[102] J Boedo, D Gray, L Chousal, R Conn, B Hiller, and KH Finken. Fast scanning probe for tokamak plasmas. *Review of scientific instruments*, 69(7):2663–2670, 1998. doi:10.1063/1.1148995.

[103] JA Boedo, N Crocker, L Chousal, R Hernandez, J Chalfant, H Kugel, P Roney, J Wertenbaker, and NSTX Team. Fast scanning probe for the nstx spherical tokamak. *Review of Scientific Instruments*, 80(12):123506, 2009. doi:10.1063/1.3266065.

[104] JG Clark, MD Bowden, and R Scannell. Low temperature thomson scattering on mast-u. *Review of Scientific Instruments*, 92(4):043545, 2021. doi:10.1063/5.0043813.

[105] B Lipschultz, B LaBombard, JL Terry, C Boswell, and IH Hutchinson. Divertor physics research on alcator c-mod. *Fusion science and technology*, 51(3):369–389, 2007. doi:10.13182/FST07-A1428.

[106] BA Lomanowski, AG Meigs, RM Sharples, M Stamp, C Guillemaut, and JET Contributors. Inferring divertor plasma properties from hydrogen balmer and paschen series spectroscopy in jet-ilw. *Nuclear Fusion*, 55(12):123028, 2015. doi:10.1088/0029-5515/55/12/123028.

[107] M Koubiti, Yannick Marandet, A Escarguel, H Capes, L Godbert-Mouret, R Stamm, C De Michelis, R Guirlet, and M Mattioli. Analysis of asymmetric

dα spectra emitted in front of a neutralizer plate of the tore-supra ergodic divertor. *Plasma physics and controlled fusion*, 44(2):261, 2002. doi:10.1088/0741-3335/44/2/309.

[108] R Neu, R Dux, A Geier, A Kallenbach, R Pugno, V Rohde, D Bolshukhin, JC Fuchs, O Gehre, O Gruber, et al. Impurity behaviour in the asdex upgrade divertor tokamak with large area tungsten walls. *Plasma physics and controlled fusion*, 44(6):811, 2002. doi:10.1088/0741-3335/44/6/313.

[109] James Robert Harrison, SW Lisgo, KJ Gibson, P Tamain, J Dowling, Mast Team, et al. Characterisation of detached plasmas on the mast tokamak. *Journal of nuclear materials*, 415(1):S379–S382, 2011. doi:10.1016/j.jnucmat.2010.12.226.

[110] X Feng, A Calcines, RM Sharples, B Lipschultz, A Perek, WAJ Vijvers, JR Harrison, JS Allcock, Y Andrebe, BP Duval, et al. Development of an 11-channel multi wavelength imaging diagnostic for divertor plasmas in mast upgrade. *Review of Scientific Instruments*, 92(6):063510, 2021. doi:10.1063/5.0043533.

[111] Hailong Du, Chaofeng Sang, Liang Wang, Xavier Bonnin, Houyang Guo, Jizhong Sun, and Dezhen Wang. Solps5. 1 analysis of detachment with drifts and gas pumping effects in east. *Plasma Physics and Controlled Fusion*, 58(8):085006, 2016. doi:10.1088/0741-3335/58/8/085006.

[112] Hugo Bufferand, Guido Ciraolo, Yannick Marandet, Jérome Bucalossi, Ph Ghendrih, Jamie Gunn, N Mellet, Patrick Tamain, R Leybros, Nicolas Fedorczak, et al. Numerical modelling for divertor design of the west device with a focus on plasma–wall interactions. *Nuclear Fusion*, 55(5):053025, 2015. doi:10.1088/0029-5515/55/5/053025.

[113] R Mao, N Fedorczak, G Ciraolo, H Bufferand, Y Marandet, J Bucalossi, P Tamain, Eric Serre, GY Zheng, and JX Li. Impact of an alternative divertor configuration on plasma detachment: pure deuterium simulations using the soledge2d-eirene edge transport code for hl-2m scenarios. *Nuclear Fusion*, 59(10):106019, 2019. doi:10.1088/1741-4326/ab3005.

[114] Xavier Bonnin, Wouter Dekeyser, Richard Pitts, David Coster, Serguey Voskoboynikov, and Sven Wiesen. Presentation of the new solps-iter code package for tokamak plasma edge modelling. *Plasma and Fusion Research*, 11:1403102–1403102, 2016. doi:10.1585/pfr.11.1403102.

[115] Makoto Nakamura, Satoshi Togo, Masanori Ito, and Yuichi Ogawa. One-dimensional time dependent analysis of the detachment front in a divertor plasma: Roles of the cross-field transport. *Plasma and Fusion Research*, 6:2403098–2403098, 2011. doi:10.1585/pfr.6.2403098.

[116] E Havlíčková, W Fundamenski, Volker Naulin, Anders Henry Nielsen, R Zagórski, J Seidl, and J Horáček. Steady-state and time-dependent modelling of parallel transport in the scrape-off layer. *Plasma Physics and Controlled Fusion*, 53(6):065004, 2011. doi:10.1088/0741-3335/53/6/065004.

[117] Satoshi Togo, Makoto Nakamura, Yuichi Ogawa, Katsuhiro Shimizu, Tomonori Takizuka, and Kazuo Hoshino. Effects of neutral particles on the stability of the detachment fronts in divertor plasmas. *Plasma and Fusion Research*, 8:2403096–2403096, 2013. doi:10.1585/pfr.8.2403096.

[118] M V Umansky. Status and verification of edge plasma turbulence code bout. *Computer Physics Communications*, 180(6):887–903, 2009. doi:10.1016/j.cpc.2008.12.012.

[119] B D Dudson. Bout++: A framework for parallel plasma fluid simulations. *Computer Physics Communicationss*, 180(6):1467–1480, 2009. doi:10.1016/j.cpc.2009.03.008.

[120] B D Dudson. Bout++: Recent and current developments. *Journal of Plasma Physics*, 81, 2014. doi:10.1017/S0022377814000816.

[121] B D Dudson. Verification of bout++ by the method of manufactured solutions. *Physics of Plasmas*, 23(6):1467–1480, 2016. doi:10.1063/1.4953429.

[122] GZ Deng, XQ Xu, NM Li, XJ Liu, X Liu, JC Xu, W Feng, JB Liu, SL Gao, SC Liu, et al. Simulation of divertor heat flux width on east by bout++ transport code. *Nuclear Fusion*, 60(8):082007, 2020. doi:10.1088/1741-4326/ab70d6.

[123] Fabio Riva, Fulvio Militello, Sarah Elmore, John Tomotoro Omotani, Benjamin Daniel Dudson, and N Walkden. Three-dimensional plasma edge turbulence simulations of mast and comparison with experimental measurements. *Plasma Physics and Controlled Fusion*, 2019. doi:10.1088/1361-6587/ab3561.

[124] B. D. Dudson. Bout++ documentation. `https://bout-dev.readthedocs.io/en/latest/`, 2019.

[125] Ben Dudson. Sd1d and hermes, 2018. `https://bout.llnl.gov/sites/bout/files/2018-08-16_Dudson.pdf`.

[126] E Havlíčková, W Fundamenski, F Subba, D Cnote=doi:10.1585/pfr.8.2403096oster, M Wischmeier, and G Fishpool. Benchmarking of a 1d scrape-off layer code solf1d with solps and its use in modelling long-legged divertors. *Plasma Physics and Controlled Fusion*, 55(6):065004, 2013. doi:10.1088/0741-3335/55/6/065004.

[127] Jarrod Leddy, B Dudson, and H Willett. Simulation of the interaction between plasma turbulence and neutrals in linear devices. *Nuclear Materials and Energy*, 12:994–998, 2017. doi:10.1016/j.nme.2016.09.020.

[128] David Wagner. Atomic, 2016. `https://github.com/cfe316/atomic`.

[129] Chen Zhang, Chaofeng Sang, Liang Wang, Mingyu Chang, Daoyuan Liu, and Dezhen Wang. Effect of carbon and tungsten plasma-facing materials on the divertor and pedestal plasma in east. *Plasma Physics and Controlled Fusion*, 61(11):115013, 2019. doi:10.1088/1361-6587/ab45de.

[130] Yuri Ralchenko et al. Nist standard reference database 78, 2019. doi:10.18434/T4W30F.

[131] K Verhaegh, B Lipschultz, C Bowman, BP Duval, U Fantz, A Fil, JR Harrison, D Moulton, O Myatra, D Wünderlich, et al. A novel hydrogenic spectroscopic technique for inferring the role of plasma–molecule interaction on power and particle balance during detached conditions. *Plasma Physics and Controlled Fusion*, 63(3):035018, 2021. doi:10.1088/1361-6587/abd4c0.

[132] Vladislav Kotov, Detlev Reiter, and Andrey S Kukushkin. Numerical study of the iter divertor plasma with the b2-eirene code package. Technical report, Forschungszentrum Juelich (Germany). Inst. fuer Energieforschung (IEF), 2007. `https://inis.iaea.org/search/search.aspx?orig_q=RN:39025830`.

[133] Benjamin Dudson, Kaden Loring, Hasan Muhammed, and John Omotani. Multi-species magnetized plasma fluid simulations with bout++/hermes. *Bulletin of the American Physical Society*, 2022. `https://meetings.aps.org/Meeting/DPP22/Session/GO05.4`.

[134] Jarrod Leddy and Ben Dudson. 3d plasma turbulence and neutral simulations using the hermes model in bout++: a study of linear devices and the tokamak edge and divertor region. In *APS Division of Plasma Physics Meeting Abstracts*, volume 2016, pages TO9–012, 2016. `https://ui.adsabs.harvard.edu/abs/2016APS..DPPTO9012L/abstract`.

[135] J.Leddy B.Dudson. Hermes-1, 2019. `https://github.com/boutproject/hermes`.

[136] Benjamin Dudson. Hermes-3, 2020. `https://hermes3.readthedocs.io/en/latest/introduction.html`.

[137] Andrew S Richardson. 2019 nrl plasma formulary. Technical report, US Naval Research Laboratory, 2019. `https://apps.dtic.mil/sti/pdfs/AD1116543.pdf`.

[138] William Morris, Joe Milnes, Tom Barrett, Clive Challis, Ian Chapman, Martin Cox, Geof Cunningham, Fahim Dhalla, Geoff Fishpool, Philippe Jacquet, et al. Mast accomplishments and upgrade for fusion next-steps. *IEEE Transactions on Plasma science*, 42(3):402–414, 2014. doi:10.1109/TPS.2014.2299973.

[139] V Rozhansky, P Molchanov, I Veselova, S Voskoboynikov, A Kirk, G Fishpool, P Boerner, D Reiter, and D Coster. Modeling of the edge plasma of mast upgrade with a super-x divertor including drifts and an edge transport barrier. *Plasma physics and controlled fusion*, 55(3):035005, 2013. doi:10.1088/0741-3335/55/3/035005.

[140] E Havlíčková, W Fundamenski, M Wischmeier, G Fishpool, and AW Morris. Investigation of conventional and super-x divertor configurations of mast upgrade using scrape-off layer plasma simulation. *Plasma Physics and Controlled Fusion*, 56(7):075008, 2014. doi:10.1088/0741-3335/56/7/075008.

[141] SA Self and HN Ewald. Static theory of a discharge column at intermediate pressures. *The Physics of Fluids*, 9(12):2486–2492, 1966. doi:10.1063/1.1761642.

[142] AA Pshenov, AS Kukushkin, and SI Krasheninnikov. Energy balance in plasma detachment. *Nuclear Materials and Energy*, 12:948–952, 2017. doi:10.1016/j.nme.2017.03.019.

[143] Kevin Verhaegh, Bruce Lipschultz, James Harrison, Basil Duval, Chris Bowman, Alexandre Fil, Daljeet Singh Gahle, David Moulton, Omkar Myatra, Artur Perek, et al. A study of the influence of plasma–molecule interactions on particle balance during detachment. *Nuclear Materials and Energy*, 26:100922, 2021. doi:10.1016/j.nme.2021.100922.

[144] GL Derks, JPKW Frankemölle, JTW Koenders, M van Berkel, H Reimerdes, M Wensing, and E Westerhof. Benchmark of a self-consistent dynamic 1d divertor model div1d using the 2d solps-iter code. *Plasma Physics and Controlled Fusion*, 64(12):125013, 2022. doi:10.1088/1361-6587/ac9dbd.

[145] J Uljanovs, M Groth, Aaro E Jaervinen, D Moulton, M Brix, G Corrigan, P Drewelow, C Guillemaut, D Harting, J Simpson, et al. The isotope effect on divertor conditions and neutral pumping in horizontal divertor configurations in jet-ilw ohmic plasmas. *Nuclear Materials and Energy*, 12:791–797, 2017. doi:10.1016/j.nme.2017.03.028.

[146] V Solokha, M Groth, S Brezinsek, M Brix, G Corrigan, C Guillemaut, D Harting, S Jachmich, U Kruezi, S Marsen, et al. The role of drifts on the isotope effect on divertor plasma detachment in jet ohmic discharges. *Nuclear Materials and Energy*, 25:100836, 2020. doi:10.1016/j.nme.2020.100836.

[147] CF Maggi, RD Monk, LD Horton, K Borrass, G Corrigan, LC Ingesson, RWT König, G Saibene, RJ Smith, MF Stamp, et al. The isotope effect on the l mode

density limit in jet hydrogen, deuterium and tritium divertor plasmas. *Nuclear Fusion*, 39(8):979, 1999. doi:10.1088/0029-5515/39/8/303.

[148] AJ Thornton. Mast-u experimental programme: From first plasma to first campaign, 2019. `https://agenda.enea.it/event/172/attachments/80/234/AJThornton_ISTW_final.pdf`.

[149] J. R. Harrison1 et al. Overview of first results from mast upgrade, 2021. `https://conferences.iaea.org/event/214/contributions/18686/attachments/9650/14332/Harrison_IAEA_2021_Poster_final.pdf`.

[150] D Post, J Abdallah, REH Clark, and N Putvinskaya. Calculations of energy losses due to atomic processes in tokamaks with applications to the iter divertor. 1995. doi:10.1063/1.871257.

[151] Daoyuan Liu, Chaofeng Sang, Liang Wang, and Dezhen Wang. The impact of neon-seeding location on the divertor plasma in east. *Fusion Engineering and Design*, 136:324–329, 2018. doi:10.1016/j.fusengdes.2018.02.018.

[152] R Clark, J Abdallah, and D Post. Radiation rates for low z impurities in edge plasmas. *Journal of nuclear materials*, 220:1028–1032, 1995. doi:10.1016/0022-3115(94)00467-6.

[153] Omkar Myatra. *Numerical modelling of detached plasmas in the MAST Upgrade Super-X divertor.* PhD thesis, University of York, 2021. `https://etheses.whiterose.ac.uk/29934/`.